NTNU – Trondheim
Norwegian University of
Science and Technology

Characterization of Insulation Materials for HVDC Subsea Connectors

Evaluation of Measurement Methods for
Surface Conductivity

Brynjar Aalberg Jacobsen

Master of Energy and Environmental Engineering
Submission date: June 2015
Supervisor: Frank Mauseth, ELKRAFT
Co-supervisor: Sverre Hvidsten, SINTEF Energy Research

Norwegian University of Science and Technology
Department of Electric Power Engineering

Problem description

The demands towards future oil and gas production include increased recovery and longer step-outs. Subsea processing is considered to be one of the main solutions for achieving these goals. To enable the next generation of subsea boosting and processing facilities, high power electrical connectors are strongly needed, and considered to be one of the most critical components. Furthermore, for the longest step-outs, the most efficient transmission scheme would be high voltage direct current (HVDC) or low frequency alternating current (LFAC).

The work will be part of a four-year research project on subsea connectors run by SINTEF Energy Research and NTNU in cooperation with several international connector manufacturers. The work will mainly be experimental, and the main purposes are to obtain essential knowledge and criteria for the insulation systems in subsea connectors. Material characterization, numerical simulations and development of test methods will provide the foundation for reaching these goals, as well as finding the most suited design and material combinations.

The focus of this work will be on characterization methods for the surface conductivity of insulation materials. Since subsea connectors consist of both solid insulation and insulation oil, determining the insulation oils effect on the surface conductivity is also of interest.

Preface

This thesis is the final work of the MSc in Energy and Environmental Engineering carried out at the Department of Electric Power Engineering at the Norwegian University of Science and Technology (NTNU) during the spring of 2015. The thesis is a part of a four-year research project on high voltage subsea connectors at SINTEF Energy Research and NTNU, in cooperation with international connector manufacturers. The thesis is a continuation of a specialization project previous semester.

I would like to thank my supervisor Professor Frank Mauseth for his guidance during this work, and SINTEF Energy Research for allowing me to use their laboratory equipment. This work has mainly been experimental, and if not for the insights from Torbjørn Ve at SINTEF Energy Research, I would not have been able to finish my measurements in time.

Lastly, I would like to thank my family, who have supported and encouraged me throughout my studies, and my friends and colleagues at NTNU for making the last five years so memorable.

Trondheim, 10th of June, 2015

Brynjar Aalberg Jacobsen

Abstract

The focus of this work has been on characterization methods for the surface conductivity of insulation materials in HVDC subsea connectors. Having a proper characterization is important when selecting the most suited design and material combinations. Two methods has been investigated; the first is a standard method (ASTM D257), using a test objects' geometrical properties, while the second method measures the polarization- and depolarization current (PDC) when it is subjected to a DC step voltage. Due to its widespread use and desirable material properties, the insulation material polyetheretherketone (PEEK) has been used throughout this work. From the PDC method, the surface conductivity is in the range of $4.4 \cdot 10^{-15}$ to $5.7 \cdot 10^{-14}$ S/m for 60 to 80 °C and 500 to1500 V. Fitting the measurements to an empirical equation resulted in the following expression for the surface conductivity in PEEK:

$$\sigma_s = 9.1 \cdot 10^{-18} e^{0.1079 \cdot T + 0.1628 \cdot E} \; [S/m]$$

Estimations at room temperature and low electric fields resulted in surface conductivities of approximately 10^{-14} and 10^{-16} S/m for the standard- and PDC method, respectively. The total deviation between the methods is more than two decades, and combined with the varying degree of uncertainty corresponding to the geometric properties and measured values, it is difficult to determine which method is better. The greatest sensitivity is however achieved with the PDC method, and by improving upon the uncertainties pointed out in this work, this method it is believed to be superior.

From curve fitting of the polarization currents, a two-termed exponential function was found to be a better fit than a single-termed, supporting ionic hopping as the dominating conduction mechanism in PEEK. The measurement time is however too short to determine any deviations between the single- or two-termed function and the resistive current. Thus, assessing whether or not the empirical equation is valid for the surface conductivity in PEEK has not been possible.

When exposed to insulation oil (MIDEL 7131), the surface conductivity of PEEK decreased significantly. The exposure to MIDEL also caused the evaporated electrodes to vanish at 80 °C, which is 10 °C lower than for unexposed PEEK. Depending on the process causing this phenomenon, accelerated ageing of the insulation material could be a possible consequence. Thus, further investigation of this matter and other findings in this work is important for characterizing PEEK for use in HVDC subsea connectors.

Sammendrag

Hovedformålet med denne oppgaven har vært å evaluere metoder som brukes til å bestemme overflateledningsevnen til et isolasjonsmateriale i HVDC subsea konnektorer. For å kunne velge de beste designene og materialkombinasjonene er det viktig vite hvordan isolasjonsmaterialet påvirkes av de gitte driftstilstandene. I denne oppgaven har to metoder for å bestemme overflateledningsevnen blitt undersøkt. Den første av disse er en veletablert standardmetode (ASTM D257) som benytter seg av resistansmålinger og geometrien til et testobjekt. Den andre metoden benytter sprangresponsen og kapasitansen til isolasjons-materialet for å estimere en overflateledningsevne. Isolasjonsmaterialet som er blitt brukt til forsøkene er polyetheretherketone (PEEK), og ble valgt på bakgrunn av ønskelige materialegenskaper og utstrakte bruk i allerede eksisterende konnektorer.

Fra sprangresponsmålinger ble overflateledningsevnen til PEEK estimert til å være mellom $4.4 \cdot 10^{-15}$ og $5.7 \cdot 10^{-14}$ S/m for temperaturer og spenninger mellom henholdsvis 60 og 80 °C, og 500 og 1500 V. Disse verdiene ble deretter approksimert til en empirisk formel, og et generelt utrykk for overflateledningsevnen i PEEK ble funnet:

$$\sigma_s = \sigma_0 e^{0.1079 \cdot T + 0.1628 \cdot E} \; [S/m]$$

Fra dette uttrykket ble overflateledningsevnen ved romtemperatur (20 °C) funnet til å være omkring 10^{-16} S/m. Den tilsvarende verdien fra standardmetoden ble bestemt til 10^{-14} S/m. Begge metodene har store usikkerheter knyttet til de både de geometriske og målte verdiene, og kombinert med det avviket på to dekader er det vanskelig å si sikkert hvilken av metodene som de beste resultatene. Måleutstyret brukt til sprangresponsmetoden muliggjør imidlertid en større grad av nøyaktighet i målingene enn standardmetoden, og ved å utbedre usikkerhetene påpekt i denne oppgaven er det stor sannsynlighet for at denne metoden vil gi de beste estimatene av overflateledningsevnen.

Det ble videre forsøkt med kurvetilpassing til sprangresponsen med to funksjoner (med henholdsvis ett og to eksponentielle ledd). Funksjonen med ett eksponentielt ledd kan sammenlignes med den empiriske formelen brukt til å estimere det generelle uttrykket over. På grunn av den korte måletiden er eventuelle avvik mellom denne og den faktiske resistive strømmen ukjent, og det er umulig å si noe om gyldigheten til den empiriske formel for PEEK. Den tidsavhengige delen av sprangstrømmen ble videre funnet til å følge funksjonen med to eksponentielle ledd bedre enn den med ett ledd, noe som betyr at mekanismene bak ledningsevnen sannsynligvis følger en tilsvarende funksjon.

For å bestemme hvordan overflateledningsevnen påvirkes av operasjonstilstandene til en konnektor ble PEEK prøvene utsatt for isolasjonsolje over lengre tid. Resultatet fra påfølgende sprangresponsmåling viste en mye lavere ledningsevne enn for tidligere målinger. I tillegg forsvant de pådampede elektrodene ved 80 °C. Dette skjedde også for testobjekter som ikke var utsatt for isolasjonsolje, men da ved 90 °C. I verstefall kan prosessen som fører til at elektrodene forsvinner også føre til hurtigere aldring av isolasjonsmaterialet. Videre undersøkelser av dette fenomenet er derfor viktig for videre karakterisering av PEEK.

Table of Contents

1 Introduction

1.1 Background

An increasing share of todays' energy consumption is related to electricity. At the same time as the rapid escalation in installed capacity of renewables is making it one of the most important sources for generating electricity [1], the world's energy supply is increasingly dependent on fossil fuels [2]. Fossil fuels play a much larger role in the generation of electricity than many believe; while renewables account for approximately 7,000 TWh of electricity, the mixture of electricity and heat from fossil fuels corresponds to 23,000 TWh [3].

The recovery of fossil fuels is moving away from today's topside solutions, and towards the use of subsea processing facilities with large quantities of electrical equipment on the seabed to increase the recovery rate (known as *boosting*). The future subsea processing facilities then require large amount of power, and connecting the equipment to the transmission system through connectors ensures easy and cost effective installation and retrieval of single components. Subsea connectors consist of a plug and a receptacle, where the moving current carrying components are covered in a solid insulation material [4]. An outer diaphragm containing insulation oil further protects the current carrying components and the solid insulation material from the external environment.

A consequence of the increasingly longer distances to offshore installations, the transmission lengths are exceeding those where standard high voltage alternating current (HVAC) systems are efficient. Depending on the transmission length, low frequency alternating current (LFAC) or high voltage direct current (HVDC) systems will be better alternatives [5, 6].

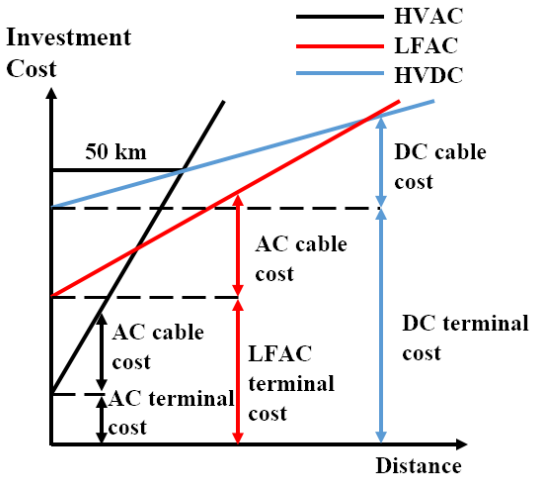

Figure 1.1. Break even distances for HVAC (non compensated),
Low frequency AC and HVDC transmission sytems for offshore wind farms [5].

Today, connectors are only available for medium voltage alternating current (MVAC), which means that development of HVDC equivalent connectors is necessary for the installations located at the longest step-outs. DC operation introduces different electrical stresses on the components and transmission systems compared to AC [7, 8], and two major challenges for the insulation material is temperature gradients and thermal ageing. High temperature gradients can cause field inversion, where the electric field stress is higher at the outer sheath than at the conductor. Thermal ageing can cause an increase in the rate of diffusion of surrounding penetrants, affecting the materials dielectric properties. A desirable quality with insulation materials is a low conductivity, but exposure to high temperatures and large amounts of penetrants might cause it to increase to a level causing equipment failure. The latter is especially relevant considering the constituents and external environment of a subsea connector. It then follows that properly characterizing the insulation material is important to ensure that an appropriate material combination is selected for any given operation condition and equipment type.

1.2 Objectives

To determine an insulation materials viability for HVDC subsea connectors, one of the material properties that needs characterization is the surface conductivity. There are several methods for determining the surface conductivity of an insulation material, and the focus of this study will be to evaluate two such methods. To assess its reliability, the first of these methods is a standard (ASTM D257). The second method should have a different methodology, but still be comparable to the standard method.

Polyetheretherketone (PEEK) will be the insulation material used throughout this work. PEEK is commonly used in MVAC connectors and other electrical components due do its desirable material properties. An added benefit of using PEEK is that the results could give indications to whether it is a viable insulation material for HVDC connectors or not.

Since subsea connectors consist of both solid insulation material and insulation oil, another step in the characterization of PEEK (or other insulating materials) is to determine the effect insulation oil has on surface conductivity.

2 Theory

In order to determine an alternative to the standard method for estimating the surface conductivity of PEEK, it is necessary to have a thorough understanding of (surface) conductivity and the corresponding conduction mechanisms, as well as the material properties of PEEK. In addition, it must be kept in mind that even if AC and DC voltages generally stresses the insulation material in different ways, a change in the applied DC voltage will initially cause the same stresses as AC [9].

2.1 Polyetheretherketone

Polyetheretherketone (PEEK) is a high performance thermoplastic, which can be annealed or thermally treated to have a varying degree of crystallinity [10]. The crystallinity of PEEK can be in the range of zero (amorphous) to 50 %, depending on the thermal history [11]. An increasing crystallinity generally reduces the conductivity. In addition, interfaces towards other regions of varying crystallinity can act as a source of charge trapping [12], which is important when considering the conduction mechanisms of a medium. Understanding these mechanisms does however require a more detailed approach, taken in Section 2.2.

PEEK has glass- and melting temperatures of 145 and 340 °C [12-16], making it well suited for use in high temperature environments. Additionally, PEEK is considered to be a thermally stable polymer, meaning its morphology is unaffected by thermal loading. Furthermore, the only changes in amorphous PEEK due to annealing is in the polymers' physical morphology, making its dielectric properties independent from i.e. chemical degradation or incomplete curing [10].

Common for the group of thermoplastics which PEEK belongs to are characteristics such as high chemical-, hydrolysis- and temperature resistance, as well as the material itself being strong and hard [11]. This also contributes to PEEK being very resistant against wear and fatigue. PEEK also has a fairly high molecular weight, and its density is typically around 1300 kg/m^3 [13]. In comparison, XLPE typically have a density around 920 kg/m^3.

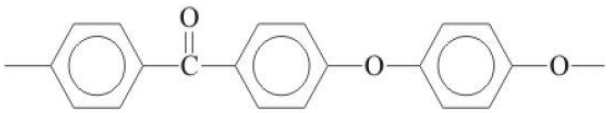

Figure 2.1. Repeating unit of the chemical formula for polyetheretherketone [12].

2.2 Conductivity

Three of the most common methods to describe the conductivity in a dielectric medium is through analysis of the conduction mechanisms, by empirical relationships, or by considering the medium as a component in a parallel plate capacitor.

2.2.1 Conduction mechanism

The conduction mechanisms are generally considered at a microscopic level, and the conductivity is then described as the transportation of electrons or ions through a medium [17]. The dominating conduction mechanism in PEEK is ionic hopping [14, 16].

Appendix A gives a detailed explanation of ionic hopping, but in short; ionic hopping is trapping of particles in potential energy wells between other particles. The particles have a probability to escape to the next trap, and if successful, contribute to a flux of charges across the well. On a macroscopic level, this flux contributes to an overall current density that depends on the materials conductivity and applied electric field.

The total conductivity of the medium is expressible by a two-termed exponential equation [18]:

$$\sigma = \frac{N_0 q \omega_0}{2\pi E} \exp\left[-\frac{H}{kT}\right] x \left\{\exp\left[\frac{(1-\beta)qbE}{kT}\right] - \exp\left[-\frac{\beta qbE}{kT}\right]\right\} \tag{2.1}$$

where

N_0 is the total number of particles in the medium
q is the particles corresponding charge
ω_0 is their attempt-to-escape frequency
β is a symmetry factor for the potential energy well
k is the Boltzmann constant
E is the electric field
T is the temperature
b is a length across the potential energy well

For a symmetrical potential energy well ($\beta = 1/2$), this equation can be expressed in terms of the constants A and B [17]:

$$\sigma = \frac{A}{E} \exp\left[-\frac{H}{kT}\right] \sinh\left(\frac{BE}{T}\right) \tag{2.2}$$

2.2.2 Empirical approach

Eq. (2.1) includes a large amount of parameters that must be determined, making it rather complex to solve. Thus, taking a simplified approach is often desirable. Based on measurements on HVDC mass impregnated cables, an empirical equation for the conductivity is as follows [18]:

$$\sigma = \sigma_0 e^{\alpha T + \gamma E} \tag{2.3}$$

where σ_0 is the conductivity at zero electric field and temperature. α and γ are the temperature and electric field coefficients.

Compared to Eq. (2.1), Eq. (2.3) only contain a single exponential term, but both equations are exponentially dependent on temperature and electric field. Furthermore, a change in α corresponds to a change in N and H, while a change in γ corresponds to a change in b.

There is little or no literature on the validity of the empirical equation for PEEK. It has however been proved to be a good approximation for extruded polyethylene insulation [19]. Since PEEK is a polymeric insulation material, it is a reasonable to believe that the empirical formula is valid also for this material. In addition, since PEEK is a thermoplastic, typical values for α and γ could be [20]:

Table 2.1. Typical values of α and γ for an extruded propylene-based thermoplastic material.

***E* [kV/mm]**	**20**	**30**	**60**
α [1/°C]	0.104	0.114	0.115*
***T* [°C]**	**20**	**60**	**80**
γ [mm/kV]	0.128	0.06	0.034

* For ethylene-based thermoplastic materials.

2.2.3 Geometrical approach

A less complex method to determine the conductivity of a medium is to consider it as part of a parallel plate capacitor:

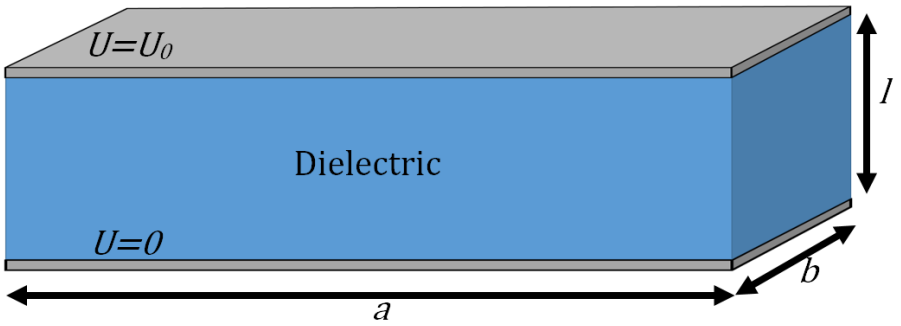

Figure 2.2. Parallel plate capacitor.

Not only does the capacitor consist of a medium with volume- and surface area, but it is also surrounded by another. This means that the total resistance of the capacitor is the contributions from the volume, surface and surrounding medium in parallel. The resistance of one such region of the capacitor is given by the resistivity, ρ, the length between the electrodes, l, and the effective cross section of the medium, S.

$$R = \frac{\rho l}{S} \tag{2.4}$$

Since the conductivity is inversely proportional to the resistivity, rearranging Eq. (2.4) leads to a total conductivity for the capacitor given as:

$$\sigma = \frac{1}{\rho} = \frac{l}{RS} \tag{2.5}$$

Solving this equation does however requires a known resistance.

2.3 Polarization

At an atomic level, all insulation materials consists of positive and negative charges [21]. These charges mostly balances each other out, creating an overall neutral charge. However, if the insulation material is subjected to an electric field, these charges may orient accordingly, contributing to macroscopic effects. The different effects are referred to as polarization mechanisms. On a macroscopic level, the four main mechanisms of polarization are electronic-, ionic-, orientation- and interfacial polarization [21, 22]:

- Electronic polarization is when an atom or molecule has its center of gravity displaced by an external electric field. More specifically, this effect is due to the electric field causing a displacement of the electrons orbiting the core, creating temporary dipoles. This effect is very rapid (up to optic frequencies), and vanishes with the electric field.
- Ionic polarization is effective in materials with ionic bonds. Without an applied electric field, these ionic bonds form a symmetrical lattice without dipoles. Applying an electric field causes elastic displacement of charges (positive and negative ions), creating temporary dipoles. This effect is fast, and vanishes with the electric field.
- Orientation polarization is due to the existence of permanent dipoles in the material. Permanent dipoles are in general randomly oriented in the medium, but aligns with applied electric fields. The action of thermal energy will however limit the permanent dipoles ability to align completely with the electric field.
- Interface polarization is due to impurities or imperfect arrangement of ions, atoms and molecules within the material. This means that there will be some interfaces in the dielectric. Interface polarization is therefore predominantly effective in materials composed of several dielectrics where the amount of effective interfaces is high. Under the influence of an electric field, moving charges can deposit at these interfaces, creating temporary dipoles.

Electronic and ionic polarization are fast, momentary mechanisms, and they vanish with the electric field. Orientation and interfacial polarization are slow mechanisms, commonly referred to as relaxation mechanisms, where the effect does not vanish with the electric field. Due to ions and electrons move more freely at higher temperatures, relaxation mechanisms are strongly temperature dependent. The polarization of a dielectric material can be expressed as [21]:

$$\Delta P(t) = \varepsilon_0 \chi_\infty E(t) + \varepsilon_0 \int_0^t f(t-\tau) E(\tau)\, d\tau \tag{2.6}$$

where χ_∞ is the momentary dielectric susceptibility, $f(t)$ is the dielectric step function, and $E(t)$ is the electric field.

When applying a step voltage to a dielectric material, the polarization mechanisms will contribute to the current density as follows [23]:

$$J(t) = \sigma E(t) + \frac{d}{dt}[\varepsilon_0 E(t) + \Delta P(t)] \tag{2.7}$$

By inserting Eq. (2.6) in Eq. (2.7), the current density may be expressed as [21, 22]:

$$J(t) = \sigma E(t) + \varepsilon_0 \frac{d}{dt}[(1 + \chi_\infty)\delta(t) + f(t)]E(t) \tag{2.8}$$

where $\delta(t)$ is the Dirac pulse, representing the momentary contribution in Eq. (2.6). The Dirac pulse cannot be recorded, and a simplified version of Eq. (2.8) is used to express the current through an object with a vacuum capacitance, C_0:

$$i(t) = C_0 \left[\frac{\sigma}{\varepsilon_0} U(t) + \varepsilon_r \frac{dU(t)}{dt} + \frac{d}{dt}\int_0^t f(t-\tau)U(\tau)\, d\tau\right] \tag{2.9}$$

Since this current is dependent on the applied voltage, an equally large change in either direction would cause similar effects. Thus, to determine the polarization- and depolarization current from Eq. (2.9), a step voltage with the following characteristics is applied [23, 24]:

$$U(t) = \begin{cases} 0 & t < 0 \\ U_0 & 0 \le t \le t_c \\ 0 & t > t_c \end{cases} \tag{2.10}$$

The resulting currents are then as follows:

$$\begin{aligned} i_p(t) &= C_0 U_0 \left[\frac{\sigma}{\varepsilon_0} + f(t)\right] \\ i_d(t) &= -C_0 U_0 [f(t) + f(t_c + t)] \end{aligned} \tag{2.11}$$

2.4 Polarization- and depolarization current measurements

A widely used method to determine the conductivity of an insulation material is to investigate the materials' dielectric response by measuring the polarization- and depolarization current (PDC) [25]. The principle methodology is to measure the currents in the insulation material when it is subjected to a step voltage and subsequent short-circuit (Figure 2.3). The resulting currents will then correspond to those in Eq. (2.11). In addition to the simple methodology, PDC measurements are non-destructive for the insulation material.

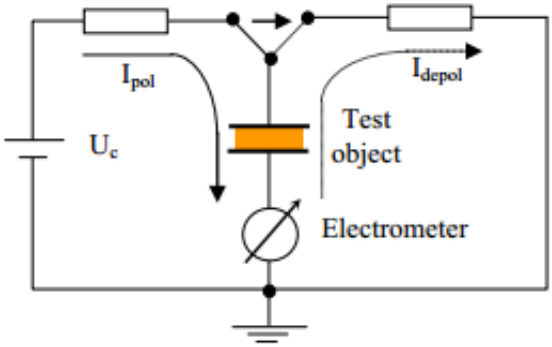

Figure 2.3. Principal polarization- and depolarization current measurement setup [26].

Given that the measurement periods are long enough for the polarization mechanisms to cease, plotting the measured PDC will yield a graph similar to that of Figure 2.4, where the large, momentary peak values in the PDC corresponds to the Dirac pulse in Eq. (2.8).

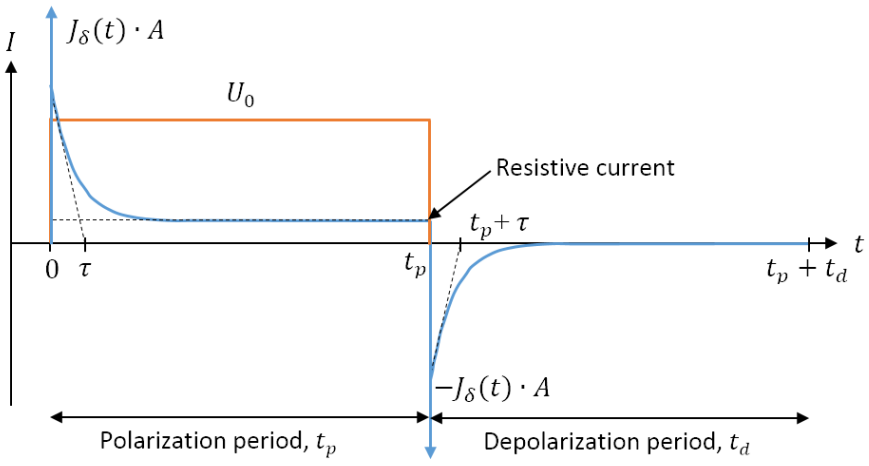

Figure 2.4. Polarization- and depolarization current waveforms.
During the period of polarization, t_p, a DC step voltage is applied to the dielectric material.

The duration of polarization, t_p, and depolarization, t_d, are usually equal [25], but not a necessity. It is important that there are no remnant charges or contributions from the polarization mechanisms between measurements to obtain reliable results.

2.5 Conductivity estimation

The contributions from the polarization mechanisms to the current in Eq. (2.9) will eventually cease as they reach their new state (i.e. orientation or location). The time dependent terms in Eq. (2.11) then becomes zero, and it follows that the polarization current is proportional to the conductivity and the depolarization current is zero. At this time, the polarization current is said to be purely resistive [23, 24]. The transition time from a capacitive to resistive distribution can be estimated as an exponential decay function, where the time constant may be described as [19]:

$$\tau = \frac{\varepsilon}{\sigma_a} \tag{2.12}$$

where σ_a is the apparent conductivity of the dominating charging mechanism.

The transition time in Eq. (2.12) is expressed in terms of the material constants, meaning that it would be the same for both the polarization- and depolarization current. Thus, the time-dependent terms of the PDCs' are opposite of one another, and by combining the currents in Eq. (2.11), the estimated conductivity of the material becomes [17, 19, 23, 24]:

$$\sigma = \frac{\varepsilon_0}{C_0 U_0}\left(i_p(t) - i_d(t)\right) \tag{2.13}$$

The vacuum capacitance, C_0, may also be expressed as the measured capacitance, C, near, or at, the rated power frequency, divided by the relative permittivity, ε_r.

Since the time dependent terms of the polarization- and depolarization current is opposite one another, Eq. (2.13) can be expressed in terms of the measured capacitance and resistive current, I_{DC}:

$$\sigma = \frac{\varepsilon_0 \varepsilon_r}{C U_0} I_{DC} \tag{2.14}$$

Eq. (2.14) can also be shown for a parallel plate capacitors with a capacitance of:

$$C = \frac{\varepsilon_0 \varepsilon_r S}{l} \tag{2.15}$$

By applying a DC voltage, U_0, to the capacitor, the resistive current is given by Ohms' law. Combining this with Eq. (2.4) and (2.15) gives the following relationship:

$$I_{DC} = \frac{U_0}{R} = \frac{U_0 S}{\rho l} = \frac{\sigma U_0 C}{\varepsilon_0 \varepsilon_r} \tag{2.16}$$

Solving Eq. (2.16) for σ gives the same expression for the conductivity as in Eq. (2.14).

2.6 Diffusion

The diffusion mechanism in PEEK follows the free-volume theory known as Fickian diffusion [15]. Free-volume theory states that the amount of sorption is dependent on the available free volume within the material, as well as the size of the penetrants' molecules. To qualify as Fickian, the diffusion of penetrant must follow Fick's laws, and can furthermore be completely characterized by determining the mutual diffusion coefficient, D, and its dependence on temperature, pressure, concentration and polymer molecular weight [27]. Fick's first law state that the penetrants' rate of transfer through an unit area, F, is proportional to the concentration gradient:

$$F = -D\frac{\delta C}{\delta x} \tag{2.17}$$

Fick's second law gives the rate of change to the concentration over time:

$$\frac{\delta C}{\delta t} = -\frac{\delta F}{\delta t} = \frac{\delta}{\delta t}\left(D\frac{\delta C}{\delta x}\right) \tag{2.18}$$

Fickian diffusion can be divided into case I and II (or type A and B) [15, 28]. Case I diffusion is typically observed with small penetrant molecules, while case II is more common with larger organic vapor molecules. If the diffusion coefficient is independent of time, concentration and plane thickness, as well as having a low solubility, the diffusion is said to be case I. Due to the independent relationship between the diffusion coefficient and the plane thickness, case I diffusion can be considered to be a one dimensional process. On the other hand, when the diffusion coefficient is dependent on both temperature and concentration, as well as for non-dilute penetrant-polymer mixtures, the process is defined as case II.

Given a large plane sheet where fickian case I is valid, the solution to Eq. (2.17) gives the following fractional weight gain [15, 28, 29]:

$$\frac{M_t}{M_\infty} = \frac{4}{\sqrt{\pi}}\left[\frac{Dt}{l^2}\right]^{\frac{1}{2}} \tag{2.19}$$

where M_t is the mass absorbed at time t, M_∞ is the equilibrium sorption at infinite time and l is the plane sheet thickness.

The mass absorbed at time t is found by the corresponding weight at that time, W_t, and the initial weight of the specimen, W_0:

$$M_t = W_t - W_0 \tag{2.20}$$

By acknowledging the linear relationships in Eq. (2.19), the diffusion coefficient can be determined by the slope obtained when plotting the fractional weight gain versus the square root of time [15, 29, 30].

$$D = \frac{\pi}{16} S^2 \tag{2.21}$$

where S is the slope of the fractional weight gain plotted against the square root of time. For case I diffusion, the slope will be a straight line.

In PEEK, the amount of sorption is affected by both the crystallinity and density of the material [29]. If the crystallinity of a material increases, the sorption amount typically decreases. However, interfaces to other materials, as well as the processing methods of the material could cause the sorption to deviate from this statement [31]. Denser materials typically have a lower amount of sorption. For example, if two different materials are the same size, but have different density, it is evident that the densest material has the least amount of free volume. This means that the individual free volumes for the densest material must then be either fewer, smaller, or a combination of the two. Large molecules that fit in the least dense material does therefore not necessarily fit in the densest one.

Compared to the sorption of water, there is a little or no literature on the sorption of oil in PEEK. If exposed to water, the time to reach equilibrium water content for a 2 mm thick specimen is approximately 400 hours at 35 °C, and less than 100 hours at 95 °C [15]. This indicates that higher temperatures cause higher diffusion rates, and it is reasonable to assume that this is valid for (insulation) oil as well. In addition, since the size of the molecules of an insulation oil is much larger than that of a water molecule, the corresponding sorption rates might be lower for oil than for water.

3 Design of PEEK specimens

The focus of this study is as mentioned in Chapter 1 to evaluate a standard- and alternative method of estimating the surface conductivity of an insulation material, more specifically PEEK. The ASTM standard include several different specimen designs, but common for them is to use resistance measurements and geometrical properties to estimate the surface conductivities. An alternative to this method is to apply the PDC measurement methodology from Section 2.4. This method is widely used for its simple methodology, as well as being non-damaging for the insulation material. For additional comparison between the standard- and PDC method, having two different specimen designs is beneficial.

Knowing the possible ranges for the resistive current is useful when determining what equipment to use in the measurement setup. Thus, using the material properties of the PEEK and the final specimen designs, some simple calculations of the expected currents can be performed.

3.1 ASTM specimens

Choosing between the possible designs suggested by the ASTM standard depends on several factors, i.e. material properties or available equipment. The materials' thickness, hardness and whether or not it can be molded, are also important to consider.

Since the evaluation of this standard is regarding surface conductivity measurements, thin PEEK specimens with a high surface-to-volume ration between electrodes is preferable. This also corresponds well to the 0.25 and 0.5 mm thick PEEK films available (Chapter 4). The ASTM standard suggests the circular design shown in Figure 3.1 for thin insulation films [32].

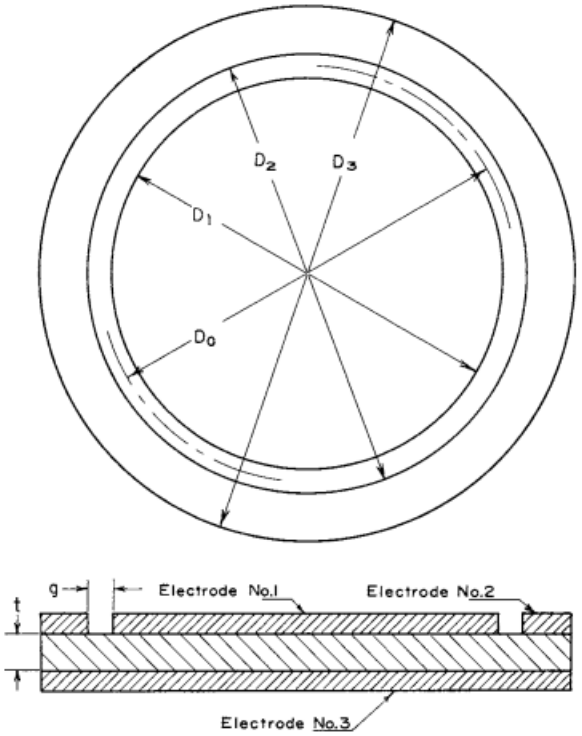

Figure 3.1. The ASTM standards' electrode layout for thin circular specimens.

This design has three evaporated metal electrodes (E1, E2 and E3), which can serve as the HV-, guard- and measurement electrode. It is possible to measure across both the surface- and volume of the specimens by varying the connections according to Table 3.1.

Table 3.1. Electrode connections for the ASTM specimens

	Surface	**Volume**
E1	HV	Measurement
E2	Measurement	Guard
E3	Guard	HV

The standard does not set any specific requirements to the electrode thicknesses, but rather suggests a typical thickness between 6 and 80 µm. The evaporated electrodes further contributes to a larger resistance than for the surface alone. This error is reduced as the insulation thickness increases, and a thickness equal to, or greater than, 0.25 mm is suggested [32]. Both 0.25 and 0.5 mm thick PEEK films are available, but selecting the 0.5 mm thick film should minimize this error.

Selecting the 0.5 mm thick film also affects how large the evaporated electrodes can be. Firstly, the length of the gap between electrode E1 and E2 should be equal to two times the insulations thickness, adding up to 1 mm. Secondly, in Figure 3.1 the specimen thickness is also the same as the creep length between electrode E2 and E3 (for volume measurements). Depending on the

surrounding medium and possible contaminations in the material, such a short creep length could cause issues, i.e. flashovers or conductive paths between E2 and E3. To have specimens that are usable for both surface- and volume conductivity estimations, the design should account for both measurement methods. By considering the critical field strength of the surrounding medium, the minimum creep length can be calculated from the desired test voltage. If the 35 kV voltage source from Section 4.4.2 is used for volume conductivity measurements, the critical field value of 2.2 kV/mm (Section 4.2) yields a minimum creep length of 15.9 mm. This does not account for possible contamination, and to make the design more practical, the creep length is therefore set to 20 mm (10 mm on each side of the specimen).

The bell jar on the vacuum evaporator in Section 4.1.3 has an inner diameter of 220 mm, and in order to evaporate more than one specimen at the time, the outer diameter of the specimens must be limited to 100 mm. Limiting the diameter is however a tradeoff, as the accuracy of the measurements increases with the size of the specimen [32]. Table 3.2 show the final geometry and electrode design of the specimens.

Table 3.2. Geometry and design of the evaporated electrodes of the ASTM specimens in Figure 3.1.

Measurement	**[mm]**
Specimen thickness	0.5
Specimen diameter	100
Gap length	1
E3 diameter, D_3	80
E2 inner diameter, D_2	60
E1 diameter, D_1	58
Mean gap diameter, D_0	59
Mean gap circumference	186

Since the focus of this study is the surface conductivity, E1, E2 and E3 serves as HV-, measurement and guard electrode from here on. The evaporated electrodes does not allow any direct connection to any equipment, meaning that a set of external electrodes are necessary. To avoid having an interface of air between the external electrodes and the PEEK, the width and diameters of the external electrodes should match the evaporated ones. To eliminate the risk of misalignment, the external electrodes should not cover the entire evaporated electrodes. For the distinction between the HV- and measurement electrode, the external electrode for the measurement electrode must be a hollow cylinder. Thus, the external measurement electrode in Figure 3.2 has an inner and outer diameter of 66 and 79 mm, while the ground- and HV electrode has diameters of 80 and 40 mm.

Figure 3.2. External ASTM electrodes.

3.1.1 Simulations

The simulation model in COMSOL utilizes rotational symmetry. This allows the model to be set up in two dimensions, with the radial distance from center and the height (thickness) as axes. For simple scaling, the applied DC voltage is set to 1 kV, while the thickness of the evaporated aluminum is set to 0.8 µm (according to the findings in Section 5.3). The figure below show the resulting electric field across the gap.

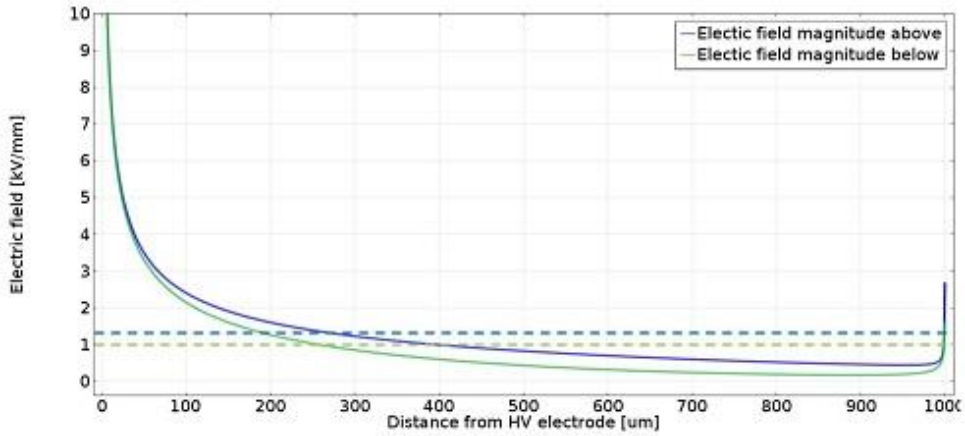

Figure 3.3. Electric field magnitudes for the ASTM model. The solid lines show the magnitudes as afunction of distance from the HV electrode, and the dashed lines their respective average values.Y-axis limited to 10 kV/mm.

In Figure 3.3, the electric field above and below the surface is less than the average value for approximately 70 and 75 % of the gap length. Due to the circular electrode design, the electric field is also unsymmetrical. The general shape of the electric field magnitude plot in Figure 3.3 is similar to that obtained in the specialization project leading up to this work [33], and will therefore not be analyzed in detail here.

Evaluating the electric field magnitudes from Figure 3.3 in COMSOL gives the following maximum-, minimum- and average values:

Table 3.3. Electric field magnitudes for the ASTM specimens.
Values found through line evaluation in COMSOL.

	E_{above} [kV/mm]	E_{below} [kV/mm]
Maximum	56.5	36.5
Minimum	0.5	0.2
Average	1.3	1.0

3.1.2 Current calculation

To find the expected resistive current for these specimens, the design in Table 3.2 and the material properties of the PEEK serves as a starting point [13]. These material properties are valid only under the same conditions as those specified in IEC 60093 *Methods of test for volume resistivity and surface resistivity of solid electrical insulating materials*. By using the test voltages from Section 4.3, the only unknown is the resistance of the model. Neglecting any contributions from volume- or short-circuit resistances, the surface resistances of the specimens are determined by solving Eq. (2.4) with a surface conductivity of 10^{-15} S/m. Since the reliability for the standard method of determining the surface conductivity is in question, covering a wider range of surface conductivities might give a better basis for comparison with actual measurements.

Table 3.4. Expected resistive currentsfor the ASTM specimens
at different surface conductivities and voltages

		Expected resistive currents [pA]		
σ_s [S/m]	R [GΩ]	U_0 = 0.5 kV	U_0 = 1 kV	U_0 = 1.5 kV
$\mathbf{10^{-14}}$	540	927.0	1 853.0	2 780.0
$\mathbf{10^{-15}}$	5 400	92.7	185.3	278.0
$\mathbf{10^{-16}}$	54 000	9.3	18.5	27.8

3.2 Alternative specimens

The starting point for designing the alternative specimens is to consider its main purpose - to compare the test results with the ASTM specimens to help evaluate the standard- and PDC method. The basic design principles for the Alternative specimens was determined in previous work, and utilizes a rectangular electrode setup as shown below [33]:

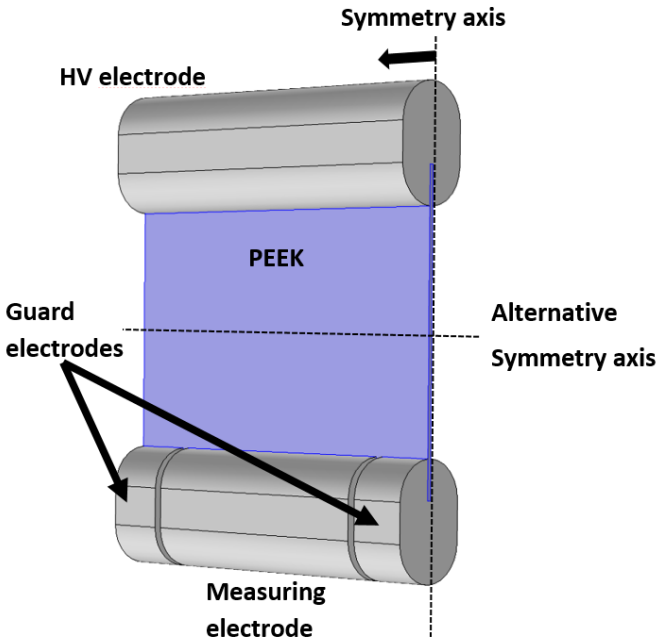

Figure 3.4. Basic design principle for the Alternative specimens and external electrodes

As with the ASTM specimens, these specimens also requires external electrodes to enable PDC measurements. Furthermore, guard electrodes ensure that any inhomogeneous electric fields along the edges of the PEEK does not contribute to inaccuracies in the measurements. Figure 3.5 show the principle design for the evaporated electrodes.

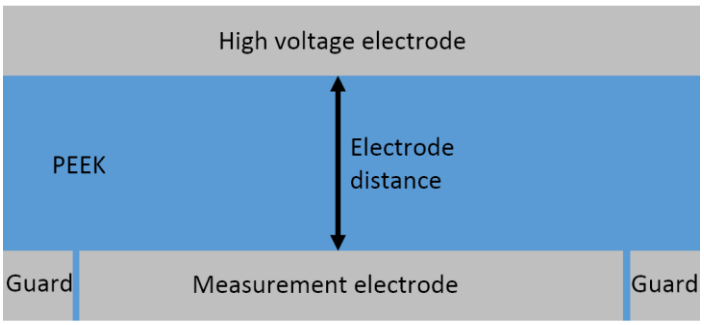

Figure 3.5. Evaporated electrodes design for the Alternative specimens.

To make comparisons as easy as possible, the design for the Alternative specimens inherits a few design parameters from the ASTM specimens; the thickness of the PEEK film is 0.5 mm, and the gap between the HV- and measuring electrode is 1 mm. Furthermore, to match the

circumference of the gap in Table 3.2, the width of the Alternative specimens' measurement electrode has to be 93 mm. The width of the guard electrodes is for simplicity set to 10 mm, and is separated from the measurement electrode by 1 mm. A smaller distance could possibly have beneficial effects on the field directionality close to the edge, would also make the electrodes more challenging to manufacture. Table 3.5 show the resulting design of the evaporated electrodes.

Table 3.5. Evaporated electrode design for the Alternative spcimens.

Measurement	**[mm]**
Measurement electrode width	93
Guard electrode width	10
Guard gap	1
Electrode length	20*
Specimen width (HV electrode width)	115
Electrode distance	1

* Determined from the design of the external electrodes.

The next step in optimizing the method is to improve the external electrodes. In Figure 3.4, the parts of the external electrodes that face each other are similar to that of a sphere gap. As long as the distance between the spheres are less or equal to 16 % of the spheres' diameter, the electric field is homogeneous (Section 4.2). Having a 1 mm electrode distance then requires an electrode diameter of at least 6.3 mm. To ensure that the method is applicable to specimens with a larger gap distance, it is desirable to have electrodes exceeding this diameter.

The directionality of the electric field is another factor that affects the design of the electrodes. The electric field initiates normal to the electrodes surfaces', which is not parallel to the PEEK in Figure 3.4. A nonlinear directionality close to the surface could cause inaccuracies in the measurements. Therefore, designing a section on the electrodes running normal to the PEEKs' surface before initiating the curvature could have a beneficial effect on the homogeneity of the electric field. To avoid deviating too far from the sphere-sphere analogy, this normal section should not be too large.

To ensure sufficient contact between the external electrodes and the specimen, designing an area on the electrodes exerting extra pressure onto the specimen might be beneficial. Including the previously mentioned limitations and design factors, Figure 3.6 show a principle design of the external electrodes.

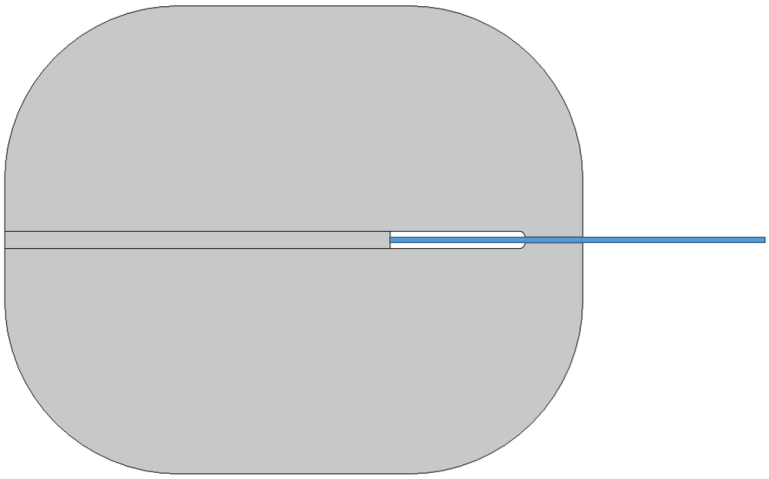

Figure 3.6. Principle design of the external electrodes for the Alternative specimens.
PEEK specimen shown in blue.

The small pockets of air in Figure 3.6 should not pose a risk since the surrounding boundaries are all at the same potential. When attaching the guard electrodes to the measurement electrode, there can be no metallic contact, and having an insulating layer between them is necessary. Since there should be zero potential at the guard electrodes, this layer can be very thin, but for practical reasons it is chosen to be a 1 mm thick Teflon layer. The material choice is due to the availability of Teflon screws (to attach the guard electrodes to the remaining structure) and a desire to keep the amount of different materials used at a minimum.

The design of these electrodes are complex, and when determining the final geometries, they must be so that manufacturing the electrodes is possible. By help from computer simulations (Section 3.2.1), Table 3.6 and Figure 3.7 show the final geometries and manufactured design.

Table 3.6. Final design of the external electrodes for the Alternative specimens.

Measurement	**[mm]**
Radius of curvature	20
Section normal to the insulation	5
Width	155
Length	75
Total height	50

Figure 3.7. Final design for the external electrodes for the Alternative specimens. The wires are for grounding the guard electrodes.

3.2.1 Simulations

The simulations for the Alternative specimens are both a tool for developing and evaluating the design. With the principle design in Figure 3.6, a parametric sweep in COMSOL helps determine the final geometries of the electrodes. The parameters in the sweep, the curvature (radius) of the electrodes and height of the normal section, ranged from 20 to 30 mm, and 5 to 10 mm, respectively. As with the ASTM simulations, a 1 kV DC voltage is applied to the HV electrode. The parametric sweep revealed that all parameter combinations results in the same electric field near the PEEKs' surface (Table B-1). Thus, selecting the best combination relies on whichever is the most practical one.

Knowing the final design of the specimens and electrodes, the electric field magnitudes across the gap is as follows:

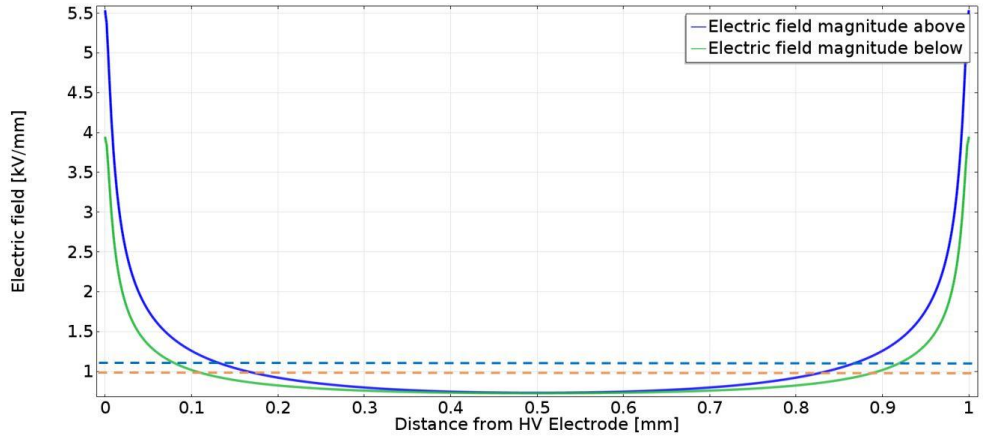

Figure 3.8. Electric field magnitudes for the Alternative model. The solid lines show the magnitudes as a function of distance from the HV electrode, and the dashed lines their respective average values.

The electric field above and below the surface in Figure 3.8 are less than the average for approximately 74 and 80 % of the gap length. The electric field is also symmetrical across the gap due to the rectangular design. Evaluating the electric field magnitudes across the gap yields the following maximum-, minimum- and average values:

Table 3.7. Electric field magnitudes for the Alternative specimens found by line evaluation in COMSOL.

	E_{above} [kV/mm]	E_{below} [kV/mm]
Maximum	5.5	3.9
Minimum	0.7	0.7
Average	1.1	1.0

3.2.2 Current calculations

Using the same method as for the ASTM specimens in Section 3.1.2, the resistive currents for the Alternative specimens are as follows:

Table 3.8. Expected resitive currents for the Alternative specimens at different surface conductivities and voltages.

		Expected resistive currents [pA]		
σ_s [S/m]	R [GΩ]	U_0 = 0.5 kV	U_0 = 1 kV	U_0 = 1.5 kV
10^{-14}	540	930.0	1 860.0	2 790.0
10^{-15}	5 400	93.0	186.0	279.0
10^{-16}	54 000	9.3	18.6	27.9

4 Experimental

One of the assessment points for the PDC method is the comparison of the resistive current and corresponding surface conductivity in two different PEEK specimens. Due to the exponential proportionality in Eq. (2.3), comparing the methods require the measurements to be performed at the same temperatures and applied voltages. By fitting exponential trendlines to the estimated surface conductivities, the exponential relationships in the empirical equation can be determined. To fit the trendlines to the measurements, at least three temperatures and electric fields are necessary, meaning that for each test voltage, a minimum of three temperatures is required, or vice versa. The maximum test voltage is dependent on the critical field strength of the medium around the test object, which is further dependent on test temperatures and electrode design. Beginning at the lower end, the initial test temperatures is set to 30, 60 and 90°C. This allows the temperatures to be increased if a larger contribution to the conductivity in Eq. (2.3) is necessary.

4.1 Specimen preparation

The PEEK films available from SINTEF Energy Research are 0.25 and 0.5 mm thick films of VESTAKEEP 3300G, manufactured by Evonik Industries AG. These films are initially rolled up, causing any pieces cut from the roll to have some curvature to it. The preparation of the PEEK specimens fall into three main steps: the general shapes, accessories required for evaporating the electrodes, and finally the evaporation process itself. As a precaution, degassing the PEEK films at 90 °C for 72 hours should remove any water- or gas content. The vacuum evaporator used to evaporate the electrodes onto the specimens have a bell jar with an inner diameter of approximately 220 mm (Section 4.1.3). Limiting the outer diameter of the ASTM specimens to 100 mm make it possible to evaporate three specimens at the time. The final design of the Alternative specimens also makes it possible to evaporate three specimens at the time.

4.1.1 Specimen shapes

Using a circular stamp with an inner diameter of 100 mm and a hydraulic press, the ASTM specimens are easily cut from the PEEK film. Placing a plastic film at each side of the PEEK protects the surface from contaminants and scratches from the process. Due to the lack of rectangular stamps, the Alternative specimens had to be prepared by drawing the shapes onto the PEEK film before cutting them by hand. To match the dimensions in Table 3.5, the metal plates cut from the matrix in Section 4.1.2 can serve as a guide when drawing. Manually cutting the PEEK results in some roughness along the edges, whereas two of the edges will be located inside the external electrodes, while the two remaining edges will be in contact with the guard electrodes (Figure 3.5). This means that any inhomogeneity along the edges should not affect the measurements.

4.1.2 Accessories

To support the specimens during the evaporation process, one matrix for each specimen type is required. The general design principle for these matrices is that they should have holes in the frame that matches the specimens. Common for the matrices is that they consist of two steel plates, measuring 220 mm in diameter. The lower plate provides support for the samples, while the upper plate secures the specimens, preventing them from moving out of position.

The lower and upper steel plate of the ASTM matrix both have three holes, measuring 98 and 100 mm, respectively. This makes it possible to fit different sets of electrode rings (Figure C-1) in the matrix to obtain the creep distance and electrode setup specified in Table 3.2. These electrode rings are 1 mm thick, and to be able to secure the specimens in place, the upper plate is 2 mm thick. The lower plate is only for support, and a thickness of 1 mm is sufficient. Six 160 mm long steel legs elevate the specimens to the height required for the evaporation procedure, as well as attaching the two steel plates.

The matrix used for the rectangular specimens also consist of two steel plates. Since the electrode layout is identical on both sides of the samples, the lower steel plate incorporates the necessary metal guides for the distinction between the guard- and measurement electrodes. This further means that 1 mm thick steel plates are sufficient for this design. To support the specimens, the holes in the lower steel plate are 1 mm shorter at the edges that will be locaten inside the external electrodes. This will result in a 1 mm unevaporated section on the specimens, but due to the location, this should not have any impact on the electric field distribution. Four 160 mm steel legs attach the two steel plates.

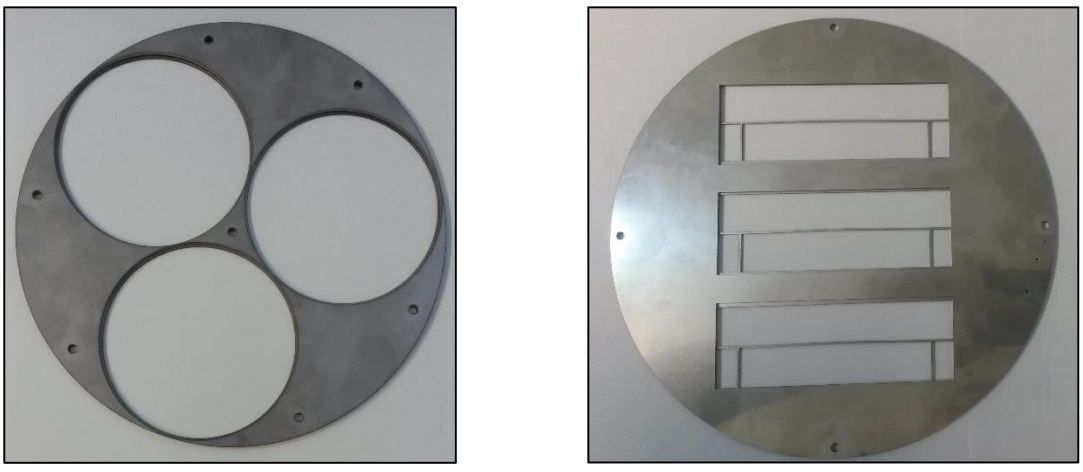

(a) (b)

Figure 4.1. Matrices used for the evaporation procedure. The 160 mm long legs are not attached. (a) the matrix used to fit the ASTM electrode rings. (b) Matrix used to fit the alternative specimens.

4.1.3 Evaporation

The next step in the preparation of the specimens is applying the thin evaporated electrodes. This process utilizes a vacuum evaporator to vaporize a piece of aluminum under low pressure, making it adhere to the insulation material (Appendix C.2). Figure 4.2 show how the specimens after the evaporation procedure.

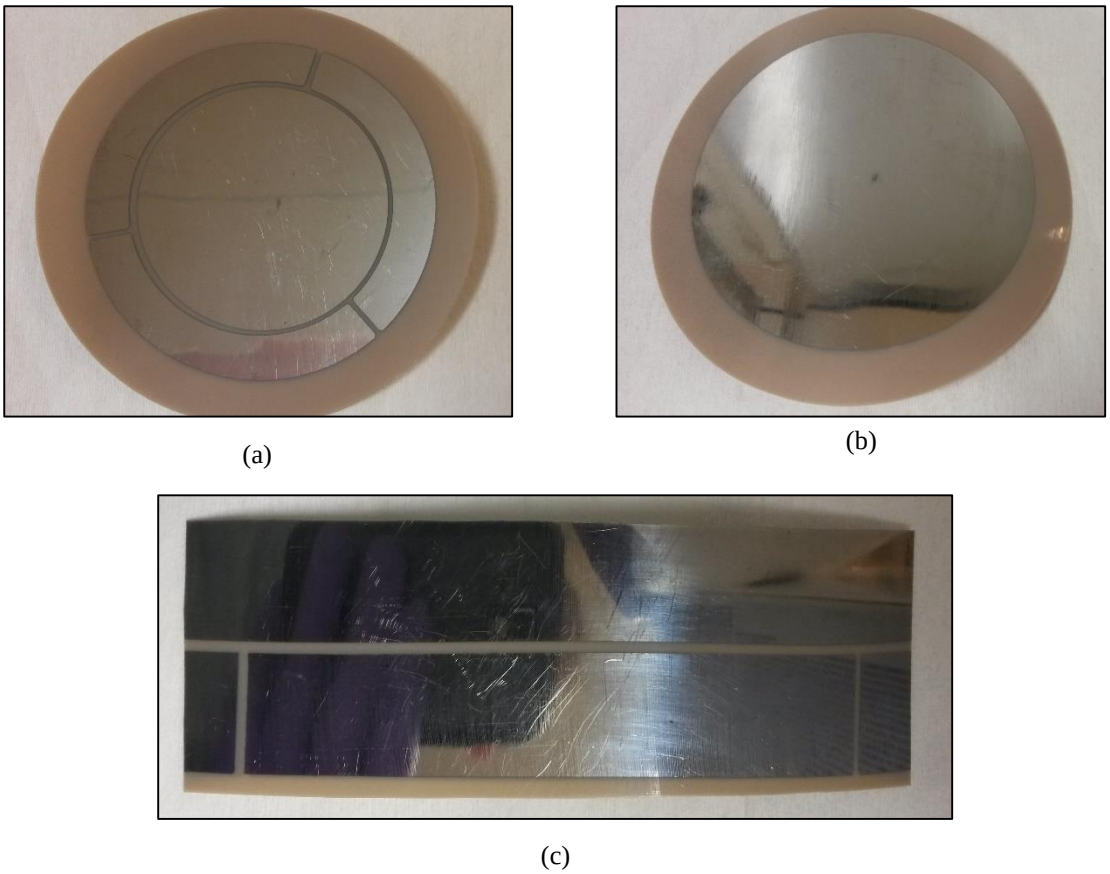

(a) (b)

(c)

Figure 4.2. Evaporated specimens. (a) ASTM: HV side, (b) ASTM: ground side, and c) Alternative specimen.

4.2 Critical field strength

The test voltages depend on the critical field strength of the air surrounding the specimens, which further depends on the frequency, electrode shapes, pressure, temperature, and voltage polarity [34-36].

The external electrodes for the alternative specimens are similar to that of a sphere gap. For a gap-to-diameter ratio of up to 40:250 mm (16%), the electric field is identical to that of a homogeneous field between Rogowski electrodes [34]. Then, for pressures between 1 and 5 atm, the following equation may be used to determine the influence of temperature and pressure on the electric field strength:

$$E_{critical} = \frac{p}{p_0}\frac{T_0}{T}\,E_0 \tag{4.1}$$

where p_0 is 1 atm, T_0 is 293 K, and E_0 is the corresponding critical field strength at a given gap distance.

For homogeneous electric fields, the critical field strength is typically around 2.8 kV/mm, and solving Eq. (4.1) at 1 atm and 363 K (90 °C) then results in a new critical electric field strength of 2.2 kV/mm. The electrodes of the alternative method have a gap-to-diameter ratio of 2%, indicating that the field is homogeneous. However, keeping in mind that this value is under ideal conditions and without a solid insulation material between the electrodes, a lower electric field strength might be more realistic. Alternatively, to have the flexibility to increase the temperatures at a later stage, rearranging Eq. (4.1) for a critical field strength of 2.0 kV/mm, yield a maximum test temperature of 137.2 °C.

4.3 Test voltages

As previously stated in this Chapter, at least three test voltages is required to be able to approximate the exponential proportionalities to the current or conductivity. In addition, acknowledging that the critical field strength from Section 4.2 in reality might be lower than 2.2 kV/mm, having a buffer in the test voltage is necessary. Thus, for 1 mm long gaps, an upper limit of 1.5 kV is reasonable. This also allows increasing the temperature beyond 90 °C if necessary. Three test voltages of 0.5, 1.0 and 1.5 kV then maximizes the step length between each measurement.

4.4 Measurement setups

To be able to measure the PDC, a DC voltage source and a measurement device are natural components of the measurement setup. In addition, since the conductivity is exponentially dependent on temperature, it is important that that the PEEK specimens are kept in a stable temperature-controlled environment.

Due to the low currents in Table 3.4 and Table 3.8, a picoammeter is best suited to measure the current. The picoammeter selected is the Keithley model 6485. The different measurement ranges of the picoammeter (mA, μA or nA) is achieved as the picoammeter switches between internal resistances. This makes it vulnerable to sudden over currents, which means that the applied voltage must be limited so that no flashovers or short-circuits occur across the test object or surrounding air. The test voltages in Section 4.3 includes a margin to prevent such flashovers. For additional protection of the picoammeter, it is suggested to connect a current limiting resistor in series [37].

4.4.1 Simple setup

Having found the critical field strength to be 2.2 kV/mm, a 5 kV Keithley model 245 DC source is sufficient for the measurement setup. A heating cabinet ensures control over the temperature of the specimen, and a 10 MΩ resistor (EGB SGP148) limits the short-circuit current at 1.5 kV to 0.15 mA.

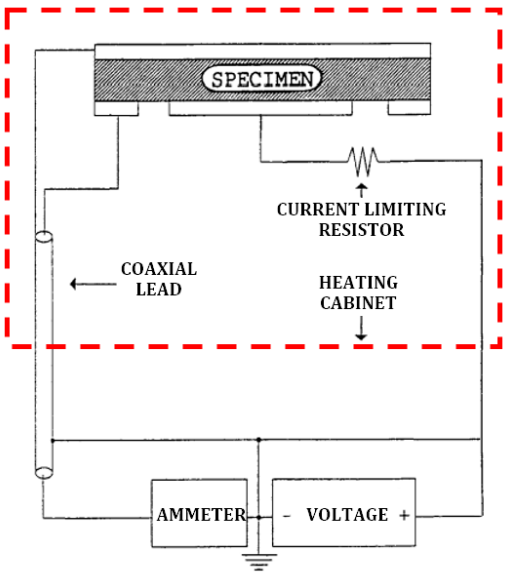

Figure 4.3. A simple measurement setup for surface conductivity with a voltage source, ammeter and a current limiting resistor.

By placing a Faraday cage inside the heating cabinet, the electromagnetic disturbance around the specimen and electrodes are reduced. To safeguard surrounding personnel, all hazardous

surfaces or objects, are either directly grounded, or enclosed in a grounded box. A mechanism on the door also brakes the power supply to the DC source if opened. The temperature limit of the current limiting resistor is 225 °C [38], and placing it inside the heating cabinet, manufacturing a grounded metal box for it is avoided.

The simple circuit in Figure 4.3 requires manually grounding the HV side to measure the depolarization current. Such a manual operation would require opening the door to the cabinet, causing warm air to flow out of the heating cabinet. This would in turn invalidate Eq. (2.14) by making the conductivity a function of time. Measuring the depolarization current is therefore not a viable option with this setup. Estimating the surface conductivity does however only require the resistive current, and measuring the polarization period is sufficient. This means that a LabVIEW program for logging and controlling the picoammeter is the only remote operation necessary for this setup.

4.4.2 Advanced setup

As stated in Section 2.4, if the relaxation mechanisms have not ceased completely before starting a measurement, the results could be inaccurate or invalid. This means that knowing the duration of the depolarization period of the dielectric is useful. To be able to measure the depolarization current, a more intricate setup with switching relays is required. Figure 4.4 show one such setup developed at SINTEF Energy Research.

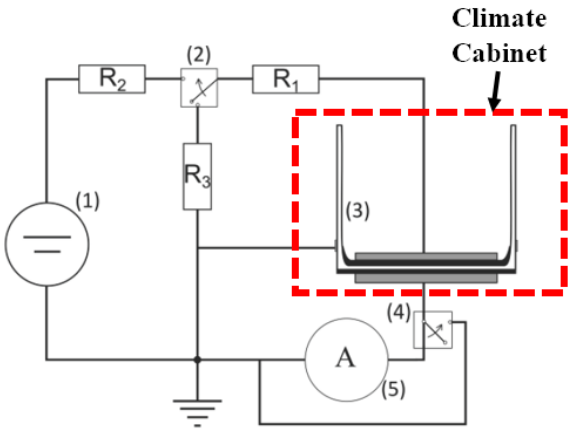

Figure 4.4. Advanced measurement setup [17]. (1) 35 kV FUG, (2) high voltage relay, (3) test object, (4) low voltage relay, (5) picoammeter. R_1, R_2 and R_3 are 50 MΩ, 500kΩ and 10 kΩ, respectively.

This measurement setup implements a climate cabinet for controlling the temperature. The current limiting resistor, R_1, limits the maximum short-circuit current to 0.03 mA at 1.5 kV (0.7 mA at 35 kV). Two major differences from the simple setup in Figure 4.3 is that 1) only the PEEK specimen and external electrodes are located inside the climate cabinet, and 2) the relays, picoammeter (Keithley 6485) and 35 kV DC source (FUG) are all controllable from a LabVIEW program. For the relays and the DC source, an Agilent switching unit and a Probus

executes the LabVIEW commands. The LabVIEW program also allow the user to set the desired noise-, polarization- and depolarization times, as well as desired test voltages (1-5 levels).

In addition to controlling the temperature, the climate cabinet also enables control over the relative humidity (RH). If the air surrounding the PEEK specimen have a high moisture content, water molecules could be a source of surface conduction [39]. Setting the RH to zero percent (0 %) should minimize this risk.

4.5 Test methodology

As the test temperatures and voltages have been determined, a methodology for testing the prepared PEEK specimens is required. Using the advanced setup, the best way to perform PDC measurements is to let the program run through the test voltages at one temperature at the time. As previously mentioned, it is important that there are no charges left in the material between the measurements. This means that the depolarization period have to be sufficiently long. In addition, since the polarization mechanisms are highly temperature dependent, beginning at the lowest temperature is important in regards to reducing the risk of inaccuracies in the measurements. The temperature in the specimens must also be allowed to stabilize before initiating measurements.

When performing measurements, some background noise is unavoidable. This means that the measurements must be post-processed to find the trendline of the polarization current, as well as filtering out possible disturbances. Having a 20 period average trendline (in Microsoft Excel) gives reasonable values for the polarization currents (Chapter 5).

The LabVIEW program used with the advanced allows the user to specify the noise time, which is a pre-polarization measurement to determine the background noise in the setup. If this noise level is non-zero, adding the average value to the measured polarization and depolarization current corrects the measurement data in regards to the background noise.

4.6 Measurements with insulation oil

According to unpublished work at SINTEF Energy Research, preliminary results show that measuring the amount of insulation oil absorbed in PEEK by the most common methods is not possible [40]. This means that a new, or different, measurement methods is required to determine the exact amount of oil sorption in PEEK. Thus, investigating the conductivity as a function of the amount of insulation oil absorbed is beyond the scope of this work.

A different methodology is to investigate the insulation oils' general effect on the conductivity in PEEK without measuring the weight gain. One approach to this is to expose the PEEK to the insulation oil and perform subsequent PDC measurements. Per Section 2.6, immersing the PEEK at elevated temperatures should increase the rate of sorption, which in turn should maximize its effect on the conductivity. To maintain comparability to the measurements with unexposed specimens, the test temperatures for the measurements with MIDEL should be the same as to those for unexposed PEEK. The PEEK can however be immersed at even higher temperatures, as long as it is cooled down before performing the PDC measurements. Any insulation oil on the surface of the PEEK will act as a parallel resistance, and drying it off is important.

The insulation oil selected for the experiments is MIDEL 7131. MIDEL 7131 is a synthetic insulation oil commonly used in transformers and subsea equipment, and has a breakdown voltage larger than 75 kV, and a volume resistivity larger than 30 GΩm at 90 °C [41].

An alternative to the test methodology above is performing PDC measurements while the specimens are submerged in MIDEL. This would require a different measurement setup to be developed, and is outside the scope of this work.

5 Results

5.1 The measurement circuits

Initial measurements with the simple setup in Section 4.4.1, revealed an undesirably high level of noise. The first step in reducing this noise were to eliminate any circulating ground currents in the setup. This include galvanic separation of all components, and a common point of grounding. The next improvement included screening of the measurement cable with a copper mesh, and rerouting any AC carrying cables in its vicinity to reduce contributions from electromagnetic disturbances. Since vibrations also can be a source of noise, the electrodes needs to rest on an anti-vibration layer or similar. A steel plate with four feet's and a thin layer of silicone is used for this purpose (Figure 5.12).

Despite all the improvements of the setup, the noise level remained undesirably high. A closer investigations of the equipment revealed that the fan motor in the heating cabinet contributes with a significant amount of noise. Figure 5.1 show a noise measurement where the heating fan is switched off towards the end.

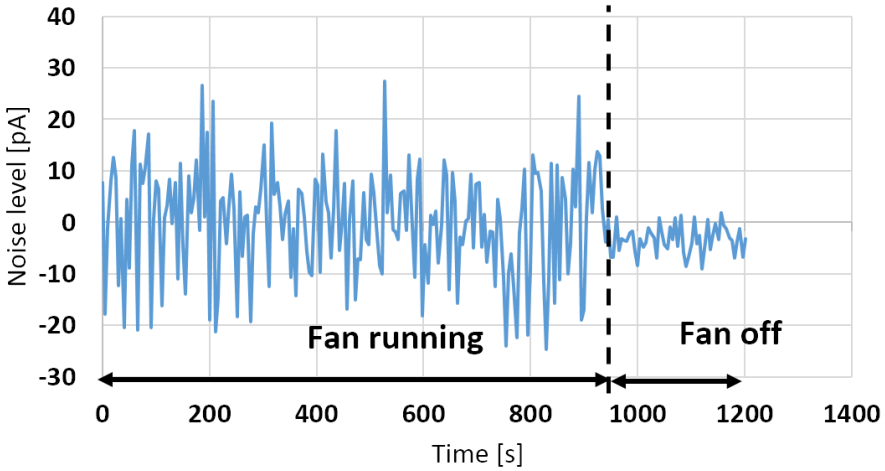

Figure 5.1. Noise level in the simple setup. Measurement for an ASTM specimen at 30 °C.

From Figure 5.1, it is evident that the fan motor have to be off for the noise levels to be within tolerable limits. Switching the fan off would however cause the temperature inside the heating cabinet to drop. If this temperature drop is small, switching the fan off for the last 5 minutes of the polarization period, could allow the resistive current to be found with reasonable accuracy. Measuring at the same height as the PEEK specimens, the corresponding temperature drop in the air at 30, 60 and 90 °C is shown in Table 5.1.

Table 5.1. Temperature drop in the simple setup, measured over a 5 minute time period with the heating fan switched off

	30 °C	60 °C	90 °C
Temperature Drop [°C]	0.8	3.2	5.4

Due to the heat capacity of the copper, it is reasonable to believe that the temperature in the electrodes drop less than in the air. If so, the temperature of the PEEK specimen between the electrodes would also have a lower temperature drop than inticated in the table.

Since the heating fan contributes with a significant amount of noise in the simple setup, similar investigations were performed for the advanced setup. Figure 5.2 show that the noise level in the advanced setup is independent of the fan motor.

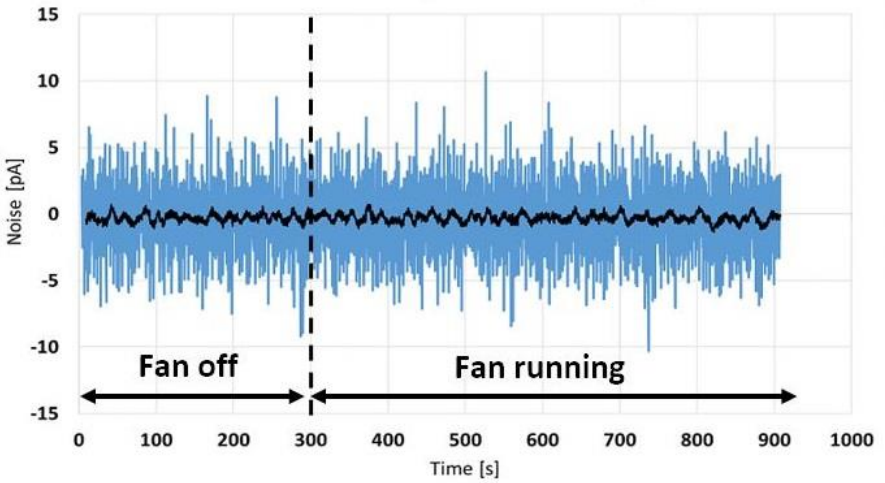

Figure 5.2. Noise in the advanced setup. The first 5 minutes are run with the fan switched off.

The noise level obtained in the advanced setup typically varies between 4 and 10 pA, and attempts to reduce this level with corona rings and extra screening of the measurement cable were unsuccessful. Since the noise level in the advanced setup is independent of the fan state switching it off during the measurements is not necessary. This means that the temperature is constant throughout the measurements, increasing the accuracy of the measurements compared to the simple setup. In addition, since the LabVIEW program enables the voltage levels to be automatically controlled, performing the measurements with this setup is a less tedious process. These advantages makes it desirable to perform all PDC measurements with the advanced setup.

5.2 Adjustment to the test temperature

The initial plan in Chapter 4 was to test at 30, 60 and 90°C, but during the first measurement at 90 °C, the evaporated aluminum vanished from the PEEK specimen:

Figure 5.3. ASTM specimen with damaged/vanished electrodes. The aluminum is intact at contact points with external measurement- and guard electrodes.

A second measurement at 90 °C revealed that this was not a one-time occurrence. From inspections of the electrodes prior to applying a voltage, it could be determined that this occurs when the voltage is applied. Several attempts at reproducing the same result in the simple setup failed, even at higher voltages and temperatures, linking this phenomenon to a property unique to the advanced setup.

Measurements at 80 °C did not result in the electrodes vanishing, and revising the test temperatures to 40, 60 and 80 °C makes it possible to stay with the advanced setup, as well as having an equal step size between the temperatures. The levels for the test voltages remained the same as planned.

5.3 Microscope investigations of the evaporated electrodes

As shown in Chapter 3, the evaporated electrodes play an important role when it comes to ensuring sufficient contact between the insulation material and the external electrodes. Furthermore, the shape and design also directly affects the distribution, directionality and control of the electric field. This means that examining the evaporated specimens to verify the design is important in regards to analyzing the measurement data.

From Figure 4.2, it is clear that there are some irregularities regarding the gap lengths and shapes. The gap length for both the specimen designs varies along the width or circumference of the specimens. For the Alternative specimen, the gap is also non-linear along the width of the electrode. By examining the specimens in a microscope, irregularities in the material and electrodes, as well as variations in the gap lengths can be determined.

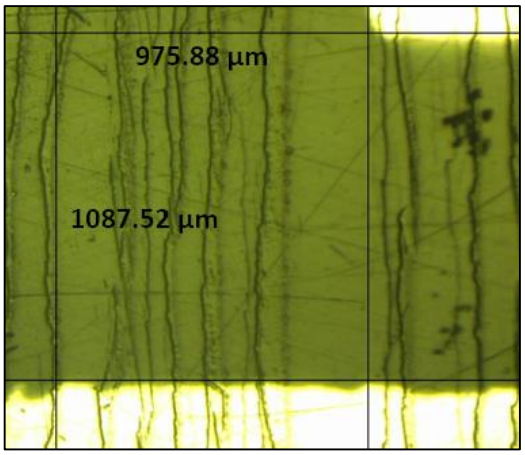

Figure 5.4. Microscope image showing roughness in the PEEK material. Image includes the measurement of the electrode- and guard gap for Alternative specimen number 2.

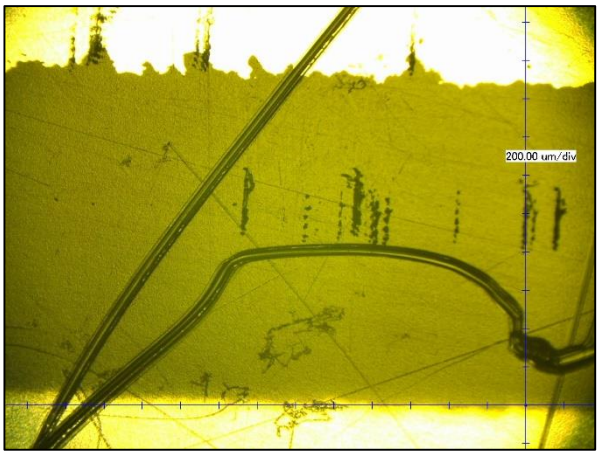

Figure 5.5. Microscope image showing gap length and damage for the middle section of Alternative specimen no. 3. Gap length is approximately 1630 µm (200 µm per tick).

Figure 5.4 show that one side of the specimen have scratches on both the evaporated and unevaporated sections. These scratches align with the initial rolling direction of the PEEK films, and occurs for all specimens. Unevaporated PEEK films show the same pattern of longitudinal scratches, pointing towards the possibility of this occurring during the manufacturing of the PEEK. Furthermore, Figure 5.5 show that scratches or damage also occur in other directions than longitudinal. The scratches looks more severe than in Figure 5.4, and due to them being unique, it is difficult to assess whether these occur prior to the evaporation or not. If occurring post evaporation, aluminum residue could be introduced in the gap. Figure 5.6 and Figure 5.8 show the minimum and maximum gap lengths for the ASTM and Alternative specimens.

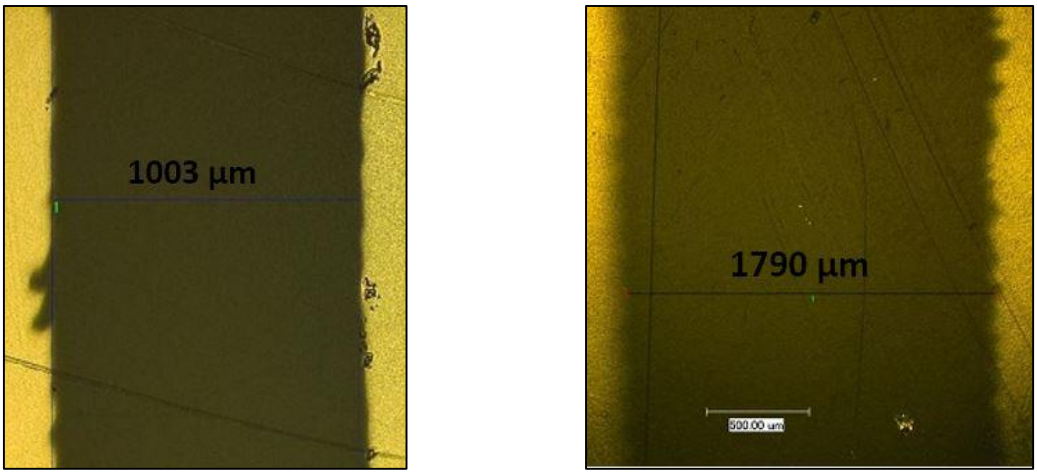

(a) (b)

Figure 5.6. Gap length of the ASTM specimens.
(a) Minimum gap length (specimen no. 4) and (b) maximum gap length (specimen no. 1).

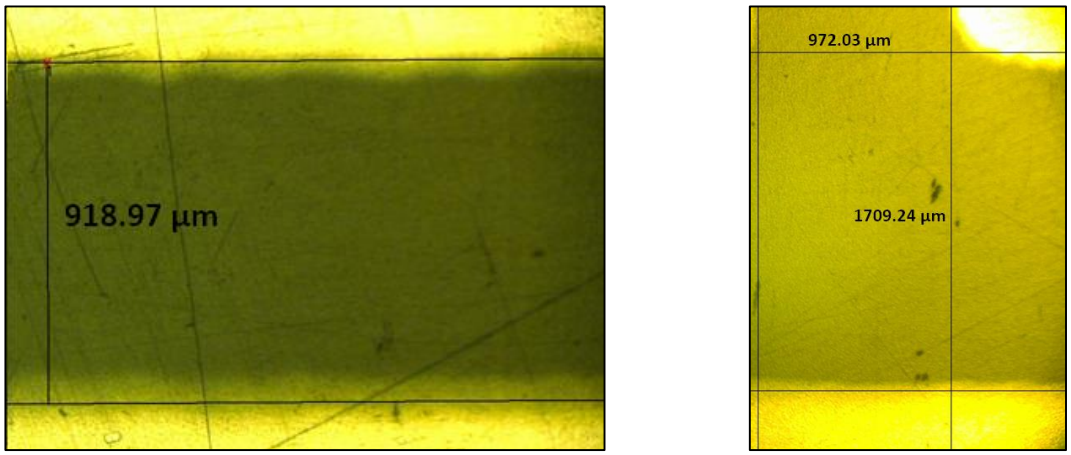

(a) (b)

Figure 5.7. Gap lengths of the Alterntaive specimens.
(a) Minimum gap length (specimen no. 4), and (b) Maximum gap length (specimen no. 1)

Figure 5.6 and Figure 5.7 show that the gap distances vary between 1003 and 1790 µm, and 919 and 1709 µm for the ASTM and Alternative specimens, respectively. This corresponds to a (total) variation of approximately 90 to 180 % of the planned 1 mm gap length. These deviations are significant, and it is necessary to take a closer look at the electrode rings and matrices used during the evaporation procedure.

Figure 5.8 and Figure 5.9 show that the width of the gap protection vary from one side of the ring/matrix to the other. This variation also seem to be in a trapezoid shape, suggesting that the matrices and electrode rings are cut at some angle during manufacturing. The figures also some roughness along the edges of the gap protection.

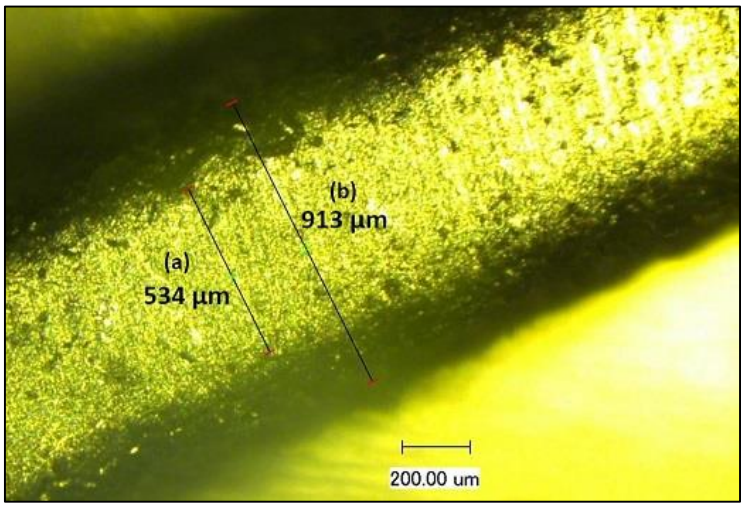

Figure 5.8. Approximate widths of the gap protection for an ASTM electrode ring.
(a) Width of the ring seen from above. (b) Width of the ring seen from below.

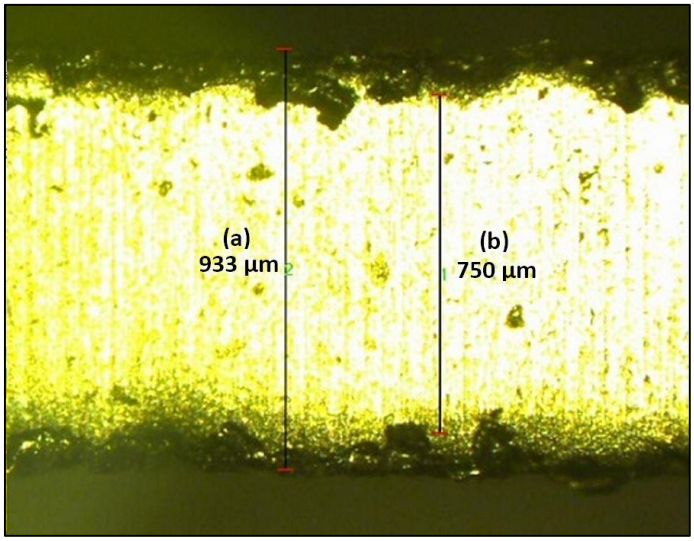

Figure 5.9. Approximate widths of the gap protection for the Alternative matrix.
(a) The width from below. (b) The width seen from above.

A close-up of Figure 4.1 b) shows that the non-linearity issue for the gaps on the Alternative specimens lies with the gap protection on the matrix:

Figure 5.10. Nonlinear gap protection for the Alterantive specimens' evaporation matrix. The dashed line visualises how much the gap protection flexes along the width of the specimen.

The gap protection in Figure 5.10 flexes easily towards either side of the matrix, but not up or down. A possible explanation for this could be that the steel plate is kept in a stressed position during the manufacturing of the matrix.

In addition to the geometrical shapes of the evaporated electrodes, the thickness might be a factor affecting the measurements. Figure 5.11 show a Profilometer image and corresponding X- and Y profile of the transition between the PEEKs' surface and the measurement electrode of an ASTM specimen. From the Y-profile, the height difference from the PEEKs' surface to the top of the evaporated electrode is approximately 0.8 µm.

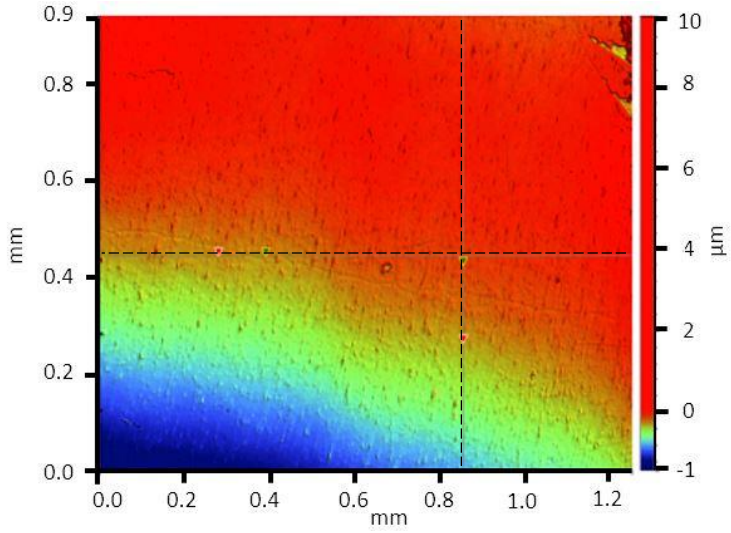

(a)

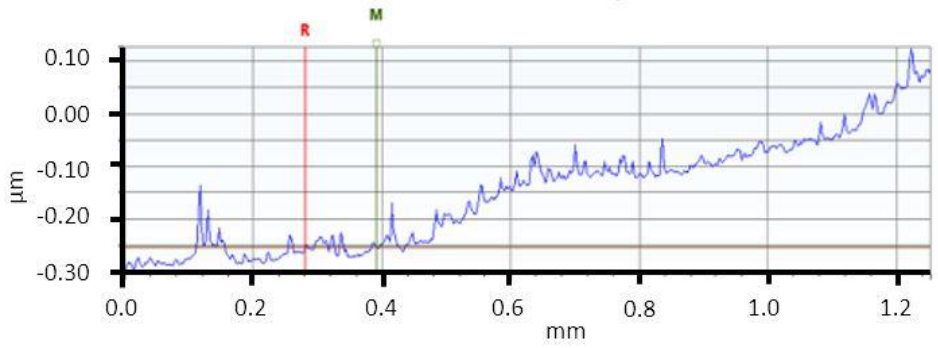

(b)

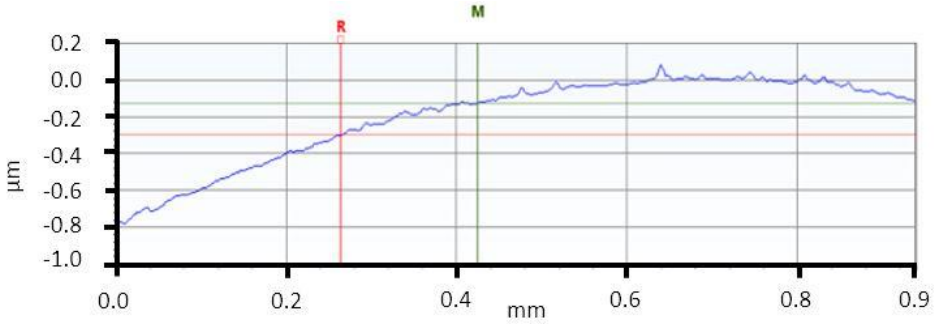

(c)

Figure 5.11. (a) Profilometer image of the evaporated electrode for an ASTM specimen. The red area is the top of the measurement electrode, and the blue area is the gap between the HV- and measurement electrode. (b) and (c) are the corresponding X- and Y-profiles showing the deviations in height along the dahsed lines in (a).

5.4 Measurements with ASTM specimens

Including the noise- and vibration reducing measures from Section 5.1, the ASTM specimen and external electrodes are set up as follows:

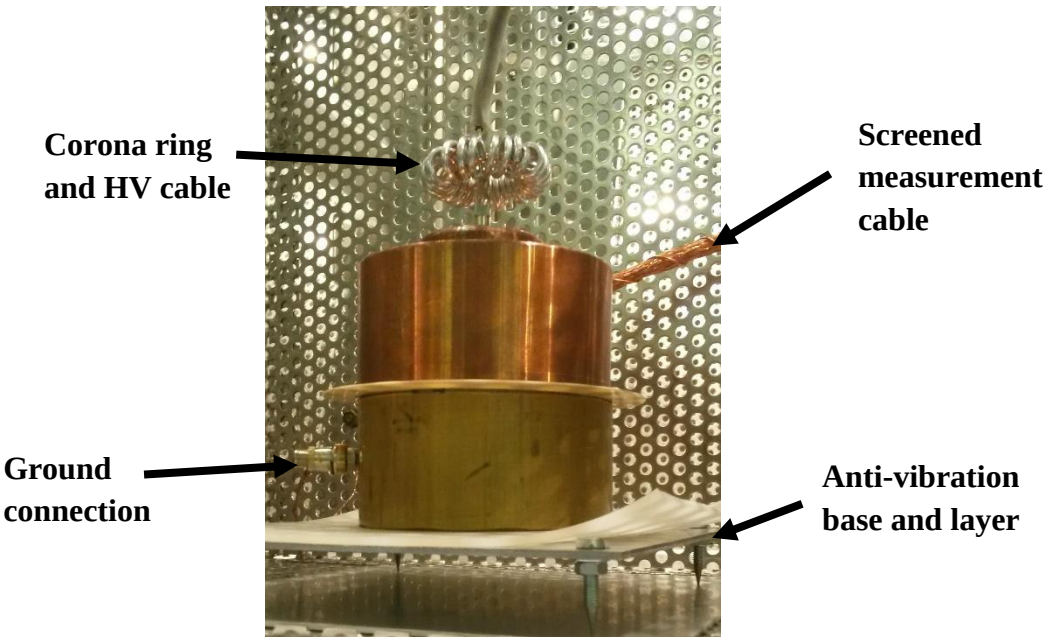

Figure 5.12. Measurement setup with the ASTM specimens

5.4.1 Capacitance and resistance

Connecting a capacitance meter or a Megger to the external electrodes allow the capacitance or resistance of the specimens to be measured. The results in Table 5.2 and Table 5.3 include the external electrodes, and corresponds to measurements at room temperature.

Table 5.2. Measured capacitance of the ASTM specimens.
Measured across the surface gap at room temperature..

Specimen No.	Capacitance, C [pF]
1	74.8
2	73.1
3	72.5
4	74.2
Average	73.7

Table 5.3. Measured surface resistance of the ASTM specimens at different Megger voltages. Measured at room temperature.

Specimen No.	Surface Resistance [GΩ]			
	500 V	1000 V	1250 V	1500 V
1	378	350	350	404
2	458	418	432	476
3	286	390	426	440
4	296	384	414	428
Average	**355**	**386**	**406**	**437**

Geometrical calculations

Since the measurement electrode is in contact with only one side of the specimens, there is an unknown amount of volume material contributing to the capacitance and surface resistance. This means that the ASTM specimens are not comparable to a parallel plate capacitor, which further means it is not possible to calculate the capacitance from the geometry.

5.4.2 PDC Measurements

An unknown issue with the measurement setup first caused the PDC measurements to be unsuccessful. Thus, the following results are from a second set of measurements. Due to the extensive amount of tests performed, Appendix E include additional figures to those presented in this Section. By using the methodology described in the beginning of this Chapter, the 40 °C measurements typically gave results similar to that of Figure 5.13. This suggests that the noise in the setup is dominating the currents obtained from the 40 °C measurements.

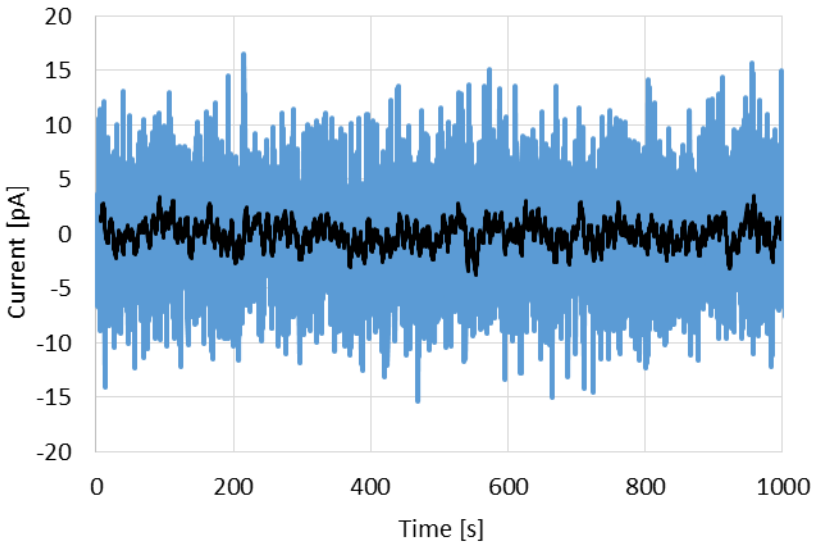

Figure 5.13. Polarization current for ASTM specimen no. 1 at 40 °C and 1500 V.

Then, since the 40 °C measurements generally are unreliable, adding 70 °C as a test temperature allows the requirement of three test voltages and temperatures in Chapter 4 to be fulfilled. Increasing the temperature beyond 40 °C typically causes the contribution from the polarization mechanisms on the current to become more visible, as well as obtaining a stable current towards the end of the measurement.

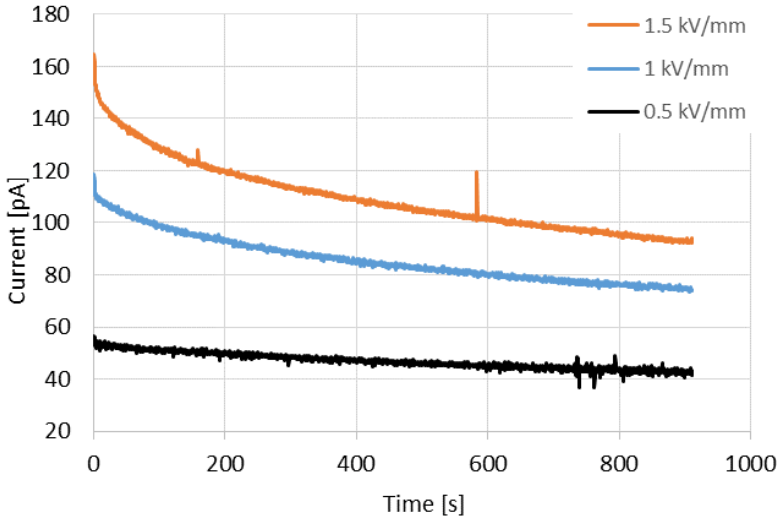

Figure 5.14. Polarization currents for ASTM specimen no. 4 at 80 °C.

Despite this being the general trend, specimen no. 3 behaves differently than the other; the 40, 60 and 70 °C measurements show little, or no, contribution from the polarization mechanisms or notable resistive current, while the currents at 80 °C is within the range of the background noise:

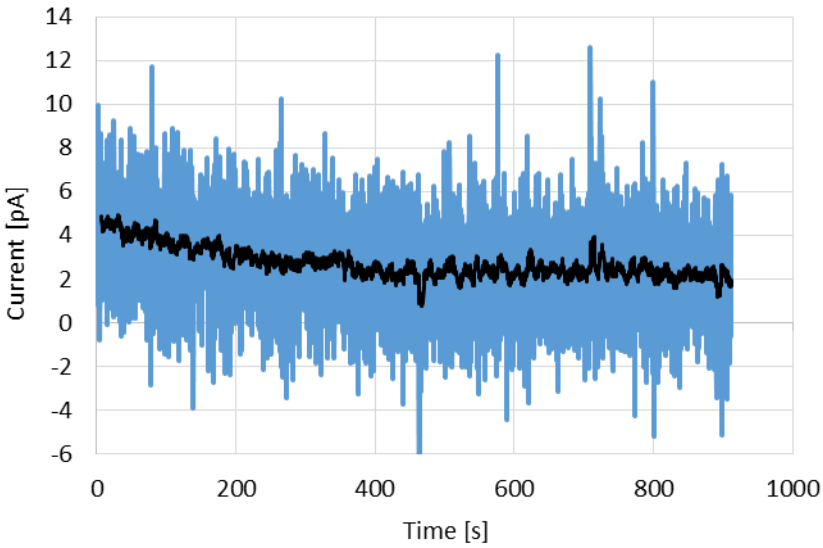

Figure 5.15. Polarization current for ASTM specimen no. 3 at 80 °C and 1000 V.

Some measurements also show large (positive) disturbances or peak values at varying frequency and time during the measurement (Figure E-6 and Figure E-7). If such contributions were included when averaging the last minutes of the measurement data, the resistive current would be too high. Consequently, the accuracy of the extracted current is increased by applying digital filters to the measurement data. For example, when processing the measurement data, it is possible to set disturbances that exceed a given limit equal to the previous value.

Table G-1 show the extracted currents for all specimens, at all temperatures and electric fields. In this table, the currents corresponding to the measurements at 40 °C and those of specimen no. 3 are very low, and by omitting these, the average resistive currents are as follows:

Table 5.4. Average resistive current for the ASTM specimens.

T [°C]	60			70			80		
E [kV/mm]	0.5	1.0	1.5	0.5	1.0	1.5	0.5	1.0	1.5
I_{DC} [pA]	8.1	14.8	19.6	44.0	94.0	155.4	85.6	120.5	146.9

Acknowledging that the measurement time for some specimens is too short, the currents might be lower than stated in Table 5.4. One method to investigate this more closely is to consider Eq. (2.13), where adding the polarization- and depolarization current should yield the resistive current. However, the depolarization current typically approaches zero more quickly than the polarization current approaches the resistive current (Figure E-10). This cause a mismatch between the waveforms, and the resulting current tend to follow the polarization current waveform. Thus, this approach is not viable for these measurements.

Another approach is to attempt curve fitting with MATLAB, which takes the measurement data as an argument, and approximates an exponential function. This function can then estimates a current at a time exceeding the measurement time. MATLAB has two exponential curve fitting methods, *exp1* and *exp2*, and their respective equations are as follows:

$$exp1 = a \cdot \exp(bt) \tag{5.1}$$

$$exp2 = a \cdot \exp(bt) + c \cdot \exp(dt) \tag{5.2}$$

where a, b, c and d are constants, and t is the time.

Eq. (5.1) and (5.2) does not contain any constant term, indicating that the limit for these exponential curves are zero. A fix for this is to write a function that subtracts a constant value from the measurement data before attempting the curve fitting (Appendix J). This constant then serves as an offset for the resulting curves, and corresponds to the value for the resistive current. Figure 5.16 show a reasonable good approximation for both exponential curves with a resistive current of 85 pA.

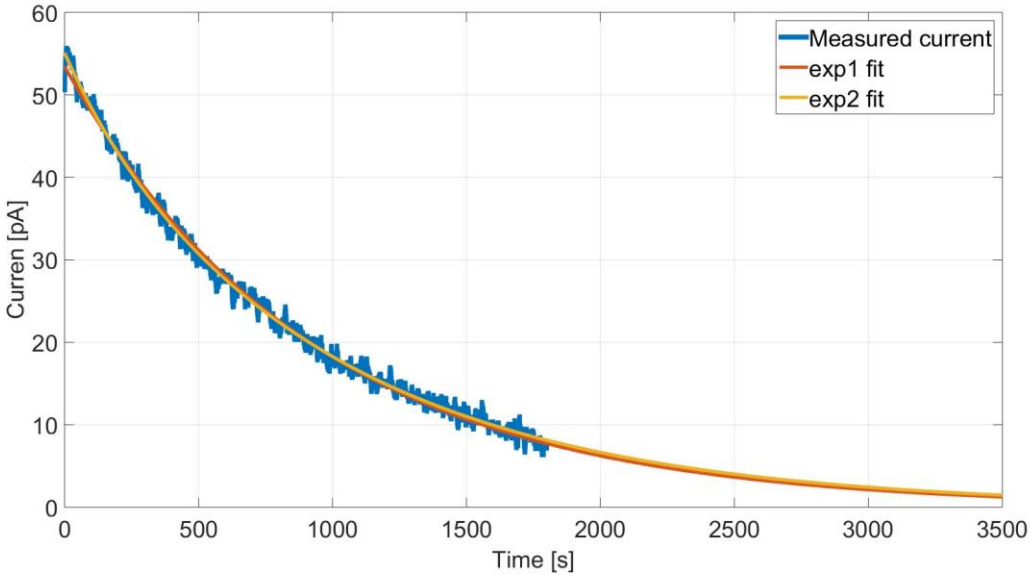

Figure 5.16. Curve fitting with an 85 pA offset at 70 °C and 500 V for specimen no. 1.

Most measurements does however result in large deviations between the two fitted curves, where the two-termed function is a better fit than the single-termed (Figure J-1). Furthermore, this approach does not work for all measurements, meaning it is not possible to approximate a lower current than previously extracted (Table J-1). The approximated current is generally 5 to 15 % lower than the measured one, and the overall trends are therefore the same as for the measured current.

5.4.3 Conductivity estimation

The surface conductivity is according to the ASTM standard determined by the geometrical parameters and the corresponding (measured) resistance of the specimen. The equation stated in the standard is the same as Eq. (2.5), with an effective surface cross section equal to the mean circumference of the gap. From the geometrical properties in Table 3.2, and the average values for the resistances in Table 5.3, Eq. (2.5) gives the following conductivities at room temperature:

Table 5.5. Calculated surface conductivity of the ASTM specimens at room temperature.

U_0 [V]	500	1000	1250	1500
σ_s [S/m]	$1.5 \cdot 10^{-14}$	$1.4 \cdot 10^{-14}$	$1.3 \cdot 10^{-14}$	$1.2 \cdot 10^{-14}$

The values in Table 5.5 show a very small overall change in the surface conductivity between the voltages, while the trend is decreasing with an increasing voltage.

In Section 5.3, the gap lengths have been found to deviate from the designed length of 1 mm. This causes the average gap length to be unknown, and a sensitivity analysis show that for each 0.1 mm increase in the average gap length, the surface conductivity changes by 9.8 %. In addition, using the values for the maximum gap length (approximately 1.8 mm), the conductivity changes by up to 78 %, and the subsequent range of the surface conductivity is $1.2 \cdot 10^{-14}$ to $2.7 \cdot 10^{-14}$ S/m.

Estimation from the PDC

Applying Eq. (2.14) to the resistive currents in Table G-1 results in positive surface conductivities between $1.5 \cdot 10^{-18}$ and $1.1 \cdot 10^{-13}$ S/m (Table G-2). The lowest conductivities typically corresponds to the 40 °C measurements and/or those of specimen no. 3. This means that omitting these contributes to a higher accuracy in the estimated surface conductivity. Figure 5.17 and Figure 5.18 show the surface conductivities as functions of electric field and temperature, respectively.

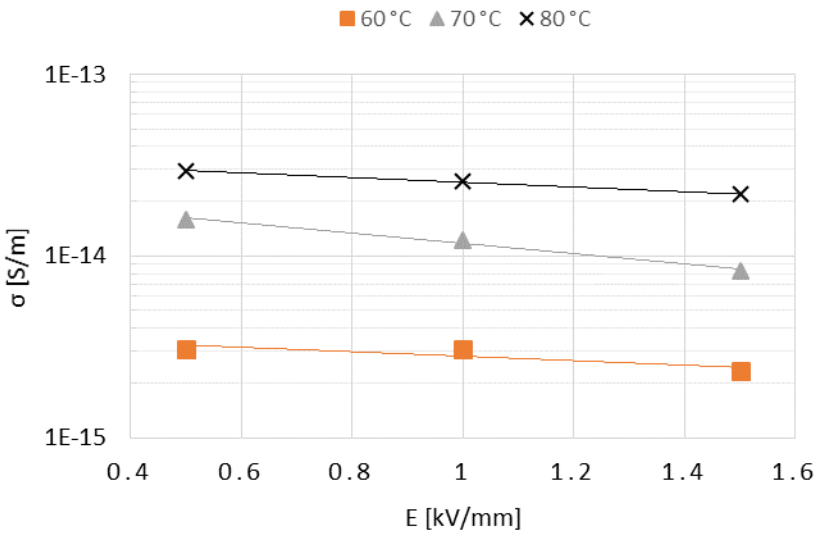

Figure 5.17. Surface conductivity of ASTM specimen no. 4 plotted against the electric field.

Figure 5.17 show that the surface conductivity is decreasing with the electric field, violating Eq. (2.3). From the addition of similar figures in Appendix H, possible reasons could be the voltage step is too small to give sufficient contribution to the surface conductivity, or that the obtained resistive currents are inaccurate.

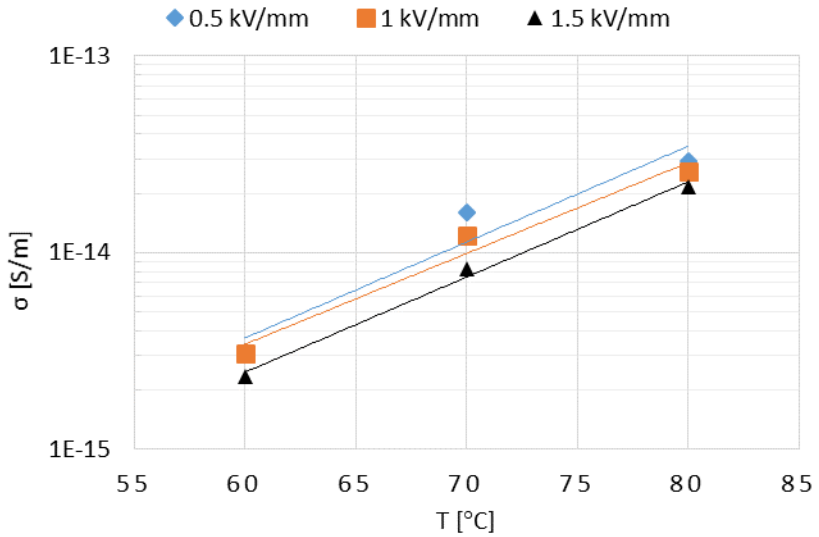

Figure 5.18. Surface conductivity of ASTM specimen no. 4 plotted agains temperature.

Figure 5.18 show that the surface conductivities' dependency on temperature is much larger than that of the electric field in the previous figure.

Estimating α, γ and σ_0

To estimate σ_0, Eq. (2.3) must be solved with known α and γ. Plotting the surface conductivity as a function of temperature or electric field, the corresponding trendline is a function of that variable alone:

$$Y(x) = A\exp(Bx) \tag{5.3}$$

where A and B are constants, and x is either the temperature or electric field strength.

This means that the slope of the trendline is a function of the temperature or electric field alone, making α or γ equal to B. The conductivity in the previous figures (and those in Appendix H) generally show negative exponential proportionalities. The best approach in estimating the parameters in Eq. (2.3) is then to plot the average conductivity of the specimens as functions of electric field and temperature. Inserting the capacitance and currents from Table 5.2 and Table 5.4 into Eq. (2.14) give the average surface conductivities in Table 5.6.

Table 5.6. Average surface conductivity of the ASTM specimens.

T [°C]	E [kV/mm]	σ_s [S/m]
60	**0.5**	$5.4 \cdot 10^{-15}$
	1.0	$5.0 \cdot 10^{-15}$
	1.5	$4.4 \cdot 10^{-15}$
70	**0.5**	$3.0 \cdot 10^{-14}$
	1.0	$3.2 \cdot 10^{-14}$
	1.5	$3.5 \cdot 10^{-14}$
80	**0.5**	$5.7 \cdot 10^{-14}$
	1.0	$4.0 \cdot 10^{-14}$
	1.5	$3.3 \cdot 10^{-14}$

Figure 5.19 show only one increasing trendline for the surface conductivity as a function of the electric field, making γ equal to 0.1628 kV/mm.

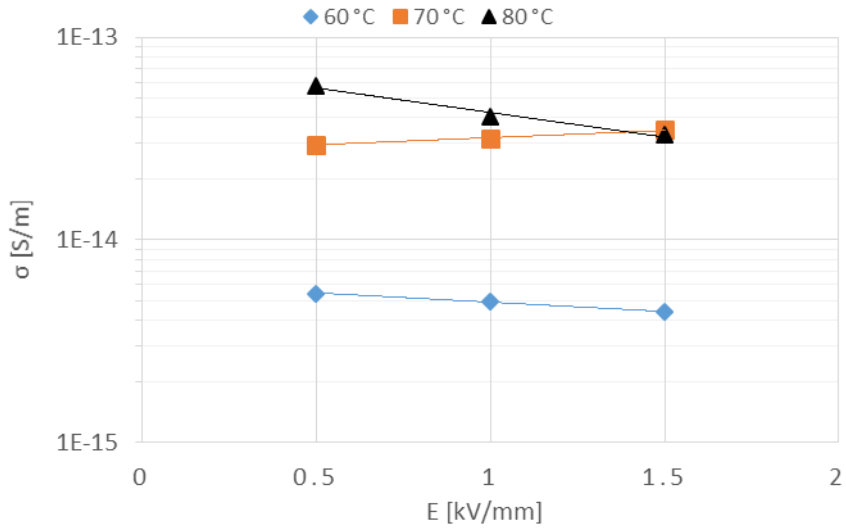

Figure 5.19. Average surface conductivity of the ASTM specimens plotted against the electric field.

The surface conductivity in Figure 5.20 show that the exponential trendlines are increasing with temperature, and it follows that all trendlines have positive values for α. Averaging these values then result in an α equal to 0.1079 1/°C.

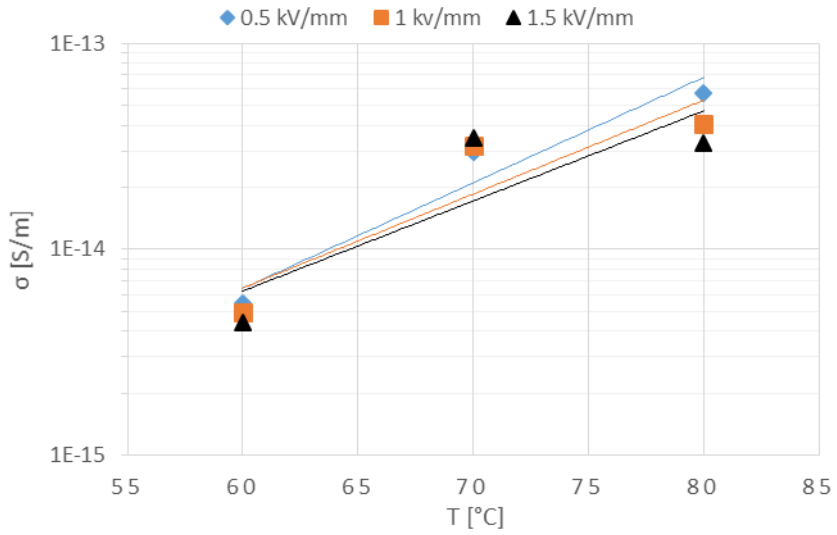

Figure 5.20. Average surface conductivity of the ASTM specimens plottet agaists temperature.

By using the estimated conductivities at 60 °C or above, for specimen 1, 2 and 4 in Table G-2, an average σ_0 is found by rearranging Eq. (2.3) and solving for σ_0.

Inserting all estimated parameters into Eq. (2.3), the resulting surface conductivity is:

$$\sigma_s = 9.1 \cdot 10^{-18} \exp(0.1079 \cdot T + 0.1628 \cdot E) \tag{5.4}$$

The value for γ deviates significantly from that indicated in Table 2.1, and to find the sensitivity of σ_0, using a $\gamma_{corrected} = 0.047$ (mean value corresponding to 70 °C in Table 2.1), result in an 11 % increase. Despite the increase in σ_0, the surface conductivity is generally lower due to $\gamma_{corrected} < \gamma$.

Table 5.7 show the surface conductivities found by solving Eq. (5.4) for 20 °C and the same test voltages as used for the PDC measurements.

Table 5.7. Estimated surface conductitivies at 20 °C.

U_0[V]	500	1000	1500
σ_s [S/m]	$8.5 \cdot 10^{-17}$	$1.0 \cdot 10^{-16}$	$1.1 \cdot 10^{-16}$

5.5 Measurements with Alternative specimens

The external electrodes for the Alternative specimens rest on a similar vibration dampening steel plate as for the ASTM setup, while six 10 mm thick Teflon plates separates the electrodes from ground potential and each other.

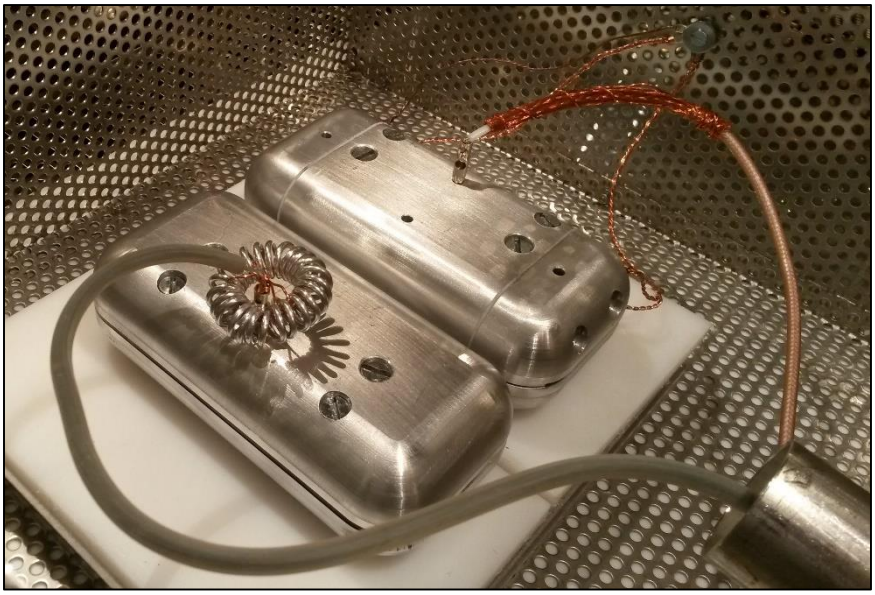

Figure 5.21. Measurement setup for the Alternative specimens

Due to the nonlinear gap of the evaporated electrodes (Figure 4.2 c), they cannot be entirely covered by the external electrodes. Consequently, the sphere gap analogy from Section 4.2 is invalidated. For comparison to the ASTM specimens in the previous Sections, four Alternative specimens were tested.

5.5.1 Capacitance and resistance

The capacitance and resistance of the Alternative specimens in Table 5.8 and Table 5.9 is measured the same way as for the ASTM specimens, including the external electrodes.

Table 5.8. Measured capacitance of the Alternative specimens at room temperature.

Specimen No.	Capacitance C [pF]
1	17.3
2	14.7
3	12.5
4	15.4
Average	15.0

The general design of the Alternative specimens is comparable to that of a parallel plate capacitor. Solving Eq. (2.15) with a cross section of 0.5 by 93 mm, a distance of 1 mm and a relative permittivity of 2.8, results in a capacitance of 1.2 pF. This value deviates significantly from Table 5.8, suggesting that a more complex approach is required to determine the actual capacitance through calculations.

Table 5.9 show that the resistance for the alternative specimens are outside the measureable range of the megger, which occur when the current is below the Meggers' detectable range.

Table 5.9. Measured surface resistance of the Alternative specimens at room temperature and different Megger voltages.

Specimen No.	Surface Resistance [GΩ]			
	500 V	1000 V	1250 V	1500 V
1 - 4	>510	>1020	>1280	>1520
Average	-	-	-	-

5.5.2 PDC measurements

While PDC measurements at 40 °C does not have a visible contribution from the polarization mechanisms, increasing the temperatures to 60 °C and above does:

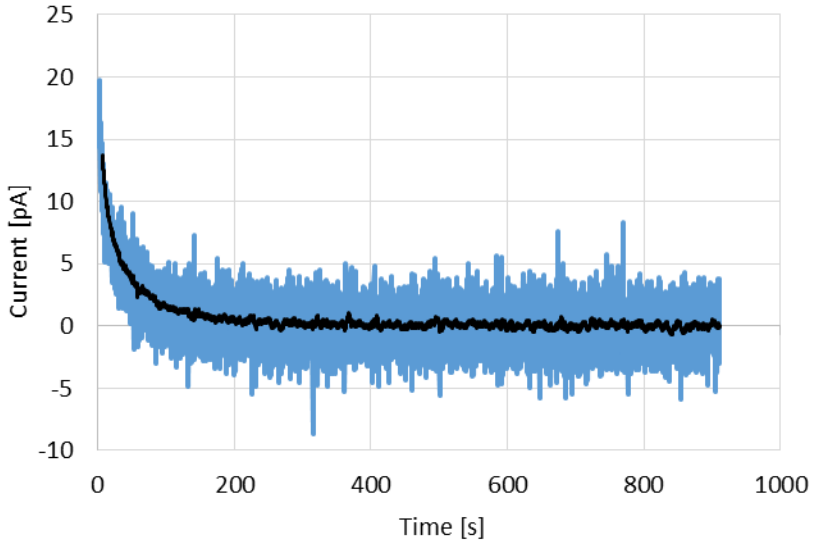

Figure 5.22. Polarization current for Alternative specimen no. 3 at 60 °C and 1000 V.

Even if the time dependent polarization is visible for the measurements at higher temperatures, the current is located inside the range of the noise towards the end of the measurement. The resistive currents in Table G-3 show that most currents are generally very close to zero, while some of them take on negative values.

5.5.3 Conductivity estimation

Since the resistances for the Alternative specimens are unknown, calculating the corresponding conductivities from the standard method is not possible.

Estimation from the PDC measurements

Applying Eq. (2.14) to the resistive currents in Table G-3, the (positive) surface conductivities are between $1.5 \cdot 10^{-18}$ and $1.5 \cdot 10^{-15}$ S/m (Table G-4). Figure 5.23 and Figure 5.24 is obtained by plotting the surface conductivities against the electric field and temperature.

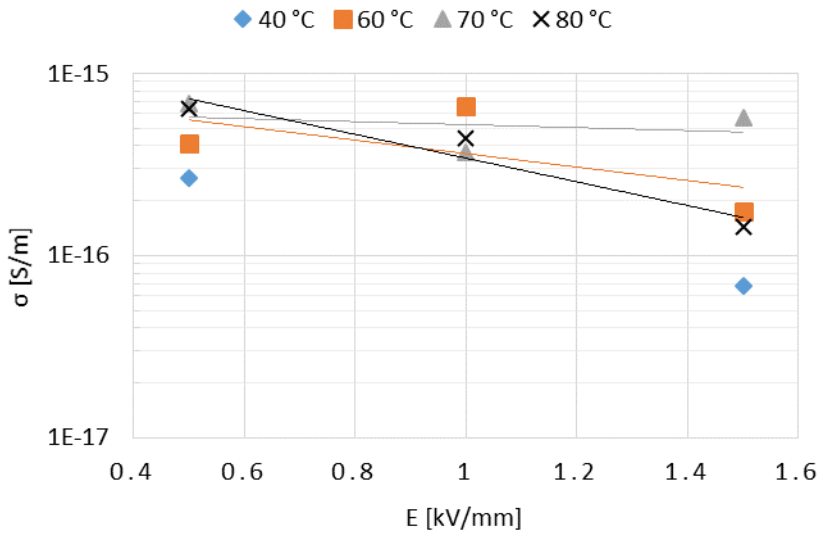

Figure 5.23. Surface conductivity for Alternative specimen no. 3 plotted against the electric field. The trendline for 40 °C cannot be accurately estimated due to the lack of datapoints.

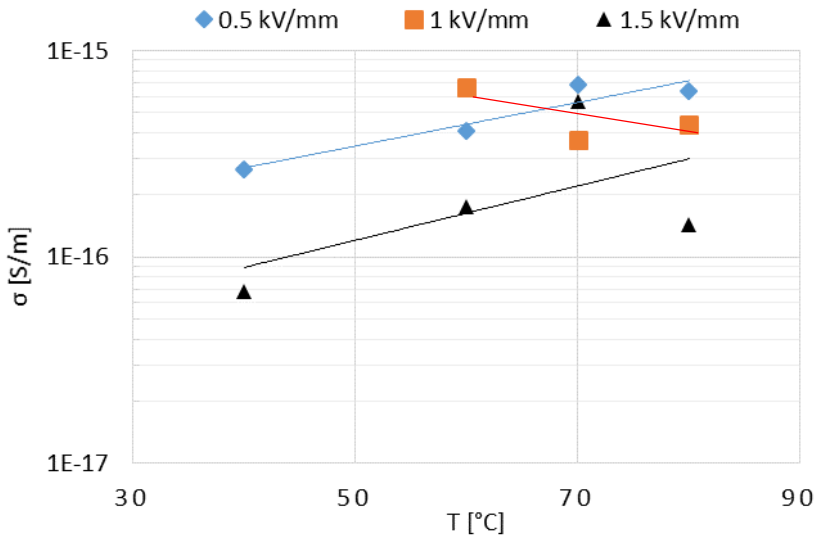

Figure 5.24. Surface conductivity for Alternative specimen no. 3 plotted against temperature.

Figure 5.23 show a negative exponential proportionality between the conductivity and electric field strength, violating Eq. (2.3). Despite the slightly increasing trend for 0.5 and 1.5 kV/mm in Figure 5.24, the conductivities seem to cluster around $4 \cdot 10^{-16}$ S/m. These observations indicates that the measured currents are too low to yield usable results.

5.6 Oil measurements

By using the methodology described in Section 4.6, both ASTM and Alternative specimens were immersed in MIDEL 7131 at 80 °C for 8 days. An attempt at determining the amount of absorbed MIDEL by weighing the specimens were unsuccessful, thus supporting the preliminary findings at SINTEF Energy Research [42]. The weighing scale measures in grams, with an accuracy of five (5) decimals, and the average weight of the ASTM and Alternative specimen both prior to, and after, the exposure to MIDEL were 4.81507 and 2.93265 g.

The PDC measurement with ASTM specimen no. 1 at 80 °C resulted in a noise between 50 and 200 pA (Appendix K), which is a much higher noise than observed with previous PDC measurements. Investigating the specimen after the measurement revealed damage on the evaporated HV- and measurement electrodes (Figure K-4 a). By lowering the test temperature to 70 °C, the background noise in the subsequent measurements were within normal range:

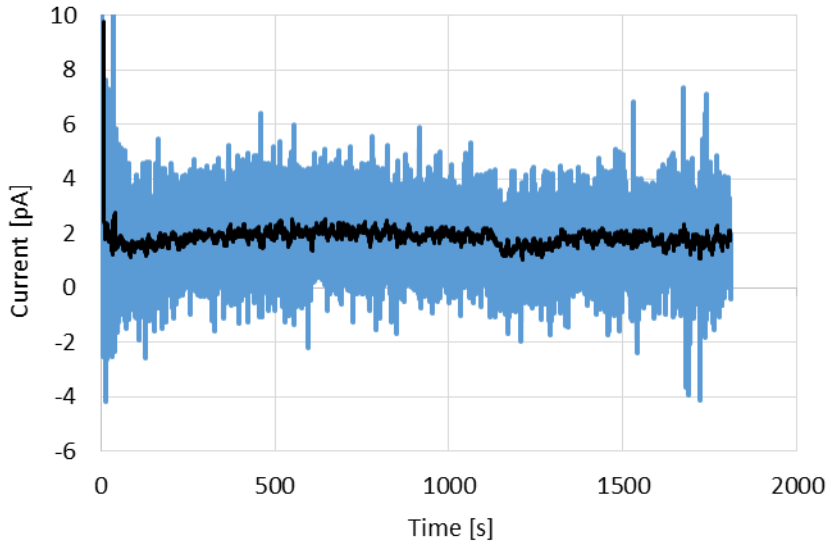

Figure 5.25. Polarization current for ASTM specimen no. 4 at 70 °C and 1500 V after exposure to MIDEL.

Figure 5.26 show the resistive currents and estimated surface conductivities prior- and post exposure.

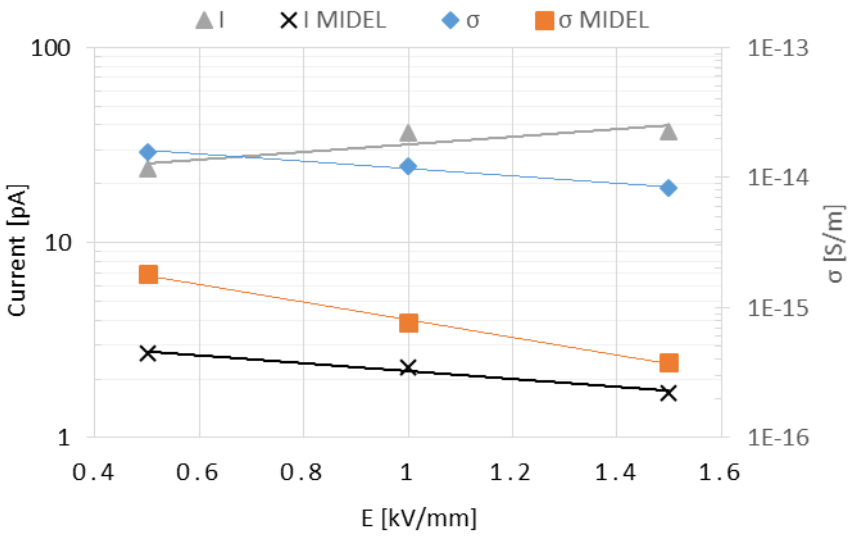

Figure 5.26. Resitive current and surface conductivity at 70 °C
for ASTM specimen no. 4, before and after exposure to MIDEL.

From Figure 5.26 it is evident that the current, and hence the surface conductivity, is lower after exposure to MIDEL. Since the current after the exposure to MIDEL is lower than prior to exposure, MIDEL is apparently contributing to an overall higher surface resistance. Despite lowering the test temperature, investigations of the evaporated electrodes revealed damage to the ground electrode (Figure K-4 b).

6 Discussion

6.1 Vanishing electrodes

In the first test at 90 °C with the advanced setup, the unprotected parts of both the evaporated HV- and measurement electrode vanished (Figure 5.3). Attempts to recreate this in the simple setup revealed that the phenomenon is unique to the advanced setup. The only significant environmental difference between the two setups is a relative humidity of 37 and 0 % for the simple and advanced setup, respectively. Since the aluminum vanishes, a chemical process is most likely taking place when a voltage is applied. Thus, this process, and its severity, could be dependent on the current or electric field. Having a RH of zero should eliminate the possibility that humid air contributes with moisture to any processes. A different source of moisture could be the PEEK itself, but the degassing of the specimens prior to the evaporation procedure attempted to account for this uncertainty. It is also reasonable to assume that the severity of the damage is dependent on the thickness of the evaporated electrodes. A thin layer means that there is a lower amount of aluminum molecules that can adhere to the PEEK, as well as to each other. The measured thickness of the aluminum electrodes were 0.8 μm, which in comparison is between 1 and 13 % of the typical thickness suggested by the ASTM standard.

The evaporated electrodes also began to vanish during PDC measurements with specimens exposed to MIDEL at 70 and 80 °C. Since the diffusion mechanisms in Section 2.6 are strongly dependent on temperature and concentration of penetrant, it is reasonable to assume that desorption of MIDEL can take place during the measurements. If so, this suggests that MIDEL enhance the chemical process thought to be responsible for the electrode vanishing. Another possibility could be that the electrodes are damaged when the drying off MIDEL from the specimens prior to the measurement.

Due to the lack of statistical data for this phenomenon, additional testing is required to investigate this matter in more detail.

6.2 Electrode gaps and shape

Microscope images in Section 5.3 revealed significant variations in the gap lengths. The total variation in length ranges between 90 and 180 %, and varies along the width or circumference of the specimens. This makes it impossible to determine the average gap length. The microscope images also show some roughness along the evaporated electrodes' edges that is comparable to the roughness observed on the gap protection on the electrode rings and matrices. Combined, the variation and roughness causes the general shape of the gap to deviate significantly from the planned design. A consequence of this deviation is a possibility for the electric field becoming inhomogeneous across the gap, affecting the exponential equations for the surface

conductivity in Section 2.2. Improvements to these issues require higher accuracy in the manufacturing process of the evaporation accessories.
Figure 5.5 show that there are scratches or irregularities in the PEEK that span both the evaporated and unevaporated parts of the specimens. If these occur prior to evaporation, the aluminum could adhere to these scratches so that it protrudes into the PEEK. On the other hand, if scratches occurs post-evaporation, there is a risk of aluminum residue in the gap, affecting the electric field or conduction across the gap.

6.3 PDC measurements

The climate cabinet used with the advanced setup keeps the temperature in the air at a seemingly very stable level. Several sensors control this temperature, but the airflow and (forced) convection could cause some discrepancies between the temperature in the upper and lower region of the cabinet. This means that there could be some deviations between the set temperature in the cabinet and the actual temperature in the PEEK specimens. However, the stability of the climate cabinet causes this effect to be negligible compared to other uncertainties in Chapter 5.

6.3.1 Noise

The background noise in the setup is typically in the range of 5 to 10 pA. Since this noise level is unaffected by the applied voltage, it is most likely dominated by other components in the setup or external electromechanical disturbances. Further reduction of the background noise would be beneficial for PDC measurements where the current is in the range of the noise. In addition to the low background noises, larger disturbances can occur during the polarization period (Appendix E), but are generally easy to filter out. However, some of these occur at i.e. 70 °C and 1000 V and not at 80 °C and 1500 V, and a suggested explanation is that discharge activity or conductive channels cause the aluminum to vanish as in Section 6.1, reducing the effective gap length in the subsequent measurement. Microscope investigations of the electrode edges could not support this explanation, but due to the possible connection to the vanishing electrodes, further investigation into this matter is necessary.

To lower the background noise, it could be beneficial to reduce the distance to the Faraday cage. A possible solution would be to manufacture a metal encapsulation for the specimen and external electrodes. Having an encapsulation would also enable the implementation of a mechanical system to control the force exerted on the electrodes. Such a mechanical system could possible eliminate issues arising from the varying stiffness and curvature of the PEEK specimens.

6.3.2 ASTM specimens

There is a large variation in the resistive currents at the same temperatures and electric fields for the different specimens. Excluding the 40 °C measurements, as well as those of specimen no. 3, the currents in Table G-1 deviate by up to 113 % from the average currents in Table 5.4. The corresponding average deviation is 45 %. Possible explanations for the large variations is issues with the measurement setup or geometrical differences between the specimens.

As all components (besides the specimens) are the same for all measurements. If the resulting currents are larger than the background noise and free of disturbances, it is evident that noise cannot be the source for the large deviations between the specimens.

From the variation in gap shapes discussed in Section 6.2, it follows that the average length, and thus surface resistance, can vary significantly between the specimens. Such variation in the surface resistance also cause similar variations in the current, linking the large inter-specimen deviation to the geometrical properties.

Due to the short measurement time, the currents in Table G-1 are not entirely resistive. In an attempt to find the resistive current, adding the polarization- and depolarization currents together resulted in a current almost identical to the polarization current. The depolarization current approaches zero much quicker than the polarization current approaches the resistive current. This means that the time constant for the exponential decay function in Eq. (2.12) differs between the polarization- and depolarization current. A possible explanation could be that the surrounding air contributes differently to the polarization- and depolarization mechanisms.

A different attempt to account for the currents not being entirely resistive were to approximate the resistive current by curve fitting in MATLAB. The maximum deviation did however only became marginally lower (107 %), while the average deviation remained the same as for the measured currents. In addition, the approximated currents turned out to be 5 to 15 % lower than the measured ones. This means that the same trends occur for the approximated and measured currents.

6.3.3 Alternative specimens

The currents measured for the Alternative specimens are typically within the range of the background noise for all temperatures. Since the design of the Alternative specimens should yield a current that is similar to that of the ASTM specimens, there has to be significant inaccuracies or errors with the specimens, external electrodes or setup.

The gaps on the Alternative specimens are non-linear along the width. This means that the external electrodes cannot follow the evaporated electrodes' edges. Consequently, the electrode gap is more similar to the gap on the ASTM specimens than a sphere-gap, and the argument for a homogeneous electric field in Section 4.2 might not hold. Being more similar to the gap of the ASTM specimens can however not be the reason for the current deviating from the ASTM specimens.

Following the same logic as in the previous Subsection, the geometrical properties of the specimens seem to have the greatest impact on the currents. For the current to be lower for the Alternative specimens than for the ASTM specimens, the average gap lengths, and thus resistances, have to be higher. Additionally, the currents are outside the Meggers' detectible range when attempting to measure the surface resistance of the Alternative specimens, further supporting that the surface resistance is higher for these specimens.

Figure 3.8 show a symmetrical electric field for the Alternative specimens. The electric field is also significantly lower at the edge of the HV electrode than for the ASTM specimens. This could point to less risk of discharges or other effects that occur due to a high local electric field strength. Combined with the findings from the specialization project, the electrode design of the Alternative specimens is believed to be better than the circular layout for the ASTM specimens. Thus, improving upon the uncertainties presented in this work should be a priority for future work.

6.3.4 Oil measurements

The 80 °C PDC measurement of the PEEK specimen exposed to MIDEL had noise in the range 50 to 200 pA, which is significantly more than the 5-10 pA noise level normally observed in the setup. The large noise is most likely a byproduct of the chemical process and subsequent damage on the evaporated HV- and measuring electrodes. Figure 5.26 show a considerably lower current for the exposed specimen, and it is therefore reasonable to assume that the MIDEL is contributing to a higher surface resistance. This is also to be expected, but additional measurements would be required to verify the results.

6.4 Conductivity estimation

Following the geometrical method of the ASTM standard, the conductivity is between $1.2 \cdot 10^{-14}$ and $1.5 \cdot 10^{-14}$ S/m (Table 5.5). The sensitivity analysis show an increase in the surface conductivity of 9.8 % for each 0.1 mm increase in the average gap length, which for the largest gap length corresponds to a maximum of $2.7 \cdot 10^{-14}$ S/m (178 %). This means that the geometrical calculations are highly sensitive to variations in the gap lengths, and a higher accuracy for the manufacturing procedure of the evaporation equipment in required. Despite the uncertainty from the sensitivity analysis, the conductivity seems to remain in the low 10^{-14} S/m for the standard method. Since measuring the surface resistance of the Alternative specimens resulted in a current outside the Meggers' range, it is possible that the current is near the detectible limit for the ASTM specimens. This means that the current detected by the Megger may not be entirely accurate, causing subsequent uncertainties in the measured surface resistances. Furthermore, the manufacturer of the PEEK used in this work suggests a surface conductivity of 10^{-15} S/m. As with the ASTM standard, this value is found from the geometrical properties and measured resistance, and introduce a large uncertainty to either the values found in this work or the standard methods themselves.

6.4.1 Estimation from the PDC

The large variation in current between the specimens cause similar variations in the surface conductivities, which is reflected by the distance between the trendlines in Figure H-4. In an attempt to compensate for these variations, the surface conductivities are estimated from the average current and capacitances. Using the average currents may or may not be the best option; only three ASTM specimens resulted in usable currents, meaning that the average current could still deviate significantly from actual values. Furthermore, since the currents extracted from the PDC measurements are generally not entirely resistive, the surface conductivities would in reality be lower than the estimates. Using the average capacitances introduce a 1 % uncertainty to the obtained surface conductivities, but is negligible compared to the uncertainty introduced by the currents.

The attempt at approximating the resistive current in Section 5.4.2 revealed that a two-termed exponential function fit better with the polarization current than a single-termed. This suggests that the conduction mechanism in PEEK actually follow a two-termed exponential function, such as ionic hopping from Section 2.2.1. Due to the short measurement time, any deviation between the single- or two-termed function and the resistive current is unknown. This means that assessing the validity of the empirical equation for PEEK from these measurements is difficult.

6.4.2 Estimating α, γ and σ_0

The estimated surface conductivities are in the range of $4.4 \cdot 10^{-15}$ to $5.8 \cdot 10^{-14}$ S/m. From the corresponding trendlines with positive exponential relationships to the temperature and electric field, α and γ are 0.1079 1/°C and 0.1628 mm/kV, respectively. For these values, σ_0 is estimated to be $9.1 \cdot 10^{-18}$ S/m. Solving the empirical equation, Eq. (2.3), resulted in a surface conductivity between $8.5 \cdot 10^{-17}$ and $1.1 \cdot 10^{-16}$ S/m at 20 °C and 500 to 1500 V. As per Section 5.4.3, a corrected value of $\gamma = 0.047$ marginally reduce the lower limit to $8.3 \cdot 10^{-17}$ S/m. Overall, the surface conductivity for the PDC method is more than two decades lower than the standard method. This also means that the standard- and PDC method both deviate from the manufacturers' suggested surface conductivity by one decade.

Given a 1 mm gap, and a corresponding electric field of 1.5 kV/mm, the contribution from αT is larger than γE as long as the temperature is higher than 2.3 °C ($\gamma = 0.1628$). In Eq. (2.3), the maximum contribution from $\exp(\gamma E)$ is 1.27, while the contribution from $\exp(\alpha T)$ at 40 °C is 74.9. This means the contribution from the test voltages on the surface conductivity is negligible compared to the temperature in the measurements, confirming previous assumptions. Such a low contribution could also be the reason why the surface conductivities found in this work tend to decrease as the voltage increases.

7 Conclusion

The focus of this thesis has been on evaluating two methods for estimating the surface conductivity of insulation materials. The first method has been a standard method involving the geometrical properties and measured surface resistance. The second method has investigated the dielectric response through PDC measurements. The material investigated is PEEK, and the specimens used have two distinct designs; one circular design suggested by the ASTM standard (ASTM specimens), and one rectangular design developed for comparison (Alternative specimens). Despite the unsuccessful PDC measurements with the Alternative specimens, the design is believed to be more suited than the circular design of the ASTM specimens.

The gap lengths for both designs vary along the width (or circumference), with a maximum length of 170-180 % of the intended length. Such variations made it impossible to determine the average gap lengths. These variations also cause the electric field across the gap to become inhomogeneous, which in turn could invalidate the exponential relationships between the (surface) conductivity and electric field. To improve upon the variations in gap lengths and geometrical properties, higher accuracy in the manufacturing process of the evaporation accessories is required.

Despite the similar variations in the gap length, attempts to measure the surface resistance of the Alternative specimens ended with currents below the detectable limit of the Megger. Thus, only the prepared ASTM specimens were applicable to the standards' method. The resulting surface conductivity for the standard method were found to be between $1.2 \cdot 10^{-14}$ and $2.7 \cdot 10^{-14}$ S/m. Due to the low sensitivity of the Megger, currents close to the detectable limit could introduce uncertainties to the standard method.

The temperatures and voltages used for the successful PDC measurements were 60, 70 and 80 °C and 0.5, 1.0 and 1.5 kV. The corresponding surface conductivities were found to be between $4.4 \cdot 10^{-15}$ and $5.4 \cdot 10^{-14}$ S/m. By fitting these values to the empirical equation $\sigma = \sigma_0 \exp(\alpha T + \gamma E)$, the parameters α, γ and σ_0 were found to be 0.1079 1/°C, 0.1628 mm/kV and $9.1 \cdot 10^{-18}$ S/m. The contribution from γE to the surface conductivity has been proven to be negligible compared to αT for the voltages and temperatures in this work. Solving the empirical equation at 20 °C (room temperature), resulted in a surface conductivity between $8.3 \cdot 10^{-17}$ to $1.8 \cdot 10^{-16}$ S/m, which is more than two decades lower than for the standard method. The short measurement time for the PDC measurements means that the currents, and thus the estimated surface conductivities, could be lower than estimated, increasing the deviation between the two methods even further.

To investigate the general effect of insulation oil on the surface conductivity, the ASTM specimens were exposed to MIDEL 7131 for 8 days. This resulted in values between $3.8 \cdot 10^{-16}$ and $1.8 \cdot 10^{-15}$ S/m at 70 °C, which is significantly lower than for the unexposed specimens. When the PEEK specimens were exposed to MIDEL the evaporated electrodes began to vanish during the PDC measurements at 70 and 80 °C. The same occurred at 90 °C for unexposed specimens, suggesting that MIDEL enhances some chemical process at the surface of the PEEK. In addition, the thickness of the evaporated electrodes were measured as thin as 0.8 μm, and could be a contributing factor to the electrodes vanishing. To address whether this phenomenon is damaging the PEEK or not, further testing with similar specimens and specimens with thicker evaporated electrodes is required.

By using a curve-fitting tool in MATLAB, both a single-termed and a two-termed exponential function were fitted to the polarization currents. The results revealed that a two-termed exponential function is a better fit than a single-termed. This indicates that the conduction mechanism in PEEK follows a two-termed exponential function, such as ionic hopping. Due to the relatively short measurement time, it is not possible to determine whether or not the single- and two-termed exponential curves deviates from what would be the resistive currents. This means that it is impossible to assess the validity of the empirical equation (single-termed) from these measurements.

According to the manufacturer of the PEEK used in this study, the surface conductivity is around 10^{-15} S/m, which puts it directly between the values found from the standard- and PDC method. Both methods have significant uncertainties corresponding to the geometrical properties and measured values, making it difficult to determine which method is better. Additional measurements and specimen designs is required to get more reliable estimates from both methods, but by improving upon the uncertainties presented in this work, the sensitivity of the PDC method could possibly make it superior to the ASTM standard.

8 Future work

A goal for future work would be to perform additional measurements with longer measurement periods to increase the reliability of the estimated parameters and values. This also includes being able to assess the empirical equations' validity for the surface conductivity in PEEK. Improvements to the measurement setup and specimens is also a natural progression. Being able to use the Alternative specimens for PDC measurements would be beneficial for comparisons, and improving the method or conducting a more thorough investigation to why the measurements were unsuccessful, should be a priority.

The phenomenon causing the evaporated electrodes require further investigations. Determining the reasons for this phenomenon and the mechanisms behind it could give important information for the characterization of PEEK (or other insulation materials) subjected to HVDC (and insulation oil).

Further study of the conduction mechanisms and diffusion behavior in PEEK will also be important next-steps in the characterization of the surface conductivity. Determining the behavior of the conduction mechanism could also assist in the evaluation of the empirical equations validity.

The dimensions of the matrices, electrode rings and geometries of the evaporated electrodes revealed that there are significant deviations from the design parameters. These deviations are also the cause of the highest uncertainties in both the current measurements and the estimations of the surface conductivities. Improving upon the evaporation procedure and the manufacturing process of the accessories could in turn greatly increase the reliability of the results.

During the measurements, two parameters that affects the results are the noise and the curvature of the PEEK specimens. To deal with these issues, designing an encapsulation with a mechanical system for controlling the force exerted on the electrodes could be beneficial. In this work, air serves as the medium surrounding the specimens, limiting the applied voltage. By finding an alternative to air, higher electric fields are possible, which in turn could increase the accuracy of the estimated value for the electric field coefficient (γ). An investigation into whether air is the reason for the deviation between the time constants (τ) for the PDC could also be necessary.

9 References

1. IEA. *Renewables*. 2015 [cited 2015 19th of May]; Available from: http://www.iea.org/topics/renewables/.
2. IEA, *Key world energy statistics 2014*. International Energy Agency: http://www.iea.org/publications/freepublications/publication/key-world-energy-statistics-2014.html. p. 82.
3. IEA, *Electricity in a Climate-constrained World - Data & Analyses*. 2012, International Energy Agency: http://www.iea.org/publications/freepublications/publication/electricity-in-a-climate-constrained-world---data--analyses.html. p. 118.
4. Siemens. *SpecTRON - Subsea Medium and High Power Electrical Connector Systems*. [cited 2015 19 May]; Available from: http://www.energy.siemens.com/mx/pool/hq/industries-utilities/oil-gas/applications/subsea/products/connectors/SpecTRON_July_2013.pdf.
5. Qin, N., et al., *Offshore wind farm connection with low frequency AC transmission technology.* 2009: p. 1-8.
6. Song-Manguelle, J., et al., *Power transfer capability of HVAC cables for subsea transmission and distribution systems*, IEEE, Editor., IEEE: Chicago, IL.
7. Antoniou, D., A. Tzimas, and S.M. Rowland, *Electric fields in LVDC cables*, in *IEEE International Conference on Solid Dielectrics (ICSD)*. 2013, IEEE: Bologna. p. 484-487.
8. Tzimas, A., D. Antoniou, and S.M. Rowland, *Low voltage DC cable insulation challanges and opportunities*, in *Conference on Electrical Insulation and Dielectric Phenomena (CEIDP)*. 2012: Montreal. p. 696-699.
9. Kreuger, F.H., *Industial high DC voltage*. 1995: Delft University Press.
10. Giants, T.W., *Crystallinity and dielectric properties of PEEK, poly(ether ether ketone).* IEEE Transactions on Dielectrics and Electrical Insulation, 1994. **1**(6): p. 991-999.
11. Mohammed, M.H., et al., *Physical properties of poly(ether ether ketone) exposed to simulated severe oilfield service conditions.* Polymer Degradation and Stability, 2013. **98**(6): p. 1264-1270.
12. Ho, J. and T.R. Jow, *Effect of crystallinity and morphology on dielectric properties of PEEK at elevated temperature*, in *IEEE International conference on solid dielectrics (ICSD)*. 2013, IEEE: Bologna. p. 385-388.
13. AG, E.I. *Campus Datasheet VESTAKEEP 3300G PEEK*. [cited 2015 6 February]; Available from: http://www.campusplastics.com/campus/en/datasheet/VESTAKEEP%C2%AE+3300+G/Evonik+Industries+AG/66/6991c4e3.
14. Das-Gupta, D. and K. Doughty, *Dielectric and Conduction Processes in Polyetherether Ketone (PEEK).* IEEE Transactions on Electrical Insulation, 1987. **EI-22**(1): p. 1-7.
15. Grayson, M.A. and C.J. Wolf, *The solubility and diffusion of water in poly(aryl-ether-ether-ketone) (PEEK).* Journal of Polymer Science Part B: Polymer Physics, 1987. **25**(1): p. 31-41.

16. Kim, E.J. and Y. Ohki, *Ionic Behavior of Dc Conduction in Polyetheretherketone.* Ieee Transactions on Dielectrics and Electrical Insulation, 1995. **2**(1): p. 74-83.
17. Ve, T.A., F. Mauseth, and E. Ildstad, *Effect of water content on the conductivity of XLPE insulation*, in *Electrical Insulation and Dielectric Phenomena (CEIDP)*. 2012, IEEE: Montreal, QC. p. 649-653.
18. Jeroense, M.J.P. and F.H. Kreuger, *Electrical conduction in HVDC mass-impregnated paper cable.* IEEE Transactions on Dielectrics and Electrical Insulation, 1995. **2**(5): p. 718-723.
19. Ildstad, E., F. Mauseth, and G. Balog, *Space Charge and Electric Field Distribution in Current loaded Polyethylene Insulated HVDC Cables*.
20. Hampton, R.N., *Feature article - Some of the considerations for materials operating under high-voltage, direct- current stresses.* IEEE Electrical Insulation Magazine, 2008. **24**(1): p. 5-13.
21. Zaengl, W.S., *Dielectric spectroscopy in time and frequency domain for HV power equipment. I. Theoretical considerations.* IEEE Electrical Insulation Magazine, 2003. **19**(5): p. 5-19.
22. Ildstad, E., *High Voltage Insulation Materials*. 2012, Department of Electric Power Engineering: NTNU.
23. Saha, T.K. and P. Purkait. *Investigation of polarization and depolarization current measurements for the assessment of oil-paper insulation of aged transformers*. in *IEEE Transactions on Dielectrics and Electrical Insulation*. 2004.
24. Jamail, N.A.M., M.A.M. Piah, and N.A. Muhamad, *Comparative study on conductivity using Polarization and Depolarization Current (PDC) test for HV insulation*, in *International conference on electrical engineering and informatics (ICEEI)*. 2011, IEEE. p. 1-6.
25. Kasiri, N.F., et al., *Design of HV switching for polarization & depolarization current measurement*, in *IEEE 7th International Power Engineering and Optimization Conference (PEOCO)*. 2013, IEEE: Malaysia. p. 35-39.
26. Fofana, I., et al., *Polarization and Depolarization Current measurements of oil impregnated paper insulation system under thermal runaway.* 2010: p. 1-4.
27. Vrentas, J.S. and C.M. Vrentas, *Fickian diffusion in glassy polymer-solvent systems.* Journal of Polymer Science Part B: Polymer Physics, 1992. **30**(9): p. 1005-1011.
28. Park, G.S. and J. Crank, *Diffusion in polymers*. 1968, London: Academic Press. XII, 452 s. : ill.
29. Browne, M.M., M. Forsyth, and A.A. Goodwin, *Solvent diffusion in poly(ether ether ketone)/poly(ether imide) blends.* Polymer, 1995. **36**(22): p. 4359-4360.
30. Wolf, C.J. and M.A. Grayson, *Solubility, diffusion and swelling of fluids in thermoplastic resin systems.* Polymer, 1993. **34**(4): p. 746-751.
31. Nordas, S. and S. Hvidsten, *Water Diffusion in High Voltage Subsea Cable Outer Sheath Materials.* 2008: p. 591-594.
32. ASTM, *D257-14 Standard Test Methods for DC Resistance or Conductance of Insulating Materials*. 2014, ASTM International. p. 18.

33. Jacobsen, B.A., *Characterization of insulation material for HVDC subsea connectors - Simulation and evaluation of methods for measureing conductivity*, in *Department of Electric power engineering*. 2014, NTNU.
34. Kreuger, F.H., *Industial high voltage*. 1991: Delft University Press.
35. Pim, J.A., *The electrical breakdown strength of air at ultra-high frequencies.* Proceedings of the IEE - Part III: Radio and Communication Engineering, 1949. **96**(40): p. 117-129.
36. Seward, E.W., *The electric strength of air at high frequencies.* Journal of the Institution of Electrical Engineers, 1939. **84**(506): p. 288-292.
37. Keithley. *Model 6485 Picoammeter Instruction Manual*. 2011; Available from: www.keithley.com.
38. EGB, *High-Voltage Resistors SGP/OGP*. EGB Resistors.
39. Das-Gupta, D.K. and A. Goodings, *Surface conductivity of irradiated polymers in humid environment*. 1989. p. 186-191.
40. *Internal report*. SINTEF Energy Research AS.
41. *Midel 7131 Dielectric Insulation Fluid Overview*. 2014, M&I Materials Ltd.
42. *Unpublished work on the sorption of MIDEL in PEEK*. SINTEF Energy Research.

10 Appendix

Appendix A Ionic hopping

The conduction mechanisms are generally considered at a microscopic level, and the conductivity is then described as the transportation of electrons or ions through a medium [17]:

$$\sigma = \sum_j q_j n_j \mu_j \tag{10.1}$$

where q_i, n_i and μ_i are the charge, quantity and mobility of charge carrier j.

The dominating conduction mechanism in PEEK is ionic hopping [14, 16], and taking a closer look at how this mechanism work is necessary to understand how it affects the overall conductivity.

Ionic conduction may be the result of several other conduction mechanisms, and on a microscopic level, a medium consist of n_i particles of type i (mechanisms). The charge, q_i, for one such particle is given as [18]:

$$q_i = \omega_i e \tag{10.2}$$

where ω_i is the attempt-to-escape frequency.

Moreover, the medium consist of particles of different types and sizes. This implies that charged particles can be trapped by a host particle, which is usually larger. There is also a possibility that a particle is trapped between different host particles where different conduction processes may dominate. Thus, the particle is trapped in a *well* in a *potential energy landscape* between host particles of type i. When trapped, the particle have a potential energy comparable to a height, H_i. Furthermore, the trapped particle has a probability, p_i, to escape this equilibrium, given by:

$$p_i = \frac{\omega_i}{2\pi} \exp\left[-\frac{H_i}{kT}\right] \tag{10.3}$$

where T is the temperature, and k is the Boltzmann constant. If the particles successfully escapes this energy well, it is trapped at the next host.

Since all charged particles in a medium will be affected by an electric field, there will also be a displacement to the barrier height of the energy wells. This means that it will be easier for a trapped particle to escape in one direction than the other when an electric field is applied to the medium. Consequently, if there are no electric field present in the medium, the probability of the particle crossing to either of the neighbor energy wells are equal, resulting in a net particle flux of, Φ, zero across the well. On a microscopic level, the electric field in the potential energy wells' region differs from the external electric field, and is therefore denoted E_{loc}.

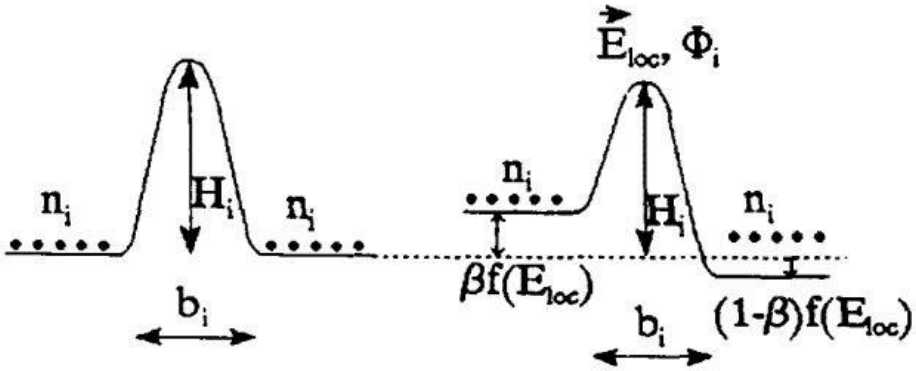

Figure A-1. Barrier heigths around a potential energy well without, and with, the effect of an electric field.

In addition to the electric field, the probability of a particle escaping the well is affected by the distance between two equilibrium positions (across the well), b_i, as well as the shape of the well. To deal with different shapes of the well, a symmetry factor, β, is introduced. $\beta = 1/2$ represents a high degree of symmetry, while $\beta > 1/2$ and $\beta < 1/2$ represents a steeper right and left side of the well, respectively.

The probability of a particle crosses the well from left to right (in the field direction) is then:

$$p_i^{1,2} = \frac{\omega_i}{2\pi} \exp\left[\frac{(1-\beta)q_i b_i E_{loc} - H_i}{kT}\right] \tag{10.4}$$

Consequently, the probability of a particle moving from the right to the left (opposite to the field direction) is:

$$p_i^{2,1} = \frac{\omega_i}{2\pi} \exp\left[\frac{-\beta q_i b_i E_{loc} - H_i}{kT}\right] \tag{10.5}$$

Now, considering that there are n_i particles of type i, the corresponding flux across the wells is:

$$\Phi_i = n_i(p_i^{1,2} - p_i^{2,1}) \tag{10.6}$$

A charged particle of type i contribute to the conduction mechanism, and it then follows that the current density contribution from this particle is:

$$j_i = q_i \Phi_i \tag{10.7}$$

which gives a total conductivity in the region of:

$$\sigma_{loc} = \sum_i \sigma_{i,loc} = \sum_i \frac{j_i}{E_{loc}} \tag{10.8}$$

For objects consisting of one or more mediums with several conduction mechanisms, calculating the contribution from each of them is challenging. A simplification is to consider the medium at a macroscopic level where

$$E_{loc} = E \tag{10.9}$$

This means that the sum of all conduction mechanisms can be considered to be due to one mechanism only:

$$\begin{aligned} \sum_i n_i &= N_0 \\ \sum_i \omega_i &= \omega_0 \\ \sum_i q_i &= q \\ \sum_i H_i &= H \end{aligned} \tag{10.10}$$

Modifying Eq. (10.8) results in a total conductivity for the medium as follows:

$$\sigma = \frac{N_0 q \omega_0}{2\pi E} \exp\left[-\frac{H}{kT}\right] x \left\{\exp\left[\frac{(1-\beta)qbE}{kT}\right] - \exp\left[-\frac{\beta qbE}{kT}\right]\right\} \tag{10.11}$$

If the potential energy well in asymmetrical ($\beta = 0$ or $\beta = 1$), one of the two latter exponential functions in Eq. (10.11) is 1, and for a symmetrical well ($\beta = 1/2$), this equation is reduced to:

$$\sigma = \frac{N_0 q \omega_0}{\pi E} \exp\left[-\frac{H}{kT}\right] \sinh\left[\frac{qbE}{2kT}\right] \tag{10.12}$$

By simplifications, this equation can be expressed in terms of the constants A and B [17]:

$$\sigma = \frac{A}{E} \exp\left[-\frac{H}{kT}\right] \sinh\left(\frac{BE}{T}\right) \tag{10.13}$$

Appendix B Simulation results

Table B-1. Electric field magnitudes from the parametric sweep on the Alternative model.

Electrode radius [mm]	Normal section height [mm]	Electrode distance [mm]	Avg. Above [kV/mm]	Avg. Below [kV/mm]	Min. Above [kV/mm]	Min. Below [kV/mm]	Max. Above [kV/mm]	Max. Below [kV/mm]
20	5	1	1,114	0,954	0,730	0,725	5,538	3,948
20	10	1	1,114	0,954	0,730	0,725	5,538	3,948
25	5	1	1,114	0,954	0,730	0,725	5,538	3,948
25	10	1	1,114	0,954	0,730	0,725	5,538	3,948
30	5	1	1,114	0,954	0,730	0,725	5,538	3,948
30	10	1	1,114	0,954	0,730	0,725	5,538	3,948

Appendix C Evaporation procedure

C.1 Electrode rings

Common for both sets of the electrode rings, is the 10 mm wide outer section keeping the creep distance clean. To be able to evaporate the HV- and measurement electrodes with the measurements in Table 3.2, a 1 mm wide gap protection ring is attached to the outer ring. Three arms secure this gap protection, but also divides the measurement electrode into three separate sections.

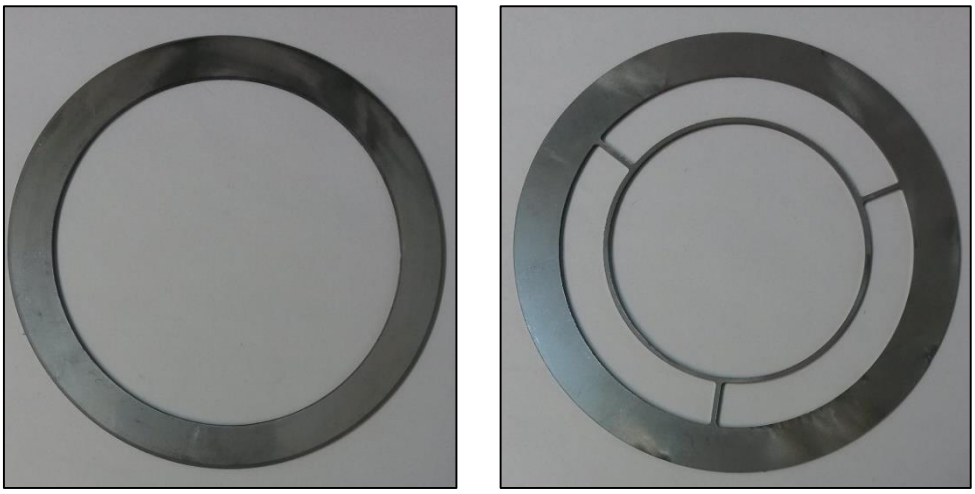

(a) (b)

Figure C-1. Electrode rings for the evaporation procedure of the ASTM specimens. (a) Ring afor evaporating the ground electrode (E3). (b) Ring for evaporating the HV- and measurement electrodes (E1 and E2).

C.2 Evaporation procedure

The principle of the vacuum evaporator used to evaporate the metal electrodes in Section 4.1.3, is to vaporize a piece of metal in a low-pressure environment (bell jar). Placing the metal in a filament ensures that it melts when a current is flowing. When the metal turn into vapor, it will adhere to any overlying objects as it travels upwards, meaning that the PEEK must be located above this filament.

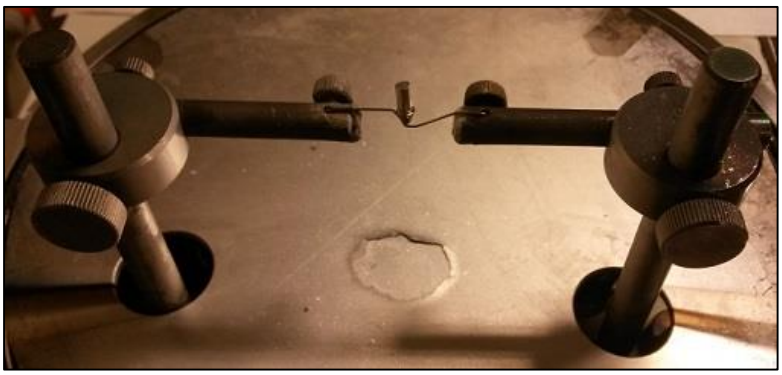

Figure C-2. Filament and aluminum mounted in the current carrying circuit

After preparing the aluminum, the next step is then to mount the PEEK specimens in their respective matrices. Due to the curvature of the PEEK, placing additional weights on top, ensures that the specimens come into contact with the matrix or electrode rings.

Figure C-3. ASTM specimens, electrode rings and weights mounted in the matrix prior to evaporation.

After placing the bell jar back on the evaporator, a low pressure is created by operating a rotary- and diffusion pump in series by having valves V1 and V2 open, while V3, V4 and V5 is closed:

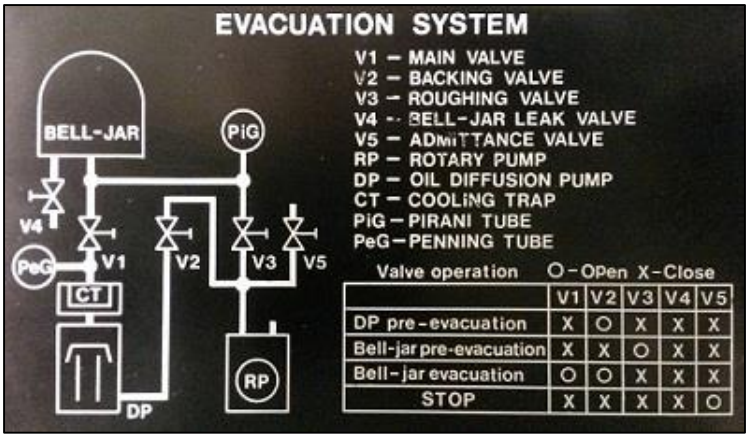

Figure C-4. Valve scheme for the vacuum evaporator.

The current through the filament may be switched on once the pressure inside the bell jar reaches 0.5 mPa or less. Gradually increasing the current reduces the risk of the filament breaking. When the current reaches approximately 30 A, the aluminum melts and turns into vapor. After a few seconds, the evaporation is complete and the current switched off. Before opening the bell jar, the specimen need to cool down for 10-15 minutes.

Appendix D Microscope images

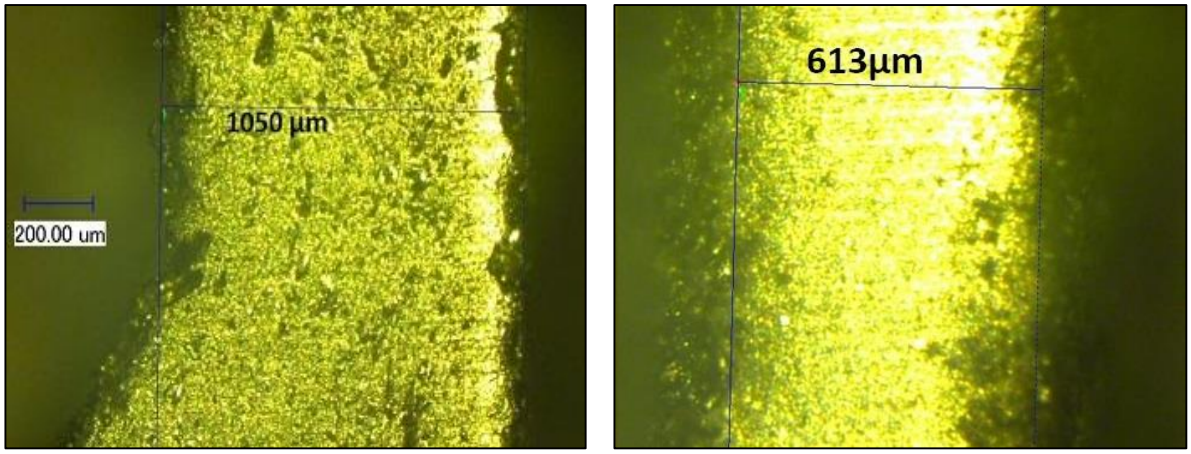

(a) (b)

Figure D-1. Width of the ASTM electrode rings close to a tri-point (section which connects the inner- and outer ring). (a) and (b) shows the widths from both sides of this point.

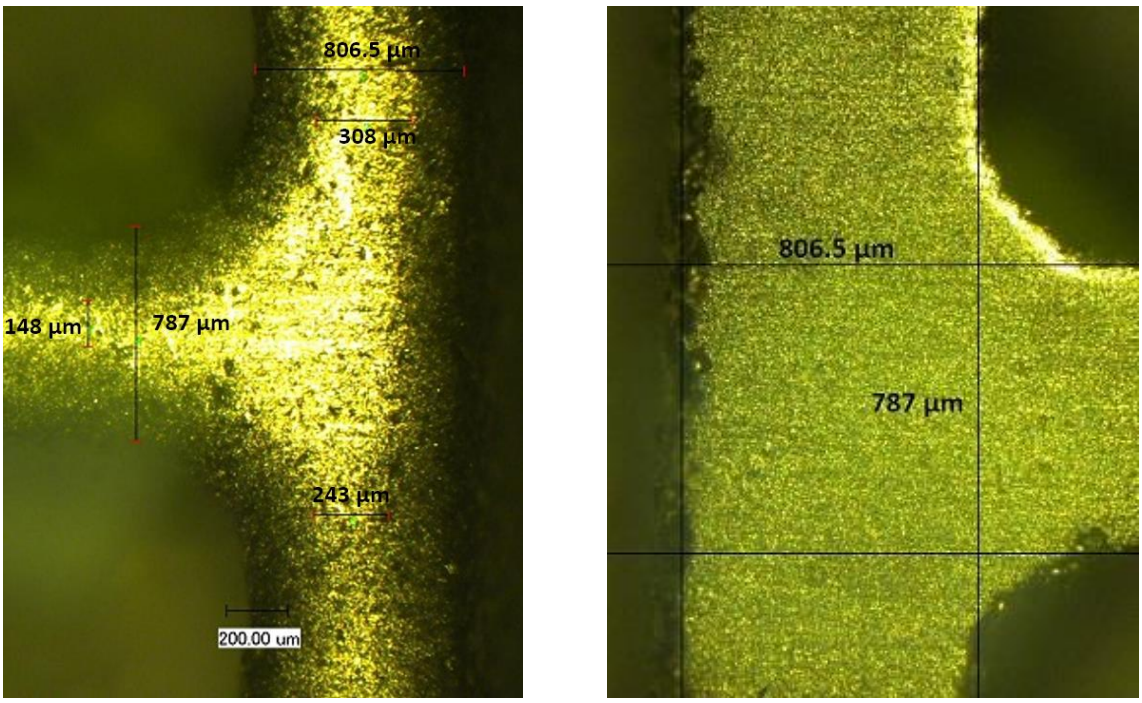

(a) (b)

Figure D-2. Width of a tri-point on the Alternative methods' matrix. (a) and (b) show measurements for both sides of the same tri-point.

Appendix E ASTM PDC plots

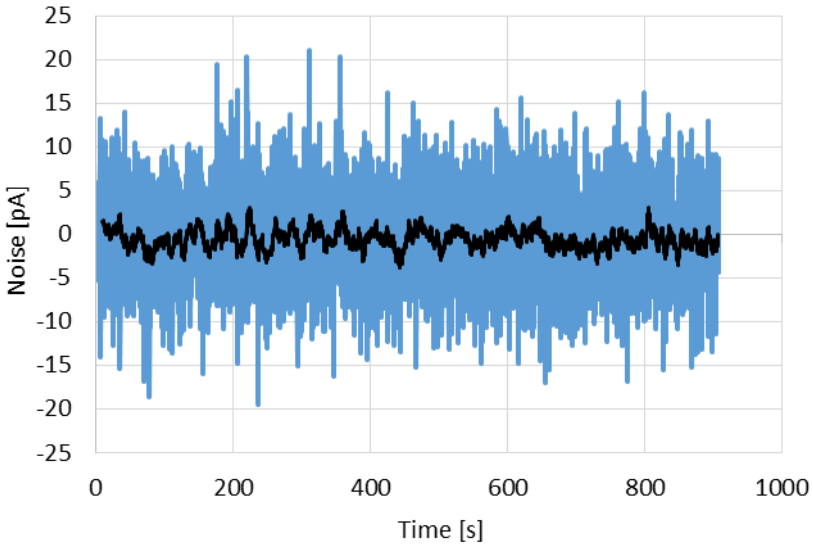

Figure E-1. Noise measurement for ASTM specimen no. 1 at 40 °C and 500 V.

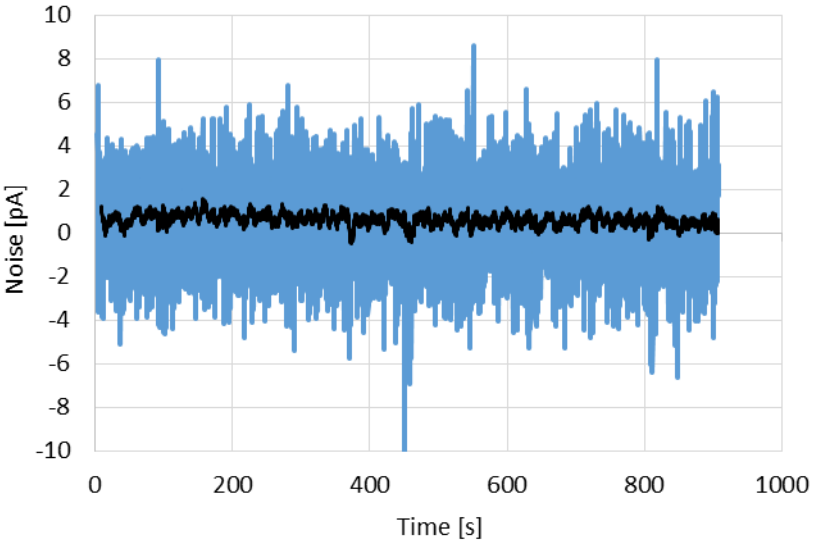

Figure E-2. Noise measurement for ASTM specimen no. 1 at 80 °C and 1500 V.

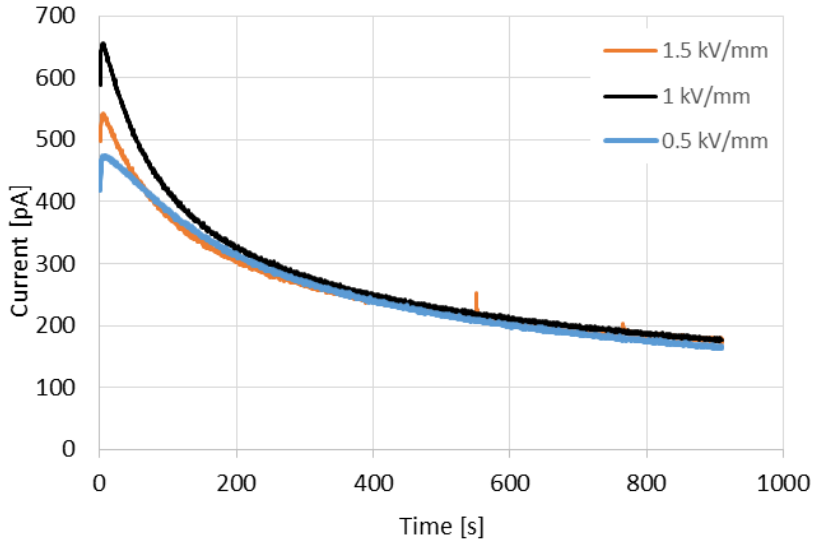

Figure E-3. Polarization currents for ASTM specimen no. 1 at 80 °C.

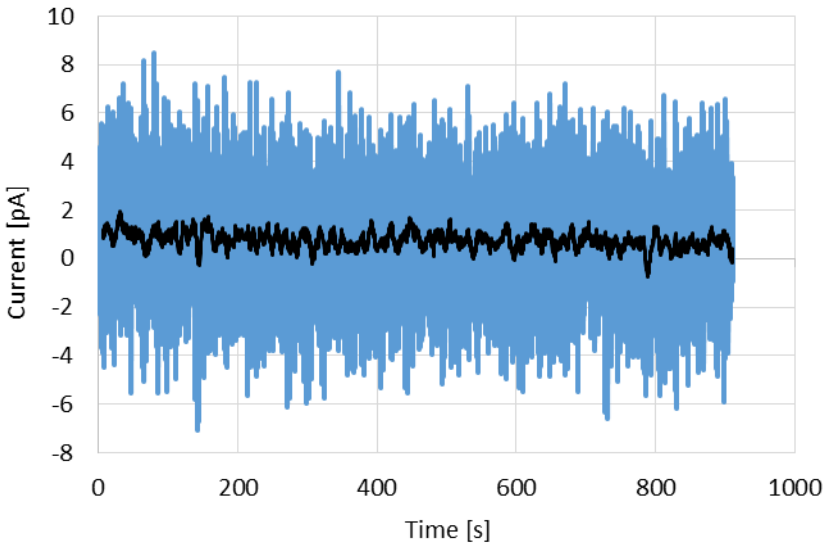

Figure E-4. Polarization current for ASTM specimen no. 3 at 70 °C and 1500 V.

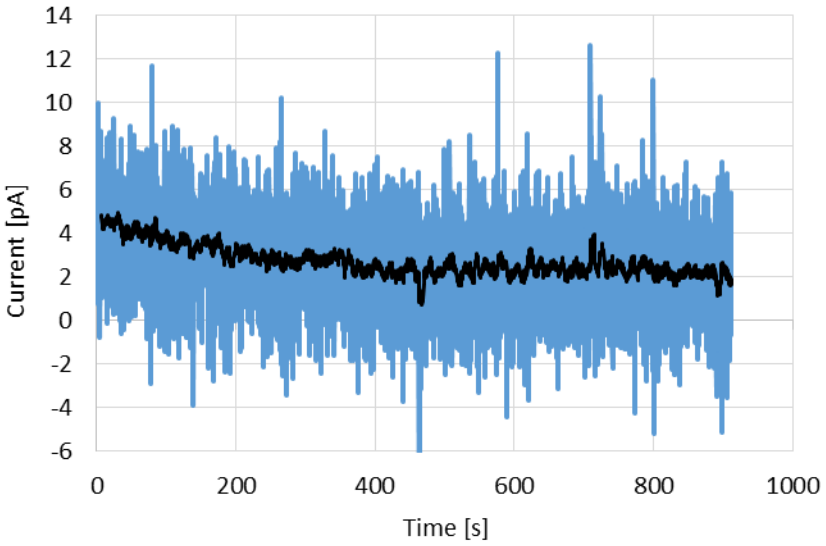

Figure E-5. Polarization current for ASTM specimen no. 3 at 80 °C and 1000 V.

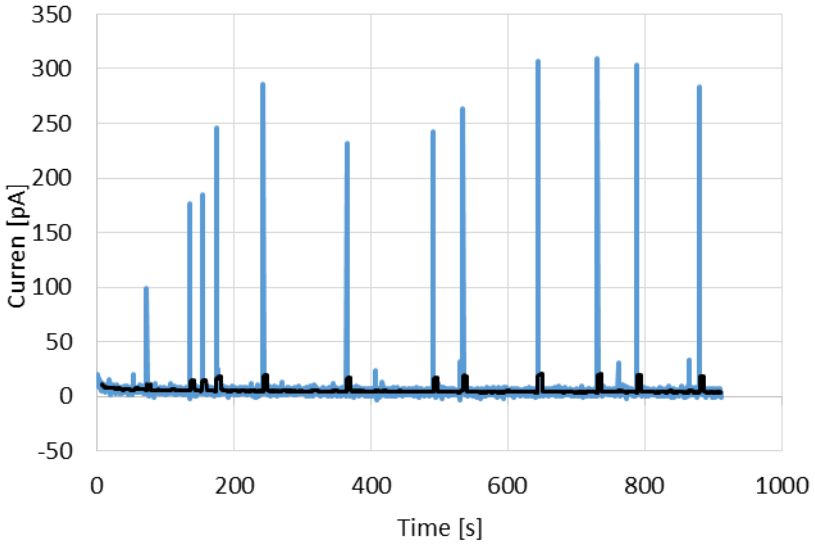

Figure E-6. Unfiltered polarization current for ASTM specimen no. 3 at 80 °C and 1500 V.

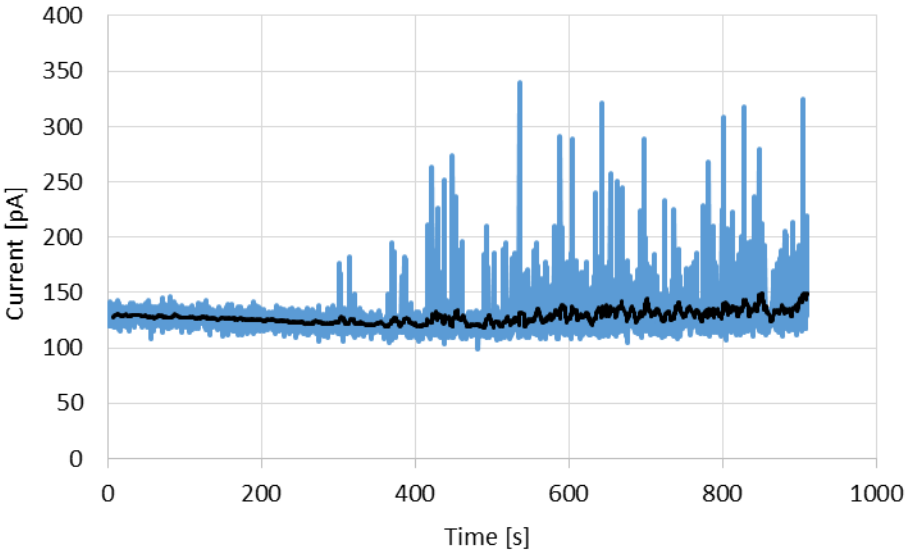

Figure E-7. Unfiltered polarization current for ASTM specimen no. 2 at 70 °C and 1000 V.

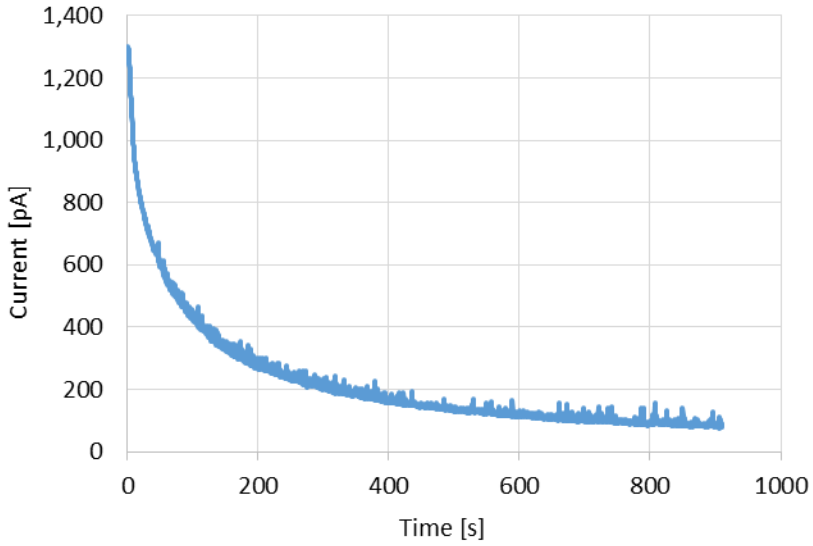

Figure E-8. Polarization current for ASTM specimen no. 2 at 80 °C and 1500 V.

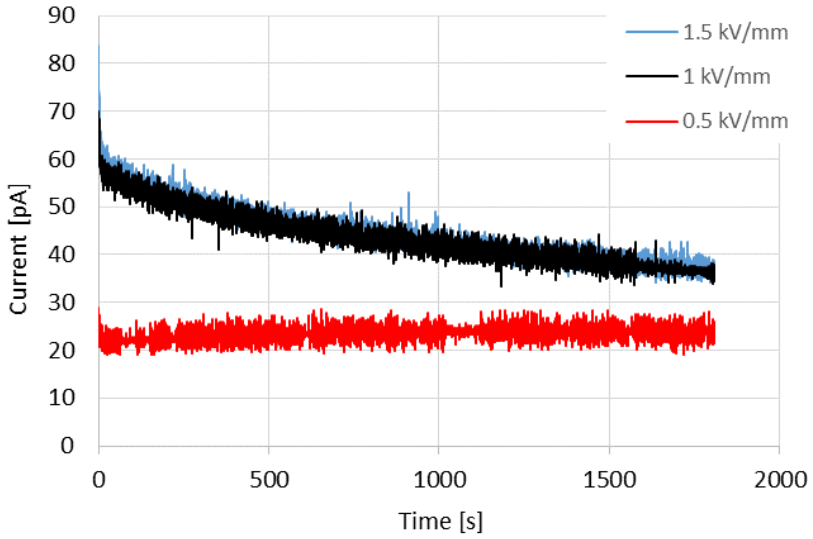

Figure E-9. Polarization current for ASTM specimen no. 4 at 70 C.

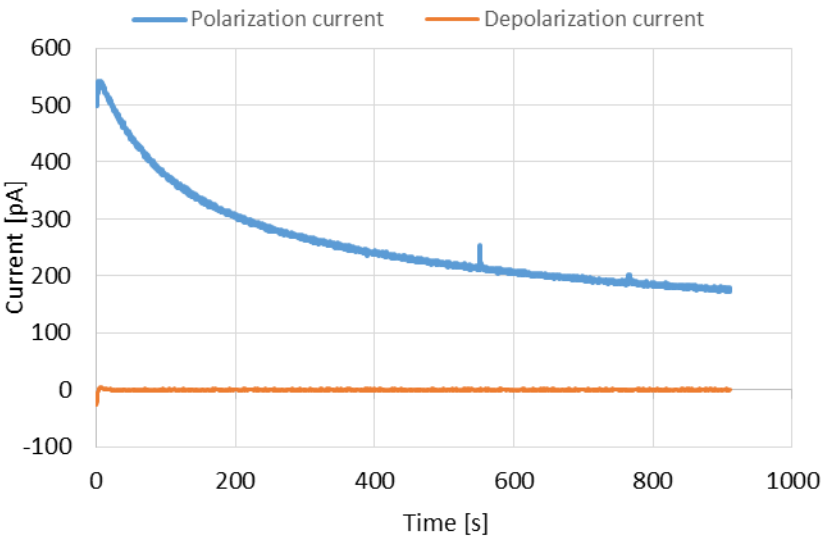

Figure E-10. Difference in pol. and depol. Current waveforms.
Here for ASTM specimen no. 1 at 80 °C and 1500 V.

Appendix F Alternative PDC plots

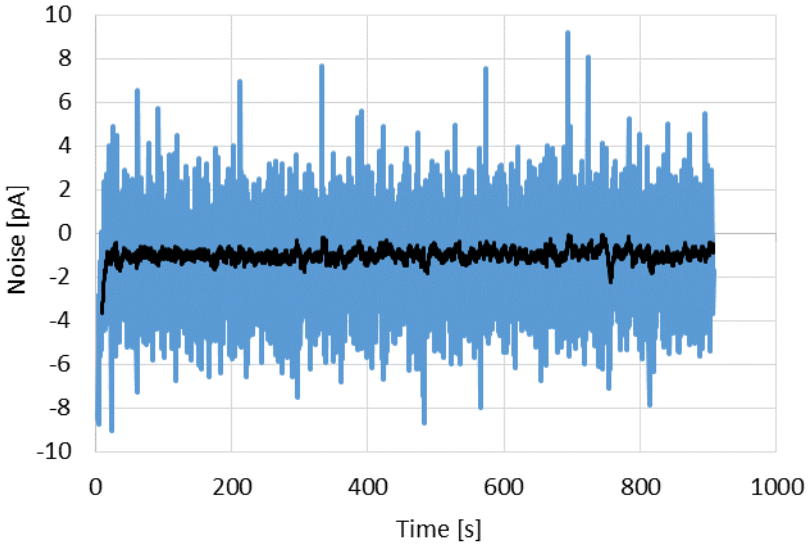

Figure F-1. Noise measurement for Alternative specimen no. 1 at 70 °C and 1500 V.

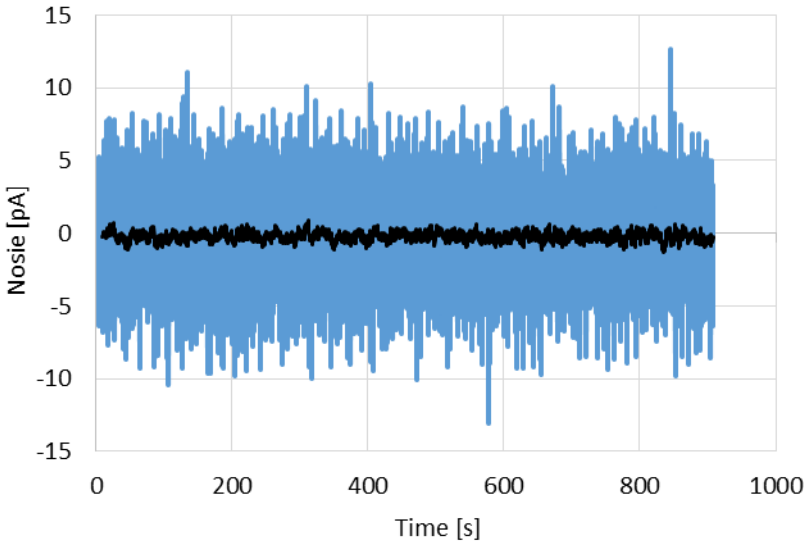

Figure F-2. Noise measurement for Alternative specimen no. 3 at 40 °C 1500 V.

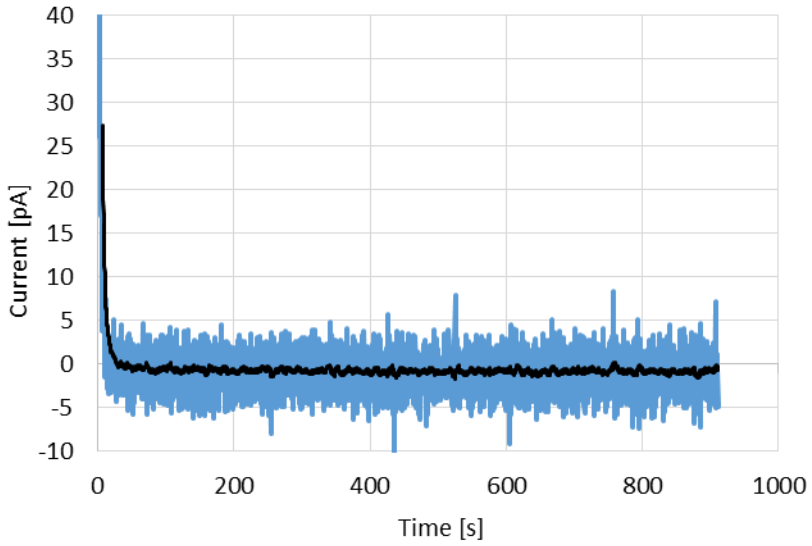

Figure F-3. Polarization current for Alternative specimen no. 1 at 60 °C and 1000 V.

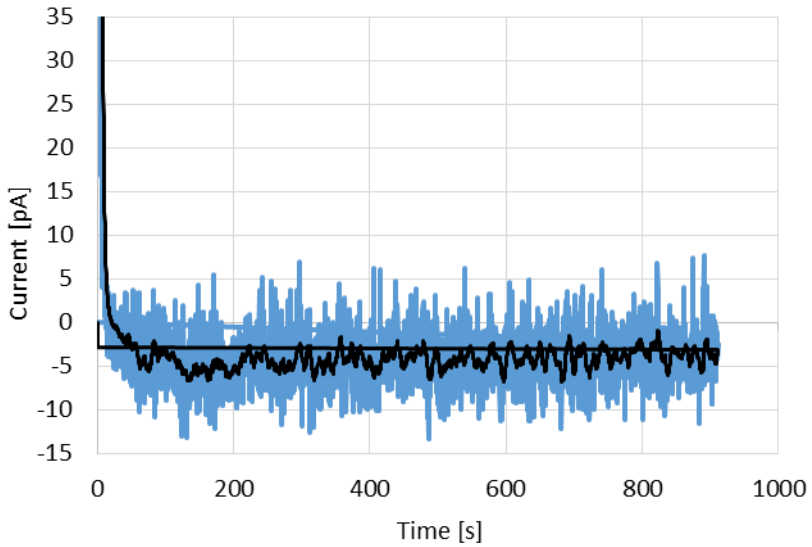

Figure F-4. Poalrization current for Alternative specimen no. 2 at 80 °C and 1000 V.

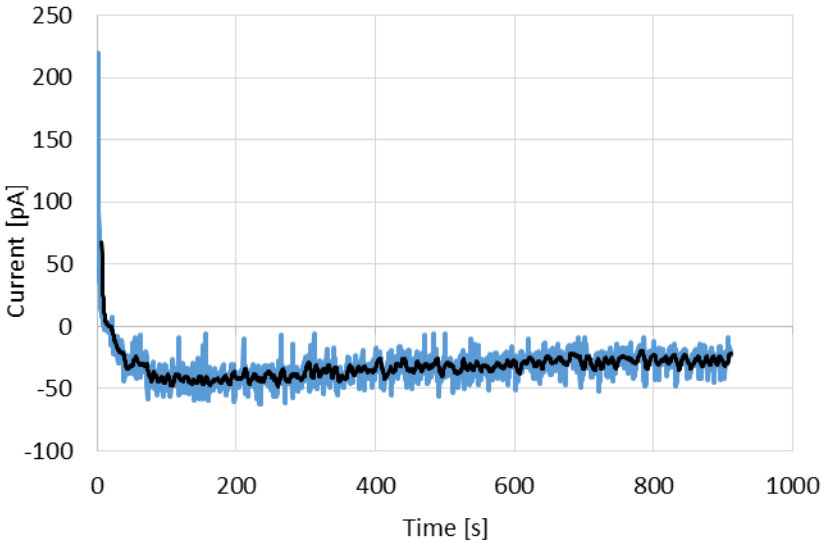

Figure F-5. Polarization current for Alternative specimen no. 2 at 80 °C and 1500 V.

Appendix G Resistive current and conductivities

Table G-1. Resistive currents for the ASTM specimens.

Resistive current [pA]					
***T* [°C]**	***E* [kV/mm]**	**Specimen 1**	**Specimen 2**	**Specimen 3**	**Specimen 4**
40	**0.5**	-0.87	0.13	-0.08	0.11
	1.0	0.17	0.17	-0.14	-0.03
	1.5	-0.24	0.54	0.34	0.20
60	**0.5**	12.55	7.06	0.08	4.63
	1.0	21.06	13.31	0.03	9.17
	1.5	28.57	19.78	0.08	10.46
70	**0.5**	93.95	14.31	0.15	23.76
	1.0	112.53	133.06	0.22	36.54
	1.5	128.95	299.89	0.57	37.26
80	**0.5**	170.59	42.28	1.47	43.83
	1.0	182.25	102.10	2.48	77.11
	1.5	180.70	162.35	5.44	97.55

Table G-2. Surface conductivities for the ASTM specimens.

Surface conductivity [S/m]					
***T* [°C]**	***E* [kV/mm]**	**Specimen 1**	**Specimen 2**	**Specimen 3**	**Specimen 4**
40	**0.5**	-5.77E-16	9.00E-17	-5.40E-17	7.66E-17
	1.0	5.93E-17	6.01E-17	-4.92E-17	-9.85E-18
	1.5	-5.51E-17	1.24E-16	7.86E-17	4.62E-17
60	**0.5**	8.32E-15	4.79E-15	5.77E-17	3.09E-15
	1.0	7.22E-15	4.51E-15	1.06E-17	3.06E-15
	1.5	6.31E-15	4.47E-15	2.03E-17	2.33E-15
70	**0.5**	6.22E-14	9.71E-15	1.07E-16	1.59E-14
	1.0	3.73E-14	4.51E-14	7.61E-17	1.22E-14
	1.5	2.85E-14	6.76E-14	1.32E-16	8.30E-15
80	**0.5**	1.13E-13	2.87E-14	1.01E-15	2.93E-14
	1.0	6.04E-14	3.46E-14	8.48E-16	2.58E-14
	1.5	3.99E-14	3.67E-14	1.24E-15	2.17E-14

Table G-3. Resistive currents for the Alternative specimens.

Resistive current [pA]					
***T* [°C]**	***E* [kV/mm]**	**Specimen 1**	**Specimen 2**	**Specimen 3**	**Specimen 4**
40	**0.5**	0.00	0.13	0.07	0.06
	1.0	0.04	-0.25	-0.03	0.17
	1.5	0.20	0.16	0.05	-0.99
60	**0.5**	0.14	0.47	0.10	-0.22
	1.0	0.23	0.78	0.33	-0.40
	1.5	0.29	0.94	0.13	-0.63
70	**0.5**	0.11	0.17	0.17	0.01
	1.0	0.22	0.33	0.19	0.22
	1.5	-37.22	0.14	0.42	0.94
80	**0.5**	-0.23	0.06	0.16	0.02
	1.0	-0.64	-3.27	0.22	-6.36
	1.5	0.32	-27.34	0.11	-4.78

Table G-4. Surface conductivities for the Alternative specimens.

Surface conductivity [S/m]					
***T* [°C]**	***E* [kV/mm]**	**Specimen 1**	**Specimen 2**	**Specimen 3**	**Specimen 4**
40	**0.5**	1.53E-18	4.54E-16	2.67E-16	2.02E-16
	1.0	5.76E-17	-1.69E-15	-5.70E-17	2.67E-16
	1.5	1.90E-16	1.76E-16	6.80E-17	-1.07E-15
60	**0.5**	3.77E-16	1.59E-15	4.10E-16	-7.22E-16
	1.0	3.27E-16	1.32E-15	6.62E-16	-6.47E-16
	1.5	2.78E-16	1.06E-15	1.75E-16	-6.83E-16
70	**0.5**	3.28E-16	5.76E-16	6.84E-16	1.80E-17
	1.0	3.10E-16	5.63E-16	3.68E-16	3.61E-16
	1.5	-3.55E-14	1.53E-16	5.67E-16	1.01E-15
80	**0.5**	-6.72E-16	2.11E-16	6.40E-16	5.35E-17
	1.0	-9.19E-16	-5.52E-15	4.39E-16	-1.02E-14
	1.5	3.10E-16	-3.07E-14	1.43E-16	-5.13E-15

Appendix H ASTM log plots

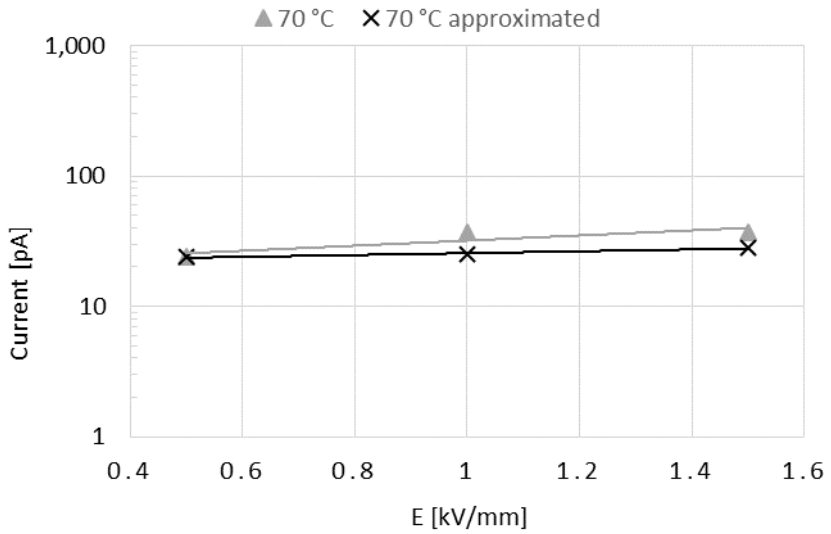

Figure H-1. Difference in measured and approximated resistive currents for ASTM specimen no. 4 at 70 °C.

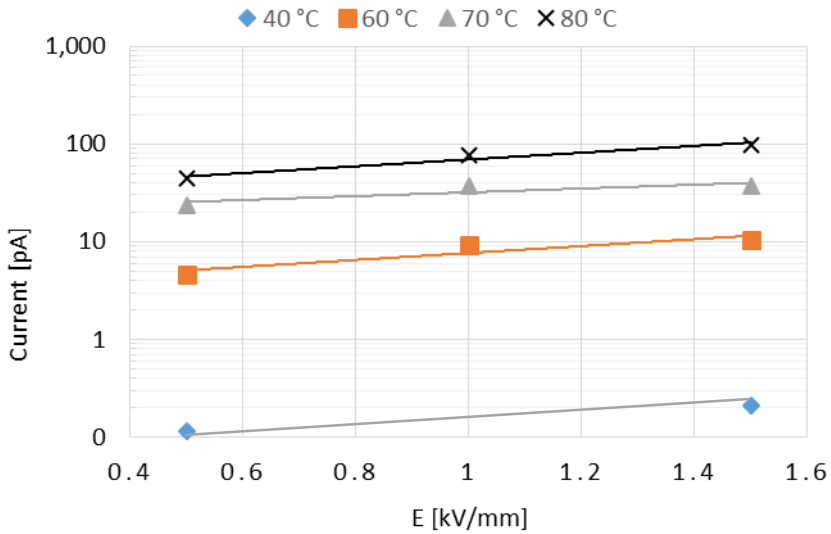

Figure H-2. Current for ASTM specimen no. 4 as a function of electric fields strength.

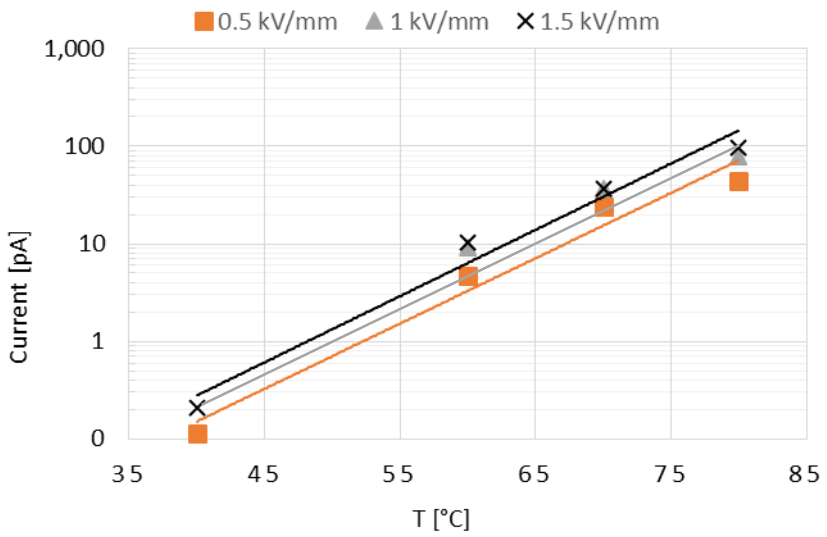

Figure H-3. Current for ASTM specimen no. 4 as a function of temperature.

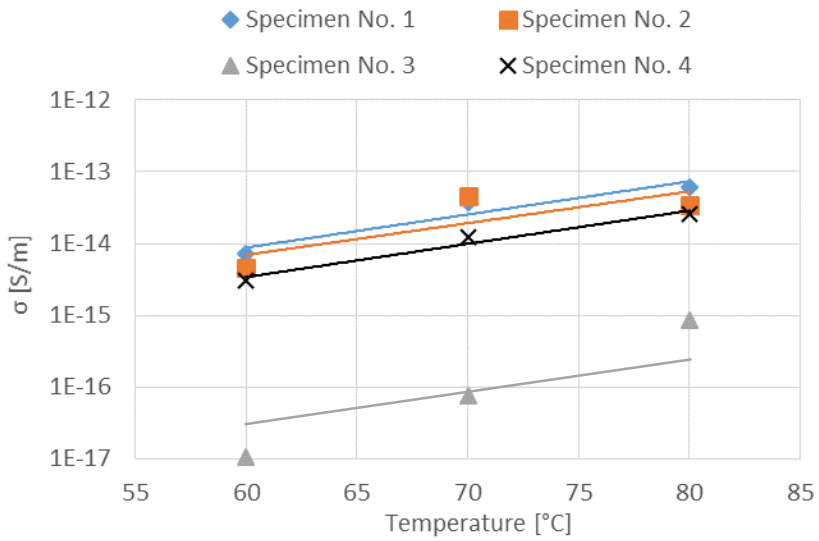

Figure H-4. Surface conductivity at 1 kV/mm for all ASTM specimens plotted against 60 to 80°C. The exponential trendline for specimen no. 3 is based on the slopes for the other specimens' lines.

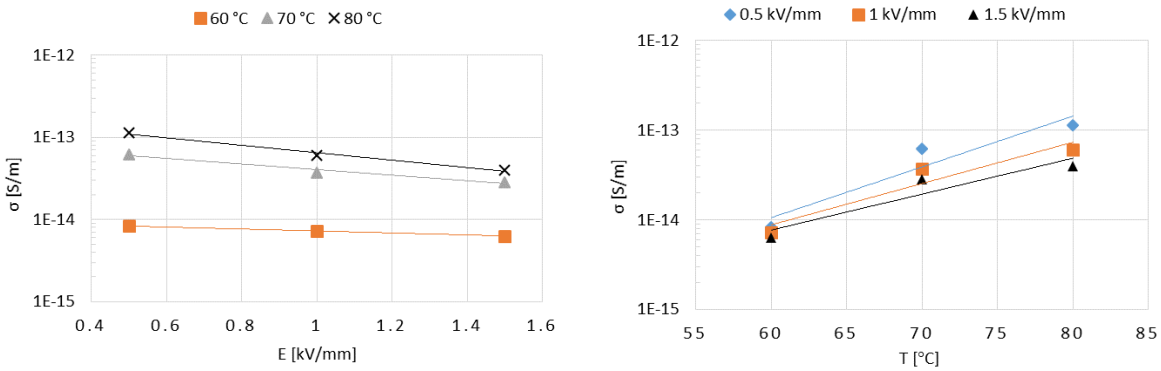

(a) (b)

Figure H-5. Surface conductivity of ASTM specimen No. 1 plotted agains (a) electric field, and (b) temperature

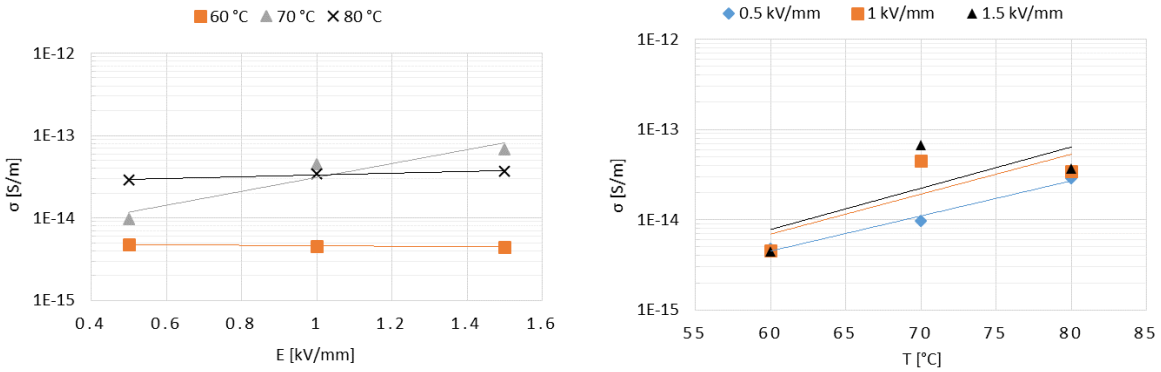

(a) (b)

Figure H-6. Surface conductivity of ASTM specimen No. 2 plotted agains (a) electric field, and (b) temperature

Appendix I Alternative log plots

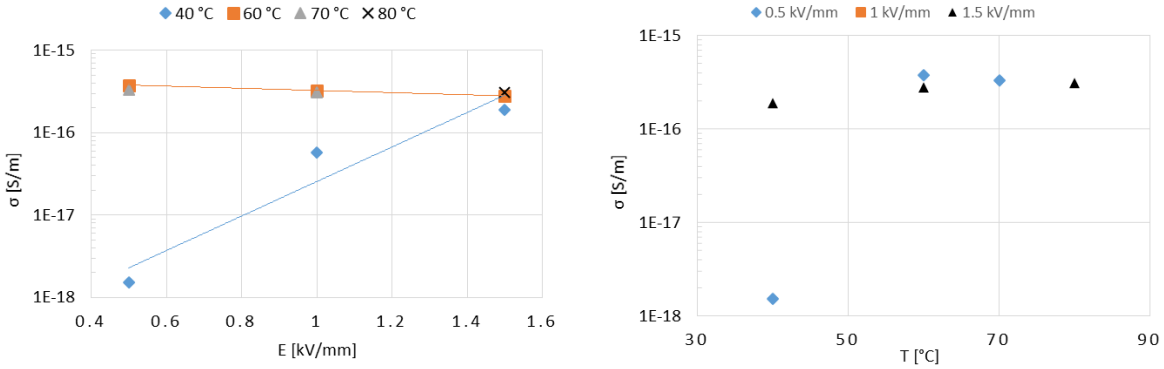

(a) (b)

Figure I-1. Surface conductivity of Alternative specimen no. 1 as a function of (a) electric field , and (b) temperature.

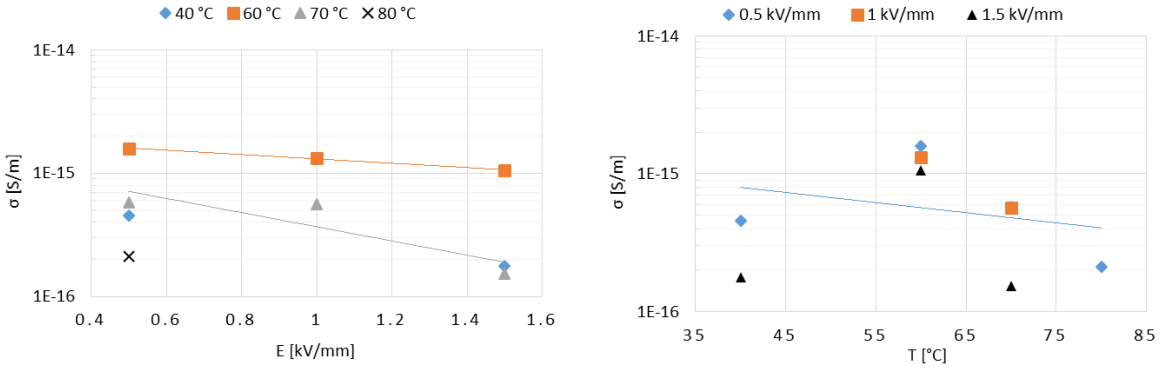

(a) (b)

Figure I-2. Surface conductivity of Alternative specimen no. 2 as a function of (a) electric field , and (b) temperature.

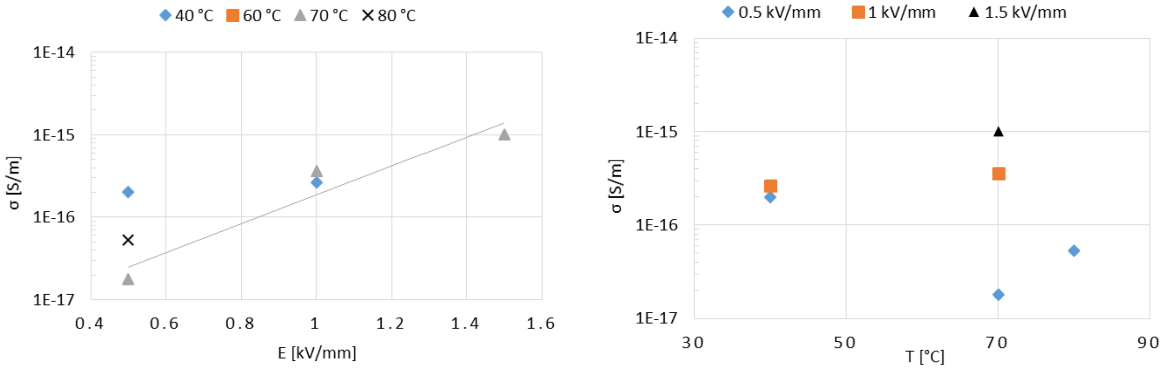

(a) (b)

Figure I-3. Surface conductivity of Alternative specimen no. 4 as a function of (a) electric field , and (b) temperature.

Appendix J Matlab: Curve fitting

J.1 The MATLAB function

```
function []=expfit(a,c)                 %function takes a filename as argument
A=importdata(a);
A1=A(:,1);                              %column 1: time
A2=A(:,2);                              %column 2: measured current
A3=A(:,3);                              %column 3: 20 period average of col. 2

%Subtracting the constant from the measurement data
for i=1:length(A(:,1))
    A2(i)=A2(i)-c;
    A3(i)=A3(i)-c;
end

%Curve fitting
f1=fit(A1,A2,'exp1')                    %exp1:      a*e^(b*x)
f2=fit(A1,A2,'exp2')                    %exp2:      a*e^(b*x)+c*e^(d*x)

%Creating
endvalue=1500;                          %maximum plot time
x=0:0.5:endvalue;
exp1=f1(x);
exp2=f2(x);

%Writing the limits to the screen to verify that the
%exp2 does not take on a negative value
f1(5*endvalue)
f2(5*endvalue)

%Plotting
p=plot(A1,A3,x,exp1,x,exp2);
%hold on
grid on;
set(gca,'fontsize',28);
p(1).LineWidth=6;
p(2).LineWidth=4;
p(3).LineWidth=4;
xlabel('Time [s]', 'fontsize',28);
ylabel('Curren [pA]','fontsize',28);
legend({'Measured current','exp1 fit','exp2
fit'},'Location','northeast','fontsize',28);
```

J.2 Approximated currents

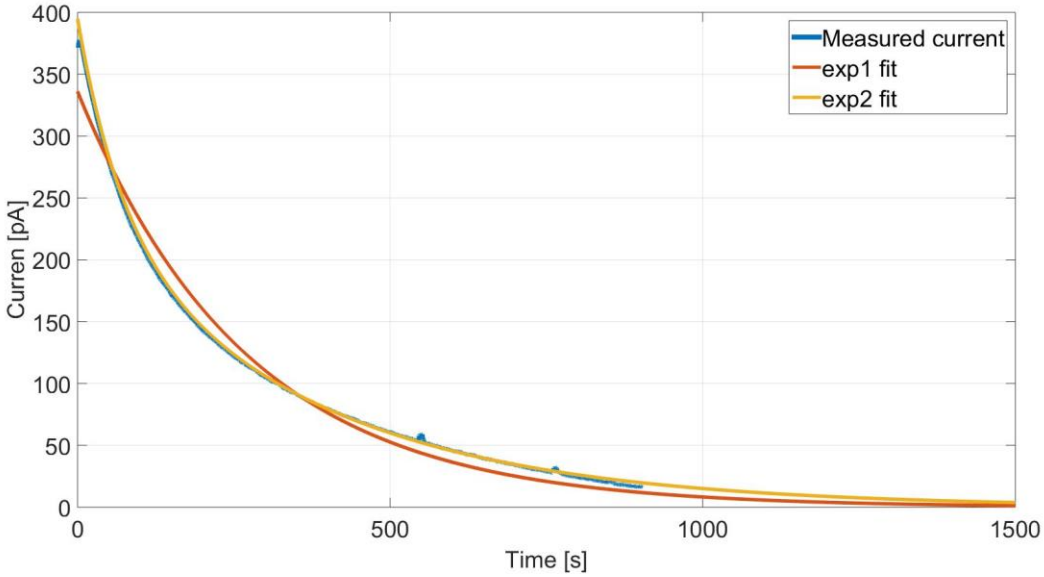

Figure J-1. Curve fitting for specimen no. 1 at 80 °C and 1500 V.

Table J-1. Resistive currents approximated by curve fitting.
Red values indicate values where curve fitting were unsuccessful.

***T* [°C]**	***E* [kV/mm]**	**Specimen 1**	**Specimen 2**	**Specimen 4**
70	**0.5**	85.00	14.32	23.76
	1	100.00	133.06	25.00
	1.5	128.95	299.9	28.00
80	**0.5**	140.00	40.00	35.00
	1	160.00	80.00	65.00
	1.5	160.00	120.00	80.00

Appendix K Specimens exposed to oil

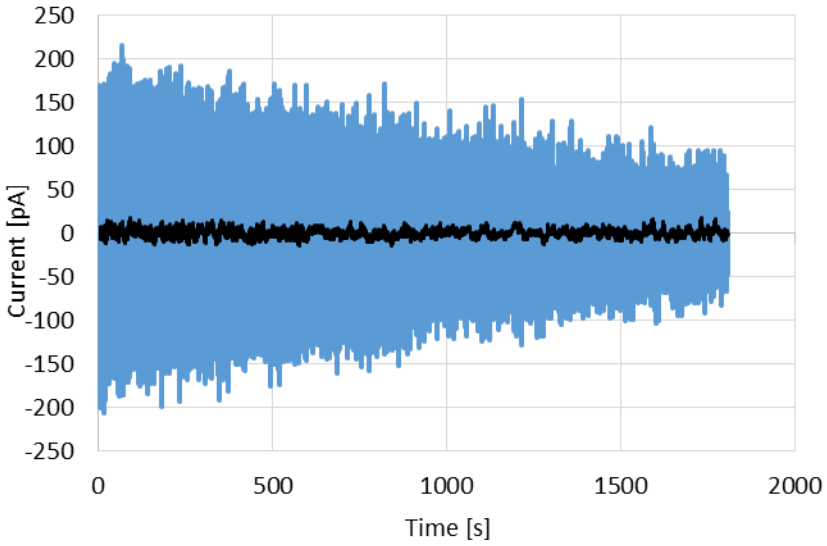

Figure K-1. Polarization current for ASTM specimen no. 1 at 80 °C and 500 V after exposure to MIDEL.

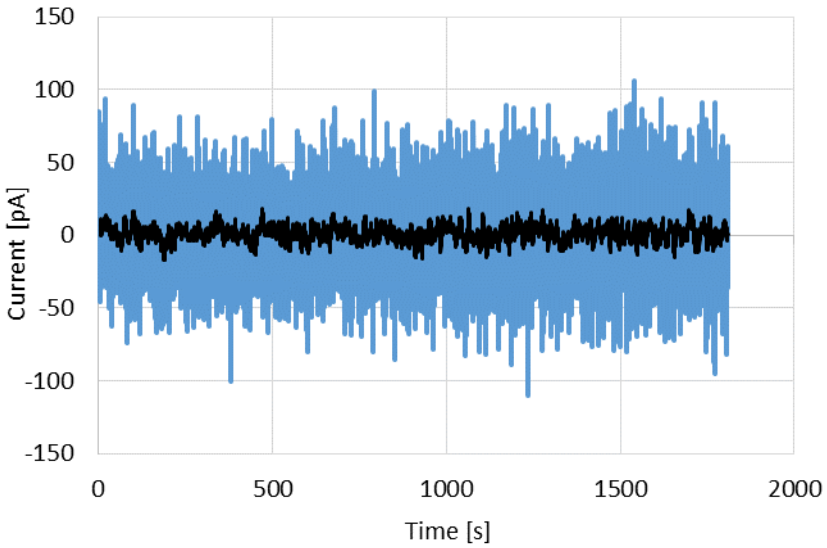

Figure K-2. Polarization current for ASTM specimen no. 1 at 80 °C and 1000 V after exposure to MIDEL.

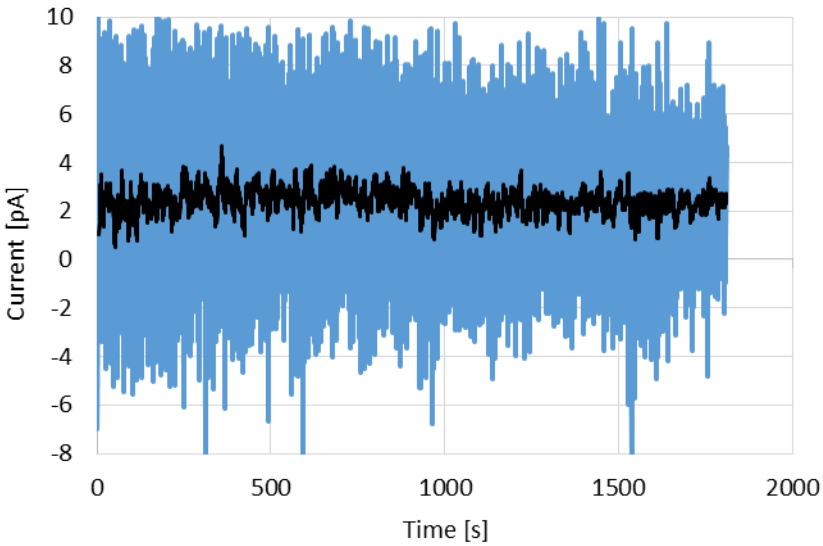

Figure K-3. Polarization current for ASTM specimen no. 4 at 70 °C and 000 V after exposure to MIDEL.

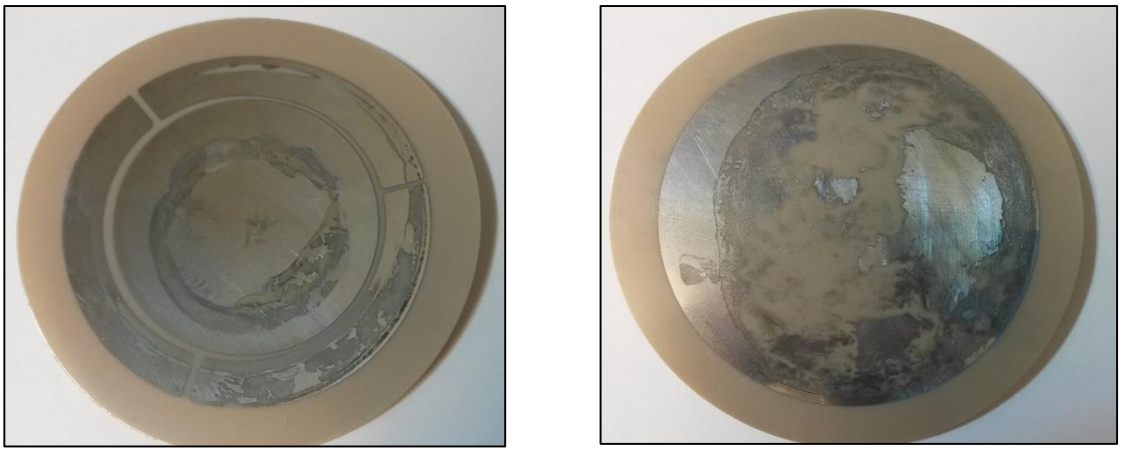

(a) (b)

Figure K-4. Damaged electrodes on a) HV side of ASTM specimen no. 1, and b) grounded side of ASTM specimen no. 4.